Strongly Interacting Bose-Einstein Condensates: Probes and Techniques

by

Juan Manuel Pino II

B.S. Physics, University of Florida, 2002

A thesis submitted to the

Faculty of the Graduate School of the

University of Colorado in partial fulfillment

of the requirements for the degree of

Doctor of Philosophy

Department of Physics

2010

This thesis entitled:
Strongly Interacting Bose-Einstein Condensates: Probes and Techniques
written by Juan Manuel Pino II
has been approved for the Department of Physics

_____

Dr. Deborah S. Jin

_____

Dr. Eric A. Cornell

Date _____

The final copy of this thesis has been examined by the signatories, and we find that both the content and the form meet acceptable presentation standards of scholarly work in the above mentioned discipline.

Pino II, Juan Manuel (Ph.D., Physics)

Strongly Interacting Bose-Einstein Condensates: Probes and Techniques

Thesis directed by Dr. Deborah S. Jin

A dilute gas Bose-Einstein condensate (BEC) near a Feshbach resonance offers a system that can be tuned from the well-understood regime of weak interactions to the complex regime of strong interactions. Strong interactions play a central role in the phenomena of superfluidity in liquid He, and theoretical treatments for this regime have existed since the 1950's. However, these theories have not been experimentally tested as superfluid He offers no similar mechanism with which to tune the interactions. In dilute gas condensates near a Feshbach resonance, where interactions can be tuned, strong interactions have proven difficult to study due to the condensate's metastable nature with respect to the formation of weakly bound molecules. In this thesis, I introduce an experimental system and novel probes of the gas that have been specifically designed to study strongly interacting BECs. I present Bragg spectroscopy measurements that have accessed this regime, as well as proof-of-principle experiments using photon-counting for Bragg spectroscopy at low-momentum. Finally, I show preliminary data using contact spectroscopy, which is a method that could lead to the first measurements of the predicted interaction energies for a dilute Bose gas of atoms in the strongly interacting regime.

Dedication

Para mi Abuelita, 1910-2010.

Acknowledgements

This work not only represents my efforts here at JILA over the years, but also the contributions of a great many others whom I'd like to thank here.

Carl Wieman gave me my opportunity to work with cold atoms when he hired me in 2003. Although he was being pulled in different directions at the end of his tenure here, I always appreciated his efforts to cultivate my understanding of physics, especially through the lunches that Kang-Kuen and I would share with him. Debbie Jin and Eric Cornell adopted me and the ^{85}Rb experiment in 2006. In many ways I felt like I had left the orphanage and was brought into a loving family. Eric Cornell played the role of my advisorial father. He defined our "family values", the study of strongly interacting condensates, and his enthusiasm was infectious. He also happened to have a wit to match his intelligence, and our family dinners (i.e. group meetings) were always lively. The best part about working with Eric was the way he always, always seemed to be able to have a physical picture or two of how things worked. It's really amazing that Eric can be, to me at least, the embodiment of "Physicist", and at the same time be very human. His professional and personal advice were always appreciated, and will stay with me for a long time.

Debbie Jin would then be my advisorial mother. I consider Debbie to be my mentor, advisor, and friend. She is both brilliant and easy going, and can make the complicated seem pedestrian. She is also the most effective person I've ever seen at solving a complicated problem, which is what this thesis, and really all technical work, is all about. Debbie was always accessible, and taught me how to be *effective* at what I do, which, in a professional sense, is the most valuable lesson you can learn. I will be forever in debt to Debbie for taking me on as a student, putting in time

with me, and believing that I could produce. I always enjoyed my interactions with her, and our advisor-student relationship will be the one aspect of graduate school that I miss the most.

I'd also like to thank my labmates over the years. Scott Papp and I spent many hours together in my early years in the lab and I will always respect Scott's knowledge of experimental technologies and techniques. He also has one of the strongest arms of anyone I've ever met, and thankfully some of his knowledge was able to rub off on me while we worked together.

If Debbie and Eric are my experimental parents, that makes Rob Wild my experimental brother. Working with Rob in our ~~nuclear~~ atomic family has been a true blessing. Rob was a great compliment to me, often thinking of a more clever solution to a problem that I would try to solve via "brute force". Working in the lab can be a frustrating endeavor, and often times we are not in our best light when things aren't going well, but Rob was always a (relatively) positive person, able to pick me up when I was frustrated and would have preferred to quit. The lens of working with someone for 10-12 hours a day, 5 days a week in lab where things don't seem to ever work is revealing, but Rob's character always was true. He's as quality an individual as you will ever meet, and I hope that his success in physics will one day match his success as a person.

Phil Makotyn would then be our adopted brother. Although that might sound bad it would turn out that we are all adopted here, even Rob with his Austrian blood. Phil inaugurated the ritual hazing that new labmates endure, and has been a great addition to the lab, bringing not only new perspectives, but also a different skill set which I think will be very useful in the long-term. I think Phil will be a great physicist one day and wish him the best of luck. I'd also like to thank Zach Newman, an REU student who spent a summer with us and whose enthusiasm was always welcome. I'd also like to thank Rachel Umbel, a later REU student, for some of the beam profiling data I used in this thesis.

I'd also like to thank my bi-group cousins. Russ Stutz has been a great, great friend over the years, and we've enjoyed (or at least gone through) experiences ranging from finishing a crib at 3 AM, to running out of gas somewhere in Utah, to epic battles as Quantum Leapers. I don't know if I could have made it through these last few years, least of all grad school, without him, and so,

Dr. Captain Stutz, I salute you. Jayson Stewart is another one of my closest friends I've made in Colorado. When I first met Jayson I was really surprised to find that we had a lot (a lot!) of the same interests. I saw a much of myself in Jayson, and watching him succeed in the lab and as a physicist was instrumental in me staying the course with this PhD. I really can't ever thank him enough for that. Shih-Kuang (Zeke) Tung was, and will always be, a wonderful friend. Zeke is as sharp and hardworking a guy as you'll ever meet, and he's also one of the nicest, with a laugh that would always make me smile. I consider myself lucky to have made his friendship.

To be honest, I don't know exactly where post-doc's lie on the experimental family tree. I think Aaron Leanhardt would be something like that uncle that taught you your first curse words. Aaron's an extremely dedicated worker who's had the unfortunate luck to both be a fan of Detroit sports teams as well as endure my friendship. He is a quality guy, though, and I know I could always count on him if I needed something (like a drive to the airport in under 30 minutes). Giacomo Lamporesi is more like...a godfather, of course. Giacomo I'll thank for being a good roomate (ICOLS, ICAP), great cook (credit: olive oil), and bellissimo friend.

I'd also like to thank John Gaebler for not impaling me with any ski equipment while he's had the chance, and for being a solid neighbor (as of three weeks). I'd also like to thank past group members Kang-Kuen Ni, Josh Zirbel, Silke Ospelkaus, and John Perreault for always being around to answer questions. I look forward to the next-generation bi-group team of Laura Sinclair (best-climbing buddy ever!), Huanqian Loh (always makes me laugh), Brian Neyenhuis, Tyler Cumby, Tara Drake, Ruth Shewmon, Matt Grau, Dan Lobser, and Lin Xia and fully expect this group to bring back the JILA cup to it's rightful home in the bi-group.

Another great thing about JILA is the wonderful support we have from everyone that works here. First I'd like to thank Krista Beck, who has always been there for me for both professional matters and personal dilemma's. Pam Leland should also be thanked for always having a wonderful smile on whenever I've needed her help. The electronics shop staff has taught me a great deal during my time here in JILA. In particular I should thank Terry Brown, who has explained the finer points of electronic design to me, as well as Carl Sauer, who can always be counted on to answer a quick

question, as well as unlock a laser or two with his laugh. The machine shop has also been a great help to me over the years, and I'd like to thank the shop staff as well. In particular Hans Green, who helped Russ and I late into the night designing and building Juan Michael's first crib. And finally J.R. Raith, who's helped me with countless computer (read: Windows) problems.

Outside of JILA I've made a number of friends here at CU, and would like to say thanks to the incoming class of 2002. Johnny "One-Eye" Jost, the best first-mate a pirate could ask for. Keith Ulmer (thanks for the super-important conversations had over soda) and Kirk Ullmann for the best road trip of my life. Marty Boyd, who's come as close as anyone to being as funny as me. Amanda Carpenter and Ashley Carter for putting up with me during that Stat Mech project, and Matt Sammons for all that money he gave me playing poker.

Finally, I'd like to thank my family. My brother Marito, for being my role model as a child and inspiring me to take things apart, challenge myself, and stay humble. Those lessons were never lost on me, and as much as anybody he's shaped me into the man I am today. To my brother Juan Carlos, for teaching me what it means to be a Pino, reminding me about what's truly important in life, and always having my back. To my sister, Ameriquita, and her family Johnny, Diego and Lucas, for loving my son as much as they do. Words cannot describe how much their love for Juan Michael means to me.

To my father, Juan Pino, for making me tough enough to get through this and making me man enough to rely on myself for whatever lies ahead. To a son, a father's love and support is all you need to conquer the world, and my father has always given me an ample amount of both. I'd also like to thank my father for the perspective he provides. He has lived an incredible life, reaching the United States on a 15 foot boat exactly 50 years from the date I defended this thesis, and has experienced both highs and lows that I think few will ever reach. As a child I always thought that I was the polar opposite of my father, but, as I grow older, I realize we are more similar every day.

To my mother, Tesla Fletez Pino, I owe more than I could ever say or write. She has given me pride, humility, empathy and conviction. She has inspired me to always ask questions and her patience is unmatched. The thing that I am most thankful for, however, is her selflessness, which

is the single quality you would most want in a parent. She was there to help me put labels on my science projects late into the night (even if some of them were misspelled!). She was there to spend her Saturday taking me on hour long treks to guitar stores on the other side of town. She was there to buy me my first soldering iron, and she was there reading me Alice in Wonderland (albeit with an accent) while I wondered when this book was going to have another picture. She embodies what an immigrant is and I am grateful to call her not only my mother, but also mi mejor amiga.

My grandmother, mi Abuelita, Rosinda Fletez gave me my spirit. Abuelita moved in with us a few days before I was born, raised me, and left when I went to college. She taught herself to read and write and at various points in her life was a gunslinger, a matriarch, an entrepreneur, a poet, and her grandson's playmate. Above all else she cultivated my creativity and my sense of self, and my first blessing in life was that she was there to watch over me.

Finally, I thank my son, Juan Michael Kort Smith-Pino, for teaching me what love is.

Contents

Chapter

Chapter 1

Introduction

I began my career as an experimental physicist working on a superfluid liquid He machine at the University of Florida. The concept of superfluidity, that is, a liquid with zero viscosity, presented what I thought were some of the most elegant demonstrations of physics, quantum mechanical or otherwise. It turns out that I was in good company, as this concept has been challenging physicists for decades. The focus of this thesis is exploring this behavior experimentally with a gas of ultracold atoms, which has its own unique challenges.

This introduction follows the analogy of a farmer tying a carrot onto the end of a stick, inspiring (some would say tricking) his horse to pull along a cart. For us the motivating carrot is one of nature's gifts, the liquid ^{4}He Bose-Einstein condensate (BEC). I will outline the historical significance, as well as some of the macroscopic phenomena that has made this system so inspiring. I will then give a sense of how "far away" the stick is to our horse (who doubles as an atomic physicist). Since our horse sees things in units of Bohr radii, I will focus on the microscopic theories that attempt to describe this system from the ground (state) up. Finally, I will present the contents of the cart: about 40,000 ^{85}Rb atoms. I will explain how 10^{-21} kg proves quite burdensome, as our horse measures weight not in kilos, but in Hz. I will conclude by explaining why both the horse and the farmer in this analogy consider this cargo to be so precious, as we hope 40,000 Bose-condensed ^{85}Rb atoms can be the seeds of our own carrot patch, nestled in our corner of the atomic physics community.

1.1 The carrot: Superfluid liquid He

Helium was first liquified in 1908 by Heike Kamerlingh-Onnes [1], where it was quickly applied as a coolant and largely forgotten about by Onnes, as he went on to discover superfluidity's affable cousin, superconductivity in 1911. This is a trend we would see some 100 years later in the atomic physics community, as the "hot topic" of late has been strongly interacting Fermi gases, with the occasional bosons again serving as coolants.

In 1932 interest in liquid ^{4}He again picked up, as a phase transition at 2.18 K was considered by Keesom and Wolfke [2], in light of work done by Onnes [3]. This was further investigated by Keesom and Clusius as they heated liquid Helium with a small, resistive wire and observed the ensuing temperature change [4]. They found the specific heat versus temperature to be discontinuous about what they termed the "λ" transition, named for the characteristic shape of the specific heat versus temperature near 2.18 K. This new phase of liquid He, below the λ-point, was referred to as He II. These were the first of many macroscopic observations manifested by a quantum state of matter.

Although anecdotal evidence had existed, the discovery of He II's superfluid nature did not come until 1938, when Kapitza and the team of Allen and Misener both independently and simultaneously measured the viscous flow of He II through a thin capillary. They found that at temperatures below the λ-point, the viscosity dropped several orders of magnitude, and became unmeasurable by their respective experiment's resolution [5, 6]. Kapitza would coin the term superfluid, and later receive a Nobel prize for his work.[1]

Superfluidity itself would end up being only one slice of the proverbial carrot, as experimentalists would measure a new kind of wave propagation, termed second sound. Instead of the usual matter wave propagation traveling at the speed of sound, second sound is the propagation of a thermal wave, where the non-condensed fraction of He II transmits this energy at its own

[1] This is a somewhat controversial area of Nobel history, as Allen and Misener were conspicuously left off of the prize. For a bit more in depth historical analysis I refer the reader to Griffin's wonderfully written review of superfluidity, complete with a timeline to further understand the Kapitza/Allen-Misener debate [7].

characteristic speed. A number of macroscopic theories for He II predicted such a phenomenon by (correctly) assuming that the non-condensed fraction of He II could be thought of as fundamental excitations within the system. These predictions were confirmed in a set of experiments by Peshkov in 1944 and 1946 [8, 9], and provided another dramatic example of macroscopic phenomena unseen in conventional liquids at the time.

Later, quantized vortex lines were experimentally verified by Hall and Vinen in 1956 [10], confirming the prediction of Onsager made in 1949 [11]. He argued that circulation about a closed loop would be quantized in units of h/m, owing to the single quantum state of the system. Quantized vortices are one of the cleanest examples of macroscopic phenomena fully explained by quantum mechanics.

Experiments aimed at understanding the microscopics of He II, specifically the elementary excitations of the system, came to fruition with inelastic neutron-scattering measurements. He II would not disappoint in its quirkiness, as experiments by Palevsky, Otnes and Larsson [12] confirmed the predicted existence of a local minimum in the dispersion. This minimum had been predicted by Landau, based on an elementary vortex excitation, and termed a roton. The "rotonic minimum", along with the complete dispersion for He II is shown in Fig. 1.1, as measured by Henshaw and Woods [13]. This particular feature of ^{4}He has been baffling physicists for years. The aforementioned Landau, as well as Feynman, Pitaevskii and Bardeen have all taken a crack at understanding the origins of the roton excitation [14, 15, 16], but a microscopic basis for such a minimum in He II has yet to be established.[2]

What we have discussed here are a number of *macroscopic* phenomena, that we know must be driven by the *microscopics* of the system. Also presented was the microscopic excitation spectrum, which had been qualitatively predicted by Landau's macroscopic theory. What is missing is a holistic approach that predicts these phenomological carrots, but is rooted in the quantum mechanics we know to be of fundamental importance.

[2] Unless you talk to a Monte Carlo theorist, in which case this is a fully understood problem, albeit with no analytical solution [17, 18, 19]

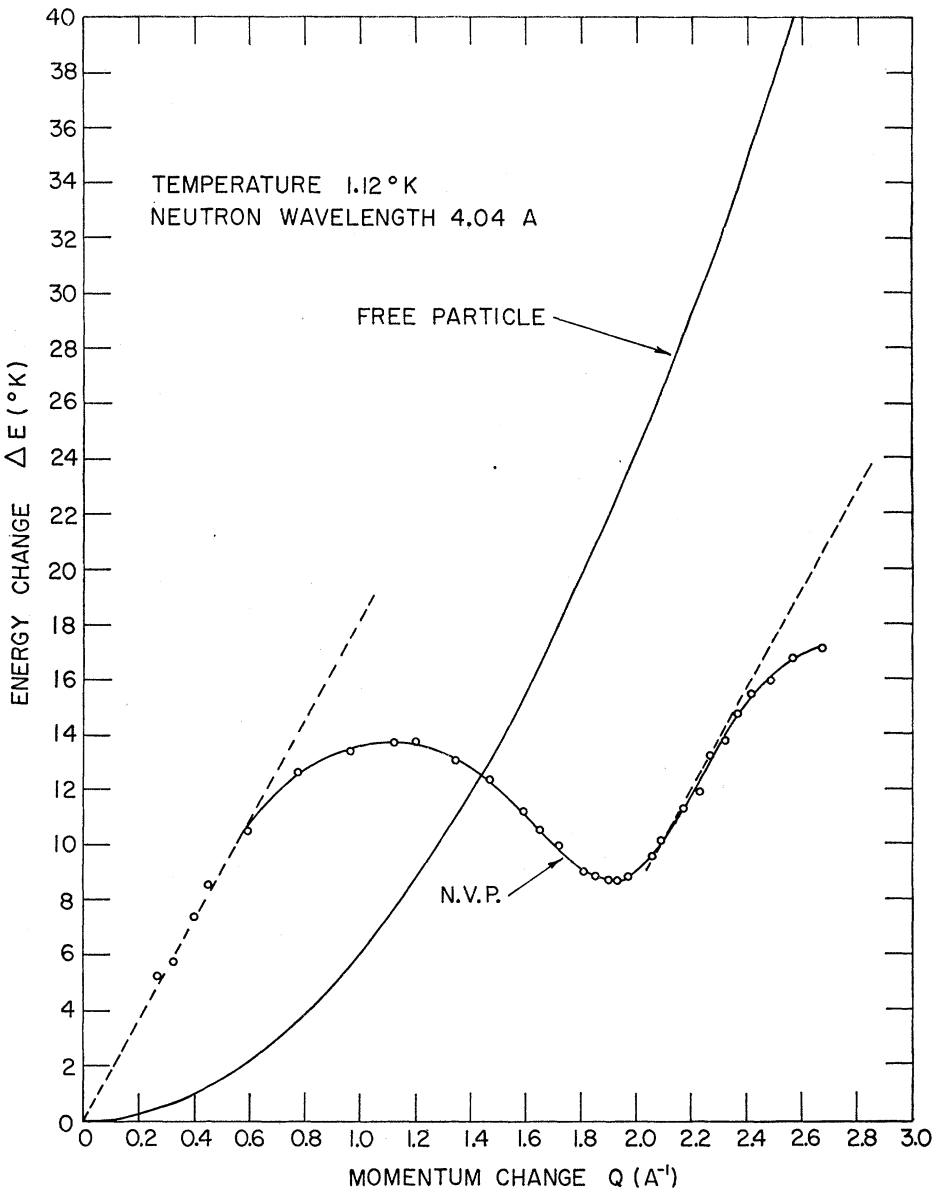

Figure 1.1: Reprinted from Henshaw and Woods [13]. Dispersion relation for He II, measured via inelastic neutron-scattering. The vertical axis is the measured energy of the excitation, while the horizontal axis corresponds to the momentum of the excitation. Note the local minimum, known as a roton excitation, as well as the linear dependence the energy has on the momentum for small excitations. This linear dependence is a signature of a collective, phonon excitation.

1.2 Theoretical treatments: But how long is the stick?

Following our analogy, the length of the stick could be thought of as how far we horses have to go to get to this carrot. I will first briefly describe the approaches taken to understand the carrot on the surface, in a macroscopic way, as this was the dominant line of thinking for quite some time. I will then go into more detail on the current state of the theory of interacting Bose gases, with a microscopic approach in mind.

1.2.1 Macroscopic theories: the carrot's perspective

A number of different theoretical treatments were developed to understand the superfluid, either in parallel, or in some cases preceding the experimental progress. Some of these approaches, particularly the work of László Tisza [20, 21, 22], extended the BEC framework (calculated for an ideal, non-interacting gas) put forth by Fritz London [23] to a macroscopic basis. However, an alternate, independent, and highly successful approach was taken by Lev Landau, who *completely ignored* the bosonic nature of ^{4}He, yet also managed to predict much of the phenomena laid out in the previous section. Landau's model relied on treating He II as being composed of both normal component that resembled ^{4}He above the λ-point and a superfluid component. He made great progress with this by quantizing the hydrodynamic equations for the superfluid component of He II, and postulating that the normal component was actually thermally excited elementary excitations. This "two-fluid model" was quite successful and thus was taken as the gold standard for He II physics, with He II's BEC nature largely ignored in some circles. In essence, this was a macroscopic theory that ignored the most fundamental characteristics of our carrot: its bosonic flavor.

1.2.2 Microscopic theories: the horse's perspective

The first microscopic theory taking into account the interactions in a degenerate Bose gas was put forth by Bogoliubov in 1947 [24] to develop a deeper understanding of superfluidity. A

number of key assumptions were made by Bogoliubov, and our thinking about BEC is dominated to this day by these assumptions. He first assumed the system was sufficiently dilute so that only pair-wise interactions were probable, and dismissed 3-body interactions. He also assumed that the system was at low temperatures, much lower than the condensation temperature, T_c. He further asserted that collisions were at low enough energies that the scattering amplitude reduced to the low-energy limit of the s-wave scattering length a. This last assumption lets us ignore the details of the inter-atomic potential at short-range, provided the potential gives the correct value of a. Lastly, the number of particles in the condensed, zero-momentum state is so large one may subtract or add a particle to that state and not affect the overall behavior of the system. This was crucial to his work and is now famously referred to as the Bogoliubov prescription.

From his work followed two important results. First is the Bogoliubov dispersion law for a condensate

$$\epsilon^2 = \frac{p^2}{2m}\left(\frac{p^2}{2m} + 2gn\right) \tag{1.1}$$

where ϵ and p are respectively the energy and momentum of the excitation, and m the mass of the boson. The interactions are characterized by the mean-field energy, gn, where $g = 4\pi\hbar^2 a/m$, and n the number density.

This dispersion law, while failing to predict the roton feature observed in He II, does a nice job in the low-momentum limit, where $\epsilon \approx c_{\mathrm{BEC}} p$, and collective, phonon excitations travel at the speed of sound $c_{\mathrm{BEC}} = \sqrt{gn/m}$. This linear dependence for low momentum excitations is shown in Fig. 1.1.

Bogoliubov's dispersion relation also proved correct in the high-momentum limit, where $\epsilon \approx \frac{p^2}{2m} + gn$. Here, we have a typical excitation with momentum p, but with the kinetic energy modified by the mean-field energy, gn. These excitations are characterized as particle-like, and their quadratic dispersion, while not addressed in Fig. 1.1, has been confirmed by later experiments probing higher momentum [25, 26]. It is worth noting that when Bogoliubov developed these theories, He II was presumed to be the only Bose-condensed system, but 50 years later experiments

with weakly interacting dilute-gas BECs proved his results quantitatively correct [27].

Another important result from Bogoliubov's work is that it introduces us to the concept of competing length scales. In many ways, the probes presented in this thesis are probes of the different length scales in our system, and it is a concept that will be present throughout this work. Here, the competition shows itself as the crossover of an excitation between the phonon regime and the free-particle regime. The length scale associated with this crossover is known as the healing length, ξ, and is defined as

$$\xi = \sqrt{\frac{\hbar^2}{2mgn}} = \sqrt{\frac{1}{8\pi na}}. \tag{1.2}$$

In the world of condensed matter physics, this is referred to as the coherence length of the system. In atomic physics, the term coherence length has a unique meaning, but we mention this to give the reader a sense of its importance. This length scale also sets the minimum distance over which a condensate can spatially distort and, in a related sense, this length scale sets the minimum size of a vortex. Later, in Chapter 3, we will again touch upon the importance of ξ, but it is worth mentioning here that the wavevector associated with the inverse of this length scale is at the same momentum at which the anomalous rotonic minimum occurs in the dispersion relation of He II. Curiously, based on the given density [3] of He one can "back out" a scattering length for He II equal to 13 a_0, which almost exactly agrees with the predicted effective range of ^{4}He of 14 a_0 [28].

Physicists Lee, Huang, and Yang calculated the ground-state energy of an interacting Bose-gas in 1957 [29, 30]. They calculated the energy density of an interacting Bose gas to be

$$\mathcal{E} = \frac{gn^2}{2}\left(1 + \frac{128}{15\sqrt{\pi}}\sqrt{na^3} + \ldots\right) \tag{1.3}$$

Their results were calculated using a Fermi pseudo-potential method, but can also be calculated from within the Bogoliubov framework [31, 32, 33].

The result of Eq. 1.3 is a perturbation about the mean-field result, $gn^2/2$. The perturbation is referred to as the LHY correction to the mean-field energy, or simply the LHY correction. The dependence of the LHY correction on $\sqrt{na^3}$ shows the non-linearity of this expansion.

The quantum depletion of the condensate is defined as the fraction of the system that has a

finite, non-zero momentum, even at zero temperature. This excited fraction arises from interactions between the particles, and is given by

$$\frac{n - n_0}{n} = \frac{8}{3\sqrt{\pi}}\sqrt{na^3} \tag{1.4}$$

where n is the total density, and n_0 is the density of the condensed, zero-momentum component of the system. The similarities between Eq. 1.4 and the LHY correction (namely the $\sqrt{na^3}$ dependence) illustrate the importance of these excitations to the next-order correction of the mean-field energy. Furthermore, as pointed out by Ref. [32], the dominant contribution to the LHY correction are the repeated interactions between two excited particles, before they drop back into the condensed, zero-momentum state.

The next-next-order correction to the mean-field energy was soon investigated by Wu [34] in 1959, shortly after Lee, Huang, and Yang's result. He calculated the coefficient in front of the logarithm below

$$\mathcal{E} = \frac{2\pi\hbar^2 a n^2}{m}\left(1 + \frac{128}{15\sqrt{\pi}}\sqrt{na^3} + 8(\frac{4}{3}\pi - \sqrt{3})\ln(na^3)(na^3) + O(na^3)\right) \tag{1.5}$$

where the other terms of order na^3 are known to be as large as Wu's correction, and therefore must be taken into account. These terms are non-universal, as they depend on the details of the interatomic potential, including 3-body effects. A number of theorists have since calculated these terms for different model potentials [35, 36]. The logarithmic dependance on na^3 further shows the non-trivial nature of this expansion.

We are now presented with another competition amongst length scales: the scattering length a versus the interparticle spacing $n^{-1/3}$. As the corrections to the mean-field energy are all expansions of na^3, we will refer to this as the "diluteness parameter" of our system. This competition is of central importance to the work presented in this thesis, as our ultimate goal is to probe systems where na^3 is nonnegligible.

In the case of He II, however, we know all of the above treatments must be fundamentally flawed. The biggest red flag being that in liquid He, the range of the repulsive interaction, a, is

on the order of the interparticle spacing, meaning that $na^3 \sim 1$. Hence, a perturbative approach makes little sense. In addition, there is an attractive part to the He potential, which plays an unknown role [31]. Finally, because He II is a liquid, there also exist correlations not taken into account with a dilute-gas BEC theory.

With a system that *is* well described by such theories, however, we aim to tune the interactions to regimes where na^3 is no longer small and test these theories. The hope is that perhaps we would be left with something more closely resembling our carrot, superfluid liquid He.

1.3 In the cart: a spherical cow

Having salivated over the superfluid carrot for long enough (albeit held by a stick some 6 orders of magnitude away), we are left asking ourselves, "What exactly is it that we are pulling along in this cart, anyway?" The answer, which assuredly will surprise none of my former labmates, is that we have been pulling along a 2,000 pound cow. A spherical one, at that.

According to Wikipedia, a spherical cow is a metaphor for a "highly simplified scientific model of reality." Our strongly interacting dilute-gas BEC will be the model system, and the hope is that with this we can mimic the peculiar reality of superfluid ^{4}He. Our system is highly simplified in that we will be working with a different atomic species, in its gaseous phase, no less. The hope is that some of the properties that have been discussed might be universal enough that they can be seen in this cold atomic system when we also approach regimes of large na^3. Furthermore, as we are able to continuously tune the interactions to such a complicated regime starting from a relatively simple system (the weakly interacting condensate) we would leave ourselves a trail of breadcrumbs to find our way back home.

In the field of cold-atom physics, this has been a highly successful model. Dilute atomic gases offer amazing amounts of control, and in many cases, a tunable amount of complexity. The trapping potentials of these systems, for example, are completely determined by the experimenter. Through manipulation of such potentials, cold-atom systems have been able to demonstrate such phenomena as Anderson localization [37], Josephson junctions [38] and Mott insulator transitions

[39], to name a few.

More recently, the push has been to tune the interactions themselves via a magnetic-field Feshbach resonance. This work, primarily done in fermionic systems, has been fruitful in measuring many universal properties of Fermi systems [40, 41, 42]. Further, one of the leading areas of research in ultracold Fermi gases is not only the mimicking of condensed matter systems, but the measurement techniques employed to study them as well [43].

For bosonic systems, Feshbach resonances have primarily been used to minimize interactions [44, 45]. As I will discuss in the next section, a major motivation for this line of research is the avoidance of the major tradeoffs inherent in studies of strongly interacting BECs. For strongly interacting Fermi systems, such compromises need not be made, as the Fermi statistics nullify such effects.

1.3.1 A hurried bull: ^{85}Rb

In the laboratory, we know that a spherical cow is never quite the right picture to paint, as cows tend to be docile and stationary targets. The systems we are herding tend to be heated and fast moving. In a word, temperamental. We thus refine the metaphor for laboratory work and refer to our system as the "spherical bull."

Our bull of choice is an ultracold cloud of Bose-condensed ^{85}Rb atoms. Such a system offers the same magnetically tunable Feshbach resonance that has proved so useful to the study of strongly interacting Fermi systems, albeit with some new tradeoffs, unique to bosons (every bull has its horns, so they say).

Carefully measured in Ref. [46], the s-wave scattering length is described as

$$a = a_{bg}\left(1 - \frac{\Delta}{B - B_{peak}}\right) \tag{1.6}$$

where $a_{bg} = -443(3)\ a_0$ is the background scattering length, $\Delta = 10.71(2)$ G is the width of the Feshbach resonance, $B_{peak} = 155.041(18)$ G the center of the resonance, and B is the aforementioned magnetic field we tune to manipulate a. A picture of our Feshbach resonance is shown in Fig. 1.2.

For all of the work presented in this thesis, we will be studying our condensate in the regimes of positive scattering length. The parameters for the Feshbach resonance in ^{85}Rb are listed in Table 1.1. Also included in the Table are the other popular Feshbach resonances in the different alkalis that have been Bose condensed.

Table 1.1: Feshbach resonance parameters for the most popular resonances in the different bosonic species that have achieved degeneracy. The ratio $|\Delta/B_{peak}|$, is useful in assessing the feasibility of studying a resonance, in terms of both the necessary magnetic field stability, as well as the range over which one must alter the magnetic field to access large na^3. Much of this information has been compiled in Ref. [47]. It is interesting to note that, aside from ^{85}Rb, every other Feshbach resonance listed applies to atoms in a high-field seeking state. In other words, ours is the only resonance occurring in a system that is magnetically trapable. This perhaps speaks to the lack of popularity of magnetic traps in the 21$^{\text{st}}$ century. We will later see that it is only through the unique advantages provided by magnetic traps that we are able to probe regimes of large na^3.

	^{85}Rb	^{7}Li	^{23}Na	^{39}K	^{87}Rb	^{133}Cs
$a_{bg}(a_0)$	-443	-25	62	-29	100	1720
$\Delta(G)$	10.7	-192.3	-1.4	-52	0.21	28.7
$B_{peak}(G)$	155.04	736.8	1195	402.4	1007.4	-11.7
$\lvert\Delta/B_{peak}\rvert$	0.07	0.26	0.001	0.13	0.0002	2.5

Now cast as experimental matadors, we must be mindful of our bull's horns. In the case of strongly interacting ^{85}Rb, both horns have to do with the limited timescales available to probe our system, with one horn being three-body recombination, and the other rapid density oscillations.

When ^{85}Rb was first considered for evaporation, the large a_{bg} listed in Table 1.1 was seen as promising. It was thought that evaporation would be straight forward, with the rethermalization rate going as the collision rate, and thus proportional to a_{bg}^2. The hidden truth, however, is that in ^{85}Rb inelastic collisions tend to dominate, with both two-body and three-body mechanisms playing a prominent role. Eventually, experimenters were able to overcome inelastic loss, either with more stages of laser cooling prior to evaporation [48] or via sympathetic cooling [49, 50], and achieved temperatures low enough for condensation.

The problem of inelastic, three-body recombination would prove to be a stubborn one, however. The rate for this process, by which two atoms form a bound molecule and a third atom carries

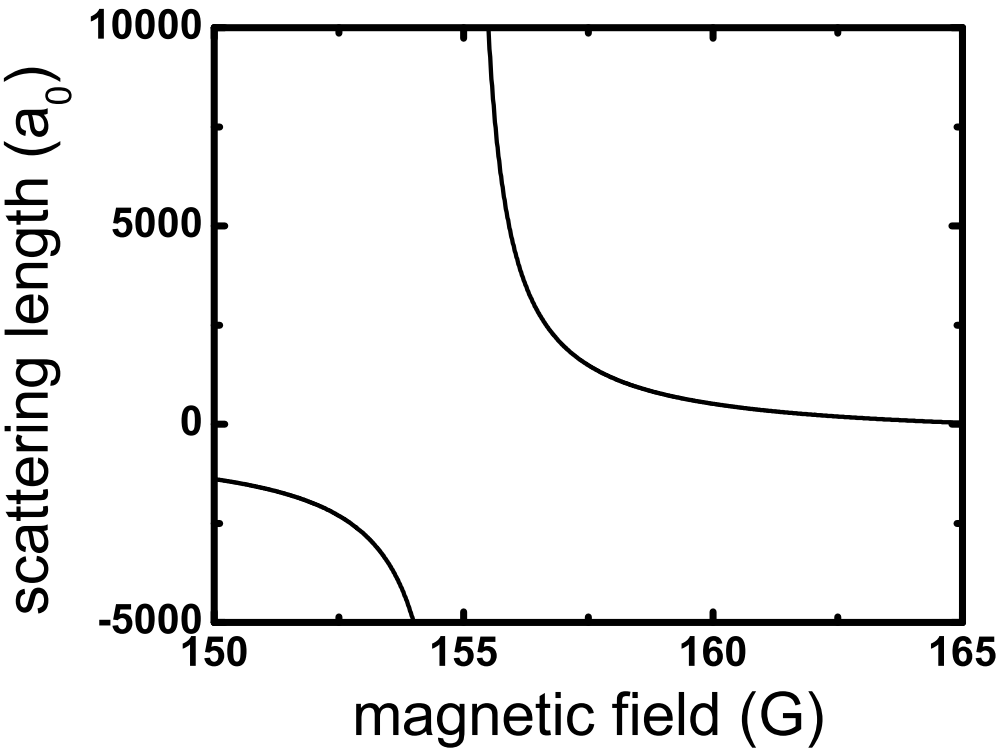

Figure 1.2: The donkey pulling the experimenter's cart: the ^{85}Rb Feshbach resonance at 155 G. Using this scattering resonance, we tune the scattering length from small a, corresponding to weak interactions (where the physics is well understood), to large a, corresponding to strong interactions. We probe the strongly interacting regime to better understand the beyond-mean-field physics of strongly interacting superfluids. The resonance is 11 G wide, allowing for a precise level of control, which makes ^{85}Rb ideally suited for studying such physics.

away the necessary energy and momentum, scales as a^4 [51]. The effects of this are both loss, as the atoms are no longer in their initial internal state, as well as heating due to the large amount of energy given to the third atom; this makes studying a BEC with large na^3 difficult.

An example of just how sharp the three-body horn is can be seen in the experiments done on the first ^{85}Rb BECs by Roberts *et al.*, where they were trying to measure beyond-mean-field physics [52]. These spectroscopic experiments measured the breathing modes, or density oscillations, of a trapped gas of ^{85}Rb near the Feshbach resonance. The oscillation frequency was known to be modified by the mean-field energy [53], and it was thought that the additional LHY correction could be measured in this same way. The experiment's undoing, however, was the aforementioned three-body recombination. Because the timescale for three-body events were faster than the timescale for the spectroscopy measurements (essentially the period of the trap) too much loss and heating was incurred and an LHY measurement proved impossible.

Further experiments of strongly interacting ^{85}Rb were performed in our group, using a second-generation BEC machine, and these met with success, having dodged the three-body horn by taking advantage of Bragg spectroscopy, a relatively quick measurement compared to 3-body rates [54]. These experiments, however, were not able to get out of the way of the second horn, and were ultimately limited by the same density oscillations that were originally being measured by Roberts *et al.*. Probes of high na^3, after all, need a relatively constant n. This horn is unavoidable as well, as the size of the condensate in the trap is set by the interactions in the gas. Hence, when we use the Feshbach resonance to change a, the BEC is no longer at its equilibrium size and a breathe oscillation ensues.

Such is life for our experimental bull fighter. In order to have success in his encounter with ^{85}Rb, he must not only probe the beast quickly (before being poked by the horn of three-body loss), but also distract the bull long enough so as to avoid the horn of rapid density oscillations. Playing the role of the red cape used to distract the bull will be the relatively weak, spherical traps made possible with magnetic confinement. This suits our matador just fine, as he wasn't planning on winning any popularity contests in the 21$^{\text{st}}$ century anyway.

1.4 Contents

This thesis, then, describes the design, construction and execution of both apparatus and measurements probing the different lengthscales of an interacting Bose gas, while maximizing the limited timescales available for such measurements.

In Chapter 2 I describe the implementation of our spherical magnetic trap, which was the major experimental change made to circumvent the limitations of rapid density oscillations. The third chapter lays the conceptual and analytical groundwork of Bragg spectroscopy, which is one of the few workable probes we have for these quickly decaying systems. In Chapter 4 I present a novel photon-counting technique for Bragg spectroscopy whereby the measurement is made on the Bragg light rather than the atoms. This chapter, together with Chapter 3, is intended to be a self-contained "cookbook" for the experimenter that would want to set up a similar system. In Chapter 5 I present our latest experiments using a different kind of spectroscopy based on a short-range quantity called the contact. Contained therein is preliminary data of what we hope will be our most accurate probe of the LHY correction. Finally, in Chapter 6 I touch upon the future directions of the strongly interacting BEC machine.

Chapter 2

BEC in a weak, spherical trap

In this chapter, I present our development of a trap and cooling scheme that has allowed us to confine ^{85}Rb BECs in a weak, spherical trap, which is necessary for the study of strongly interacting condensates. I will show that the dynamics of BEC systems are dominated by the mean-field energy. We model these dynamics, allowing us to characterize the breathing modes induced from changes in the scattering length. Through this modeling we can see the benefits of a weak, spherical geometry. The trap design will be presented, as will the evaporation scheme we have developed, and which we believe to be novel in atomic physics experiments.

2.1 The ansatz: ramping a

Central to the work of this thesis is the concept of establishing equilibrium after ramping the scattering length in time. This ramp is necessary, as we cannot create BECs at large na^3 due to large inelastic loss rates. Hence, to probe these strongly interacting regimes we must do so dynamically. A key to this approach, then, is the necessary time to establish such equilibrium. In other words, we will need to evaluate the "quickness", or conversely, the adiabaticity of our ramp in a.

The timescale associated with our ramp rate is set by $(\dot{a}/a)^{-1}$, to which we can compare different criteria for adiabaticity. In the past, we have argued [54] that the timescale to establish local, many-body equilibrium is set by $ma^2/\hbar$. For cases of $a > 0$, this is the timescale associated with the binding energy of a molecule. One could argue that the lengthscale, a, associated with

this timescale, is the lengthscale that sets the interactions of the many-body physics we study. This timescale for establishing equilibrium also happens to be the shortest and least demanding of the various arguments presented here.

A stricter criteria would be the timescale associated with the interparticle spacing, $n^{-1/3}$. From the Thomas-Fermi approximation, we can write the peak density of a trapped BEC as [55]

$$n_{pk} = \mu/g = \frac{m\omega_{ho}}{8\pi\hbar a}\left(\frac{15Na}{a_{ho}}\right)^{2/5} \tag{2.1}$$

where $\omega_{ho} = (\omega_\rho^2\omega_z)^{1/3}$ is the geometric mean angular trap frequency, $a_{ho} = \sqrt{\hbar/m\omega_{ho}}$ the harmonic oscillator length, and N the number of atoms in the condensate. This criteria for achieving equilibrium is given by $mn_{pk}^{-2/3}/\hbar$.

Finally, one might be a true "stickler", and argue that the most important lengthscale (in terms of being locally adiabatic) of the system is not a or $n_{pk}^{-1/3}$, but rather the healing length, ξ, where $\xi = 1/\sqrt{8\pi na}$. This is also the timescale of the chemical potential, or $\hbar/\mu$. For the experiments presented in this thesis, our system will always be in the Thomas-Fermi limit, where the dominant energy scale of the system is the interaction energy. We can thus write the chemical potential, μ, as [55]

$$\mu = gn \tag{2.2}$$

where gn will be referred to as the interaction energy, set by $g = 4\pi\hbar^2 a/m$ (as defined in Ch. 1) and the density n. Ignoring prefactors, this timescale also goes as $m(na)^{-1}/\hbar$. One could argue that this is in fact the relevant timescale, since the dominant energy of the system is, by definition, the chemical potential. We consider this the strictest criteria for achieving equilibrium.

How slowly one needs to ramp a in order to be adiabatic with respect to local, many-body equilibrium is an open question that is not answered in this thesis work. The hope is that future experiments, taking advantage of the previously unattainable time resolution offered by the trap geometry presented in this chapter will shed light on this outstanding question.

2.2 Motivation

As discussed, creating BEC of ^{85}Rb atoms has historically been a challenging endeavor. After completing the 2008 Bragg experiments [54], we had a system capable of studying strongly interacting condensates, yet we elected to essentially scrap that design in favor of something new, which would add further complications to an already difficult experiment. The most obvious question is, "why?"

2.2.1 Spherical cows, spherical traps, and BEC dynamics

Just as the spherical cow provided a simplified *model* of reality, the spherical trap, provides a simplified *realization* for our model. In other words, working with such a trap should make the experiments performed therein easier for the concerned theorist. In our 2008 publication [54], we presented no fewer than *five* different theoretical interpretations, knowing all five to be wrong in one way or another. I mention this to illustrate the theoretical complexities associated with BEC in the strongly interacting regime. In simplifying the trap geometry, we garner achieve a system that is that much easier to interpret for the theorists.

The second, and driving, motivation for implementing a spherical geometry is the need to probe our system for longer times. As discussed, we are only able to produce condensates at reasonably small values of $a \sim 100\ a_0$, and so must then quickly change a to probe large values of na^3. The equilibrium condensate size, however, is set by the interaction energy, gn, in the Thomas-Fermi limit. We express this as the radius of the BEC in the x direction, in terms of N and a, for a harmonic confining potential

$$R_x = \frac{1}{\omega_x}\sqrt{\frac{2\mu}{m}} = \frac{1}{\omega_x}\sqrt{\frac{\hbar\omega_{ho}}{m}}\left(\frac{15Na}{a_{ho}}\right)^{1/5}. \tag{2.3}$$

This sets another timescale, which is the timescale to establish an equilibrium density profile in the trap. This time can be defined as R_x/c_{BEC}, where $c_{\mathrm{BEC}} = \sqrt{gn/m}$. If we again ignore prefactors R_x/c_{BEC} goes as $1/\omega_x$. However, a quick (relative to $1/\omega_x$) ramp in a is unavoidable for the reasons discussed. The result is an induced expansion to accommodate the extra interaction

energy that was just dumped in. As we will see, the subsequent BEC dynamics, in particular density oscillations induced by a sudden change in a, give rise to a density that is rapidly changing in time. This time-varying density will ultimately limit the time over which we can probe the large na^3 condensate.

We take, for example, our Bragg experiments of 2008 where the measurements were completed before the density fell to 30% of its original value. At the largest values of na^3, this criteria allowed for interrogation times of 90 μs. Using square pulses of light, this corresponds to a Fourier-limited rms width of 4 kHz ([49]). This makes observations of beyond-mean-field LHY corrections to the BEC energy, which are predicted to be on the order of 400 Hz, experimentally quite difficult. Our aim in designing a new trap is to be able to probe the condensate for longer times, as well as suffer less change in our overall density. This was our primary motivation for developing a spherical trap.

2.2.1.1 The Pérez-Garcia model

To better understand the breathe mode excited by a rapid change in a, we use a model developed by Pérez-Garcia *et al.* [56] to simulate the BEC dynamics. This is a variational model that describes the condensate with a simple gaussian density profile that has a characteristic rms width of w_ρ (w_z) in the radial (axial) direction. The results are given in the form of these coupled differential equations [56]

$$\ddot{\mathrm{w}}_\rho + \omega_\rho^2 \mathrm{w}_\rho = \frac{\hbar^2}{m^2}\left(\frac{1}{\mathrm{w}_\rho^3} + \sqrt{\frac{2}{\pi}}\frac{Na}{\mathrm{w}_\rho^3 \mathrm{w}_z}\right) \tag{2.4}$$

$$\ddot{\mathrm{w}}_z + \omega_z^2 \mathrm{w}_z = \frac{\hbar^2}{m^2}\left(\frac{1}{\mathrm{w}_z^3} + \sqrt{\frac{2}{\pi}}\frac{Na}{\mathrm{w}_\rho^2 \mathrm{w}_z^2}\right) \tag{2.5}$$

The stationary solutions for the widths (w_{ρ_0}, w_{z_0}) are given by the real solutions of [56]

$$\lambda^{2/3}\frac{\mathrm{w}_{z_0}\mathrm{w}_{\rho_0}^4}{a_{ho}^4} = \mathrm{w}_{z_0} + \sqrt{\frac{2}{\pi}}Na \tag{2.6}$$

$$\frac{\mathrm{w}_{z_0}^4 \mathrm{w}_{\rho_0}}{\lambda^{4/3} a_{ho}^4} = \mathrm{w}_{\rho_0} + \sqrt{\frac{2}{\pi}}Na\frac{\mathrm{w}_z}{\mathrm{w}_\rho} \tag{2.7}$$

where $\lambda = \omega_\rho/\omega_z$ is the aspect ratio of the trap. For non-critical calculations, where a 10% error in the size is of no consequence, we can approximate these stationary solutions with analytic solutions for w_{ρ_0} and w_{z_0}, given by [56]

$$w_{\rho_0} = \lambda^{1/45}\left(\frac{\sqrt{2/\pi}}{15}\right)^{1/5} R_\rho \tag{2.8}$$

$$w_{z_0} = \lambda^{-28/45}\left(\frac{\sqrt{2/\pi}}{15}\right)^{1/5} R_z. \tag{2.9}$$

These solutions are valid in the Thomas-Fermi limit, which is defined here as $\sqrt{\frac{2}{\pi}}Na \gg a_{ho_\rho}$. This model is most useful for scaling arguments, because although the condensate density profile is not a simple gaussian, its radius is linear with w.

Using the Pérez-Garcia model, we can simulate the predicted breathing modes induced by a rapid change in a for condensates. For example, we consider 4×10^4 BEC atoms and a mean trap frequency of $\omega_{ho} = 2\pi \times 40$ Hz, which are conditions similar to our 2008 experiments in Fig. 2.1. We plot the normalized density of the BEC versus the time after a 10 μs ramp from $a = 100\ a_0$ to $a = 500\ a_0$. As one can see, a breathe oscillation is induced, and the density decreases versus time.

The different colored lines in Fig. 2.1 correspond to traps with different aspect ratios $\lambda = \omega_\rho/\omega_z$. The simulation makes apparent the benefits of working with an aspect ratio of 1 (red line), which corresponds to a spherical geometry. With other aspect ratios, with the same geometric mean trap frequency, there are actually two breathe modes induced corresponding (in the non-interacting case) to twice the radial and axial trapping frequency. This is most easily seen in the time dependence of the sizes of the clouds, as shown in Fig. 2.2. The radial frequency corresponds to the faster oscillation (Fig. 2.2(b)) while a slower breathe (Fig. 2.2(c)) occurs due to the axial confinement. It is the shorter timescale radial breathe that dominates the initial density evolution of the condensate. This motivates us to implement a spherically symmetric trap which has no preferred radial direction.

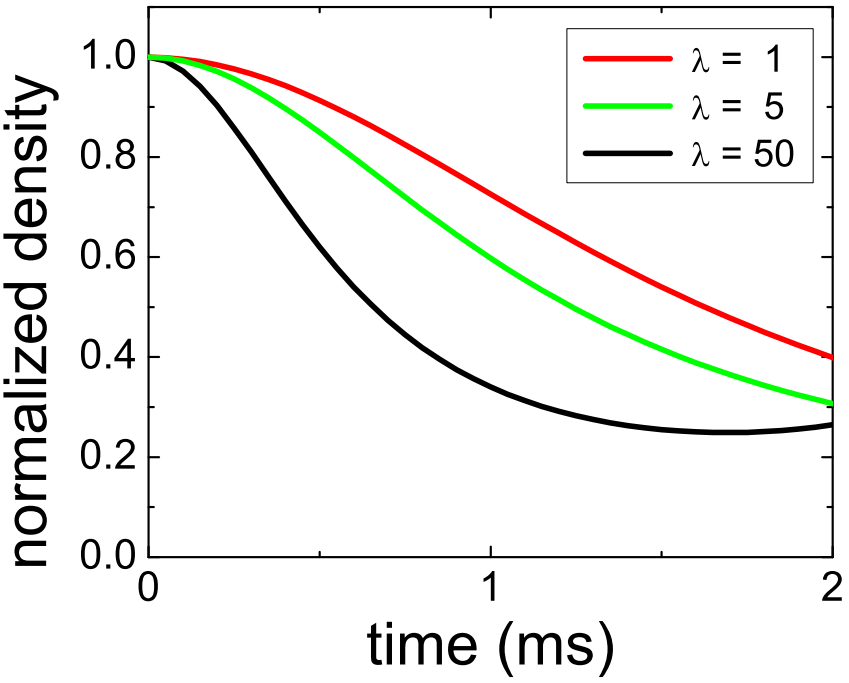

Figure 2.1: Simulated breathe from a quick jump in a. The density (n), normalized to the initial density, is displayed on the vertical axis. On the horizontal axis is time, measured after the jump from $a = 100\ a_0$ to $a = 500\ a_0$. Different colored curves represent traps of different aspect ratios $\lambda = \omega_\rho/\omega_z$. A spherical aspect ratio ($\lambda = 1$, red curve) gives the slowest breathe and hence the longest interrogation times at a relatively constant n. This simulation is done with a BEC of 4×10^4 atoms and a mean trap frequency of $\omega_{ho} = 2\pi \times 40$ Hz.

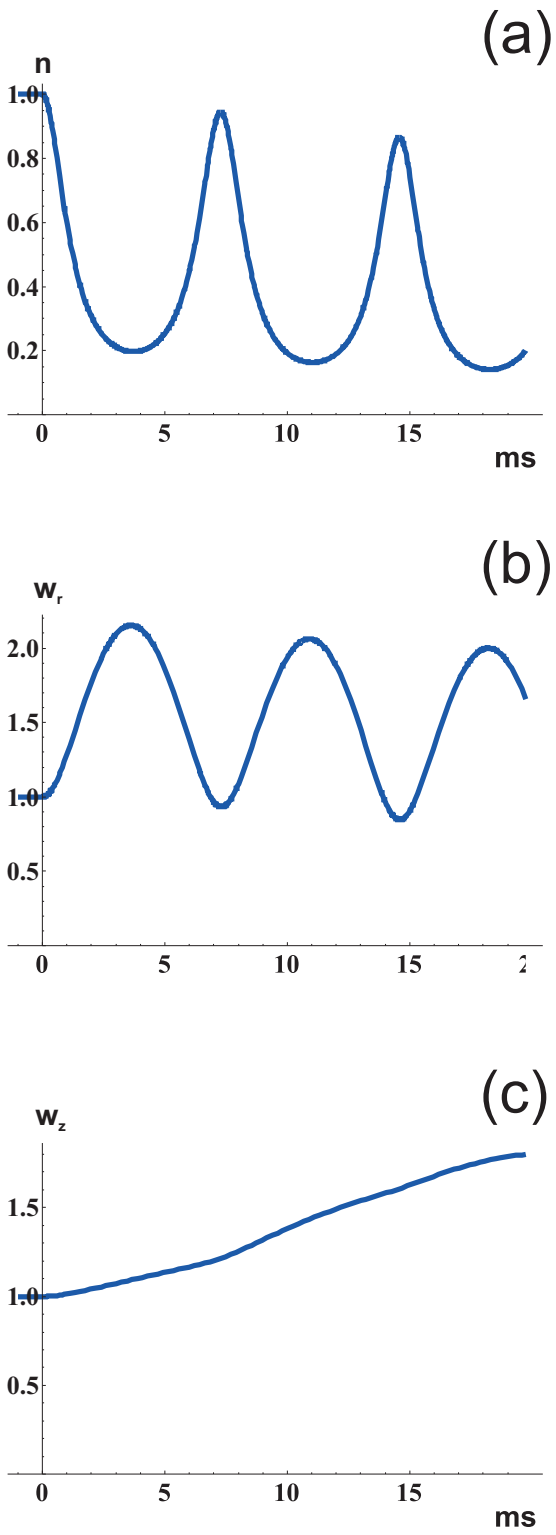

Figure 2.2: Illustrating how the larger trap frequency (ω_ρ) sets the timescales for breathe. This simulation is done with a trap whose radial confinement (ω_ρ) is five times larger than the axial confinement (ω_z), giving an aspect ratio of $\lambda = 5$. In (a) we plot the normalized density (vertical axis) against time (horizontal axis). The density oscillations correspond to breathes of the radial size, shown in (b), which in turn correspond to ω_ρ. The overall slope of the density oscillations (which can be considered the density time-averaged over $1/\omega_\rho$) correspond to the slow increase in the axial size of the condensate, which likewise corresponds to ω_z.

2.2.2 The weak shall inherit the trap

If we are going to all the trouble, then, of redesigning the trap for a spherical geometry, we would have some flexibility as to the mean trap frequency as well. From Eq. 2.1, we see that a lower mean trap frequency, while perhaps allowing us to probe longer, would also cost us in the initial density, which scales as $\omega_{ho}^{6/5}$. Hence, to probe the same value of na^3 in a weaker trap, we must ramp to a higher final value of a. We have simulated the dynamics that ensue for ramps to $na^3 = 5.4 \times 10^{-4}$ and plot these density oscillations in Fig. 2.3(a). This value of na^3 corresponds to an LHY correction to the energy density of 11%. As one might guess, the weaker traps always win this gambit and allow for the longest possible probes of BECs with large na^3.

While weaker trap confinements will make work more accessible from an experimental standpoint (e.g. computer control of ms pulses is much easier compared to μs pulses), there is no benefit in terms of resolving the interaction energy, as shown in Fig. 2.3(b). Here we see density oscillations plotted against the normalized time after the ramp. When considering direct probes of the interaction energy, the relevant normalization is the timescale associated with the chemical potential, $\hbar/\mu$. What Fig. 2.3(b) illustrates is that regardless of ω_{ho}, we suffer the same amount density drop when comparing the breathes at constant $t\mu/\hbar$. We nonetheless set out for a weak geometry as earlier attempts to create ^{85}Rb BEC in traps of large ω_{ho} proved unsuccessful [49].

2.3 Trap design

Having laid out the gauntlet, our challenge loomed: design a weak, spherical trap to work with ^{85}Rb BECs near the 155 G Feshbach resonance. Magnetic traps offer the advantage of being extremely flexible in their design, with the trap aspect ratio being completely controllable via the relative amounts of currents in the magnetic trap coils. In addition, weak geometries imply large amounts of gravitational sag. This sag introduces undesirable anharmonic components in an optical trap design (the other standard for cold atom experiments) that magnetic traps are inherently less sensitive to, due to the large coil spacings that define the trapping potential.

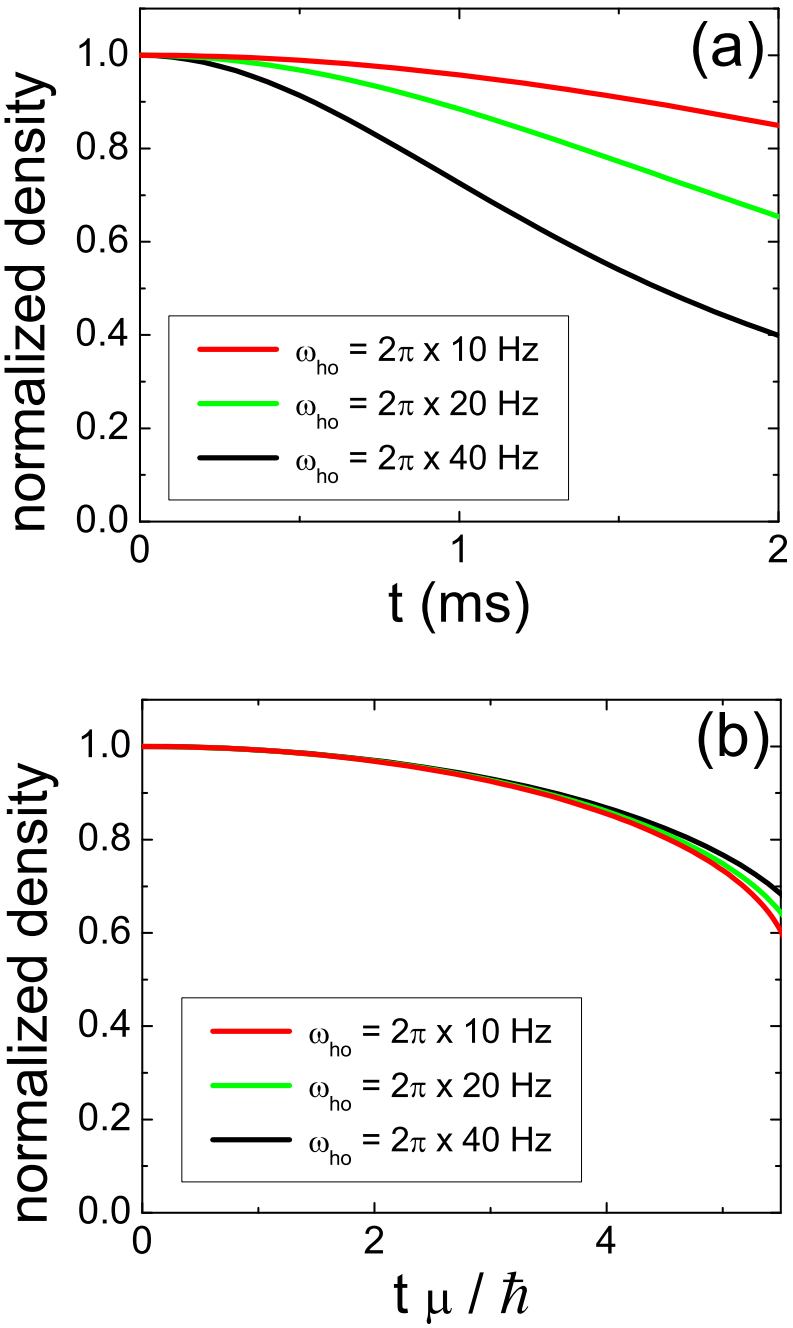

Figure 2.3: Breathing mode induced by a quick jump of a to achieve a large $na^3 = 5.4 \times 10^{-4}$. In (a) the vertical axis is the normalized density, and on the horizontal axis is the time after the jump to large a. Different colored curves represent traps with different mean trap frequencies. This illustrates the advantage of working with a relatively weak trap, which gives the longest interrogation times possible at constant density. In (b) we plot the same normalized density breathe, only now versus the time after the jump normalized to $\hbar/\mu$, the timescale associated with the chemical potential. This demonstrates how even for the slower breathes at small $\omega_{\rm ho}$ (seen in (a)), we are still subject to the same drop in density for the same $t\mu/\hbar$.

Our magnetic trap is in the Ioffe-Pritchard style; more in-depth discussions of the Ioffe-Pritchard design can be found in [57, 52], while details particular of our geometry are in Ref. [49]. What we have done in this work is reconfigure the currents and provide an additional vertical field (supplied by the cart coils) to achieve our desired trapping potentials and bias field.

The relevant parameters for the coils used in our magnetic trap are listed below in Table 2.1, including the currents we presently use to make spherically symmetric BECs. The bias fields, gradients and curvatures are all taken from Scott Papp's thesis [49], except for the cart parameters, which are new to this trap.

Table 2.1: Relevant parameters measured for the coils used in the 10 Hz spherical trap. Many of these can be found in Scott Papp's thesis [49]. The currents we list here for the trap might change as much as a few percent (in particular the cart coil) for slightly different optical trap alignments, as the currents are used to align the magnetic trap to the optical trap. Currents were measured using the in-loop Hall current sensors, September 2010.

	Bias ($\hat{z}$)	Pinch ($\hat{z}$)	Ioffe bars ($\hat{\rho}$)	cart ($\hat{y}$)
Bias field (G/A)	1.61	0.515		1.02
Gradient (G/cm/A)			1.04	
quadratic (G/cm^2/A)	0.097	0.695		
current (A)	47.3	167.2	167.2	30.2

To give a conceptual picture of the Ioffe-Pritchard design, we present a cartoon of the coils involved in the trap in Fig. 2.4. What this geometry gives you is a large bias field in the $\hat{z}$ direction, with the magnitude of the magnetic field having a local minimum in the center of the trap. The potential felt by our atoms is due to the Zeeman energy, where $U_{\text{Zeeman}} = \mu|\vec{B}|$. Because it is only this magnitude of the magnetic field we care about, the fields orthogonal to $\hat{z}$ contribute to the trapping potential only by adding to the large bias field in quadrature.

Roughly half of the large bias field (B_0) in $\hat{z}$ is provided by the so-called bias coils, depicted in blue in Fig. 2.4. These are in a Helmholtz configuration, and function only to produce this uniform field. For the previous, all-optical trap, which was used for our 2008 experiments, these coils provided the entirety of the bias field, as well as the axial confinement due to a slight curvature,

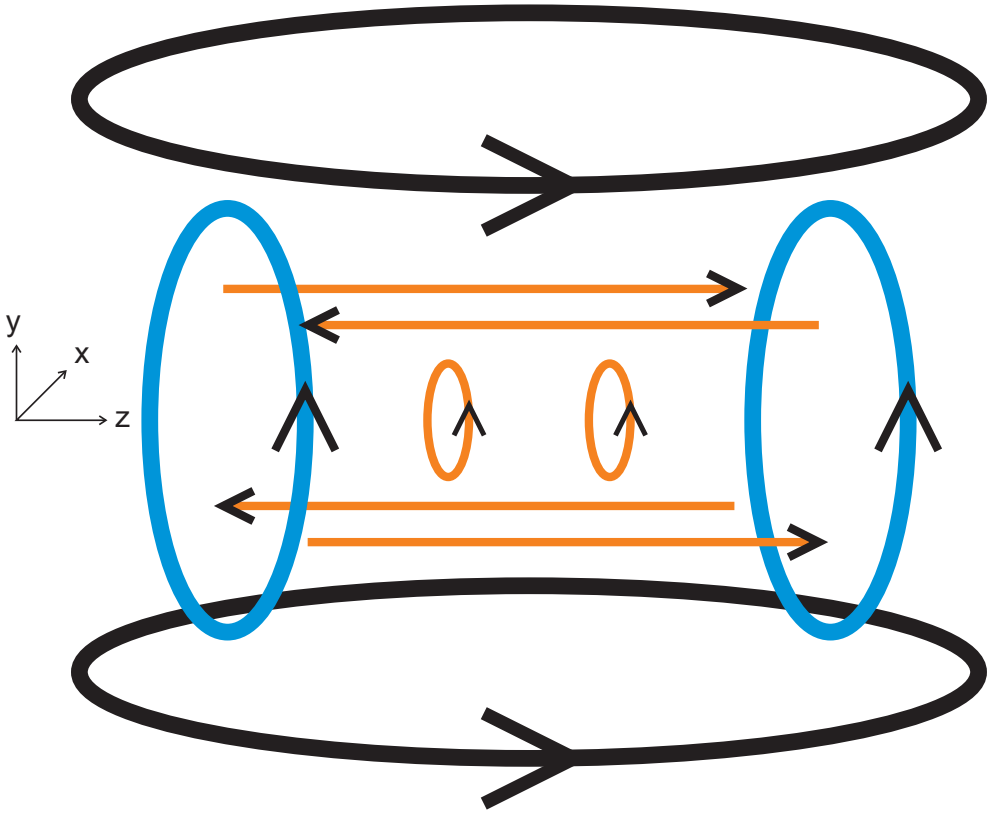

Figure 2.4: Cartoon picture of coils used to make the 10 Hz spherical trap. Bias coils in blue, arranged in a Helmholtz configuration, produce a uniform field and provide roughly half the bias field along $\hat{z}$. The smaller loops of coil in orange are the pinch coils, providing the other half of the bias field as well as confinement along z. The straight, orange wires are the Ioffe bars, and provide radial confinement when their linear, quadrupole gradient is added to the large bias field along z. Large black loops seen at the top and bottom are referred to as the cart coils. These provide a small bias field ($\sim$ 30 G) in the vertical direction and are used to adjust the center of the magnetic potential in y.

(see Table 2.1). This curvature, with a minimum at the center of the coil pair, results from the spacing between the coils being slightly larger than in the standard Helmholtz configuration.

Also seen in Fig. 2.4 is the pinch coil pair in orange. The current flows through these coils in the same direction as in the bias coils. This is not standard for the Ioffee-Pritchard trap, but we found it necessary to achieve our desired bias field with weak confinement. The function of these coils is two-fold. First, they add to the bias field, providing the other half of the needed 160 G. The field from the pinch coils also has a curvature along $\hat{z}$, providing parabolic confinement. This curvature is the dominant contributor to the axial confinement of the atoms.

Also seen in orange are the Ioffe bars, depicted by straight lines in Fig. 2.4. These bars share the orange color of the pinch coils to illustrate that they are electrically in series with the pinch coils. The function of these coils is to provide radial ($\hat{\rho}$) confinement to our atoms. Although the gradient they produce is linear (β_ρ), the resultant trap is parabolic in ρ. The key here is the large bias field (B_0) in the $\hat{z}$ direction. Again, the Zeeman energy of our weak-field-seeking state is proportional to the *magnitude* of the magnetic field because the magnetic moment of the atom adiabatically follows the field direction. When we add the bias field to the linear gradient produced by the Ioffe we are left $|B| = \sqrt{B_0^2 + \beta_\rho^2 \rho^2}$. For a large enough bias field ($B_0 \gg \beta_\rho \rho$), this can be approximated by $|B| \approx B_0 + \frac{1}{2}(\beta_\rho^2/B_0)\rho^2$, giving us a trap harmonic in ρ.

Finally, in black is another pair of Helmholtz coils, which we refer to as the cart coils. These work in the same way as the bias coils, providing a constant field, B_c, only this time in $\hat{y}$. The role of the cart coils is to shift the center of the magnetic trap position vertically, by effectively shifting the zero of the magnetic field produced by the Ioffe bars. This is illustrated in Fig. 2.5. If we focus on the fields in $\hat{y}$, then $B_y = \beta_y(y - y_0)$, where $y_0 = -B_c/\beta_y$ is the new center of the Ioffe gradient in y. This trap center shift will prove necessary to overlap this trap with the trap used for earlier stages of the experiment. This is required because the final confining potential in the new trap is so weak that gravitational sag is substantial (roughly 2.5 mm). Without the addition of the cart field, the atoms could not be loaded cleanly from earlier cooling stages of the experiment. This, we will see, is a key design consideration.

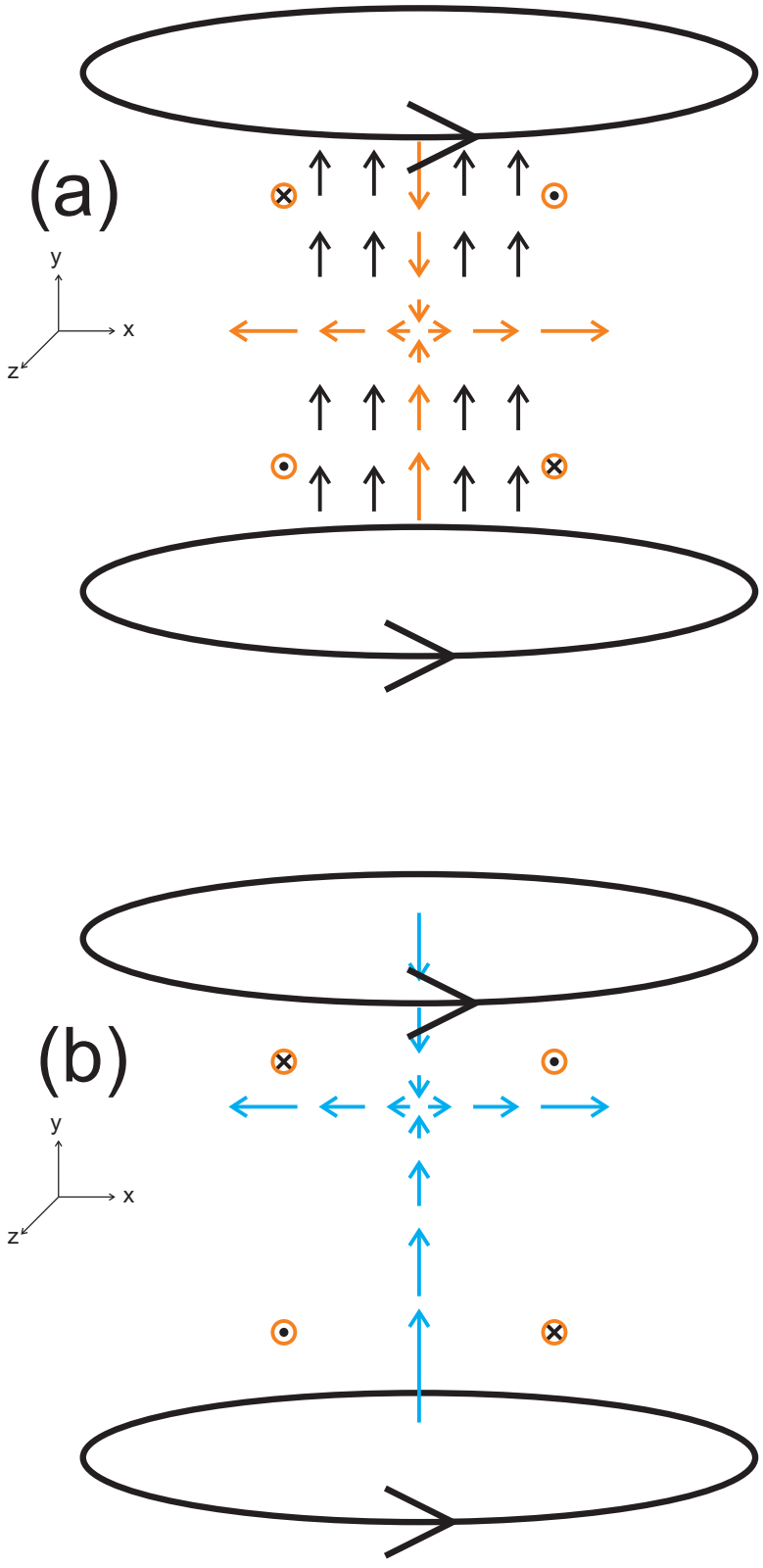

Figure 2.5: Cart coils lifting the center of the quadrupole potential for alignment of the spherical trap in y. In (a) we see both the direction and magnitude of the field generated by the Ioffe bars in the orange vectors. The black vectors represent the uniform field from the cart coils. In (b) we see the resultant field in blue. Notice this looks just like the Ioffe field (orange) in (a), only now offset in y, effectively shifting the center.

The resultant trap potential is modeled and shown in Fig. 2.6. An unexpected aspect of our spherical trap is the rotation of the primary axes of the trap by roughly 45 degrees, as seen in Fig. 2.6(c). We have found that this symmetry breaking of the primary axes of the trap is due to the pinch coils. Because they provide confinement along the $\hat{z}$ direction, we know that there must also be some curvature along the other directions to fulfill the requirements of Gauss' law, $\nabla \cdot \mathbf{B} = 0$. Invoking the known symmetry of the pinch coil geometry, we can assume that the field goes as $\mathbf{B}_{pinch} = (B_0 + B''z^2)\hat{z} - B''zx\hat{x} - B''zy\hat{y}$. We notice there are two crossterms here, $B''zx\hat{x}$ and $-B''zy\hat{y}$. Because our trap is always centered in x, but offset in y due to gravitational sag ($y_{\text{sag}} = \frac{mg}{\beta^2 B_0}$), it is the last term, in $\hat{y}$, whose crossterm features both z and y, that breaks the symmetry for a non-zero value of y. We only return to the primary axes of the trap if we eliminate both the effects of gravity as well as the cart fields we use to center the trap.

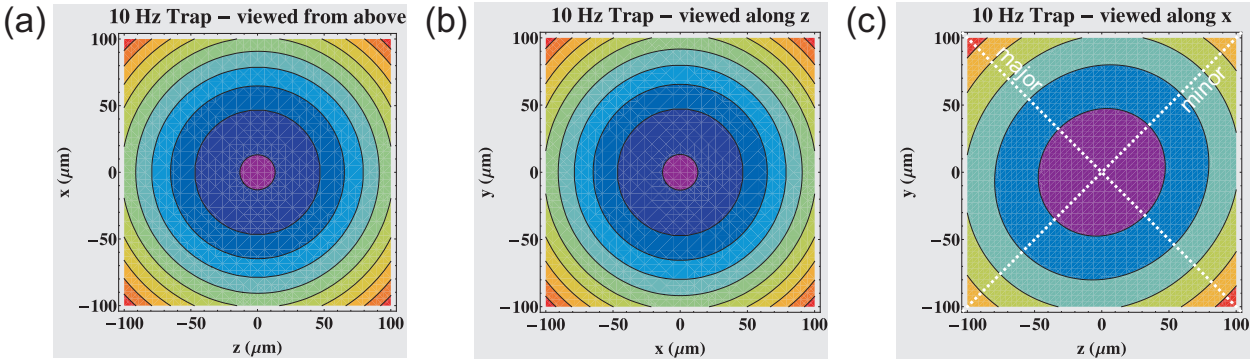

Figure 2.6: Contour plots for the 10 Hz spherical trap, as seen along the $\hat{y}$ (a), $\hat{z}$ (b), and $\hat{x}$ (c) direction. Darker colors represent lower potential energy. By eye it is clear that the trap is fairly spherical, except for the plots in (c). The reason for this are discussed in the text. We will define the "long" axis of the trap, with the weaker trap frequency as the minor axis ($y = z$), and the orthogonal direction, with the tighter trap frequency, as the major axis ($y = -z$).

Finally, we can ask ourselves how good we have done as trap-builders by measuring the trap frequencies directly with the atoms. The results of these measurements are shown in Fig. 2.7. Here, we have rotated the axes of the fits by 45 degrees with respect to the primary axes of the trap (the vertical, $\hat{y}$, and axial, $\hat{z}$, direction) so that the y' and z' positions correspond to the major and minor axes, respectively. We then fit the data to a sinusoidal oscillation. We measure trap

frequencies of 10.21(5) Hz in the $\hat{x}$ direction, and frequencies of 10.41(4) Hz and 9.39(7) Hz for the major and minor axes of our trap. This ultimately gives us an aspect ratio of 10.41/9.39 = 1.1. Considering that our previous optical trap had an aspect ratio of 50, we consider this a successful endeavor.

2.4 Making ^{85}Rb BEC

In this section, I outline the cooling scheme we have developed for ^{85}Rb. The ideas presented here were new to us, and exploring these ideas represented some of the most exciting times in the lab. The basic concept is the same as that of many of the dual-species machines: use ^{87}Rb to sympathetically cool the more stubborn species, which in our case is ^{85}Rb. Sympathetic cooling provides the advantage of avoiding the scattering processes of ^{85}Rb that proved so painful for the original ^{85}Rb machine [58, 59] by outnumbering and overwhelming them with the good elastic collisions provided by another species. What we have developed is a new twist, with a cooling scheme that is truly sympathetic, empathetic even, all the way to quantum degeneracy. The results of our work are large, round, stable condensates and a scheme that could be readily applied to other systems as well.

We will breakdown each stage of the experiment in the following sections, but begin with a general overview diagrammed in Fig. 2.8 to help facilitate an understanding of both the entire experimental cycle, as well as the evaporation scheme used with the hybrid trap (a combination of the weak spherical trap and the optical trap), which is being presented for the first time. Much of the cooling process is standard in cold-atom experiments. The atoms are cooled from room temperature via optical cooling performed in a magneto-optical trap (MOT). From the MOT, we load atoms into a quadrupole trap (QT) to transfer them to a high-vacuum region of the experiment where they will be further cooled. It is here that ^{85}Rb is first sympathetically cooled, with direct radio frequency (rf) evaporation performed on ^{87}Rb in the traditional sense [60].

From the magnetic trap, we load the ^{85}Rb and ^{87}Rb gases into our hybrid trap. This is done in two stages as first we confine the atoms optically. We then turn on the 10 Hz spherical

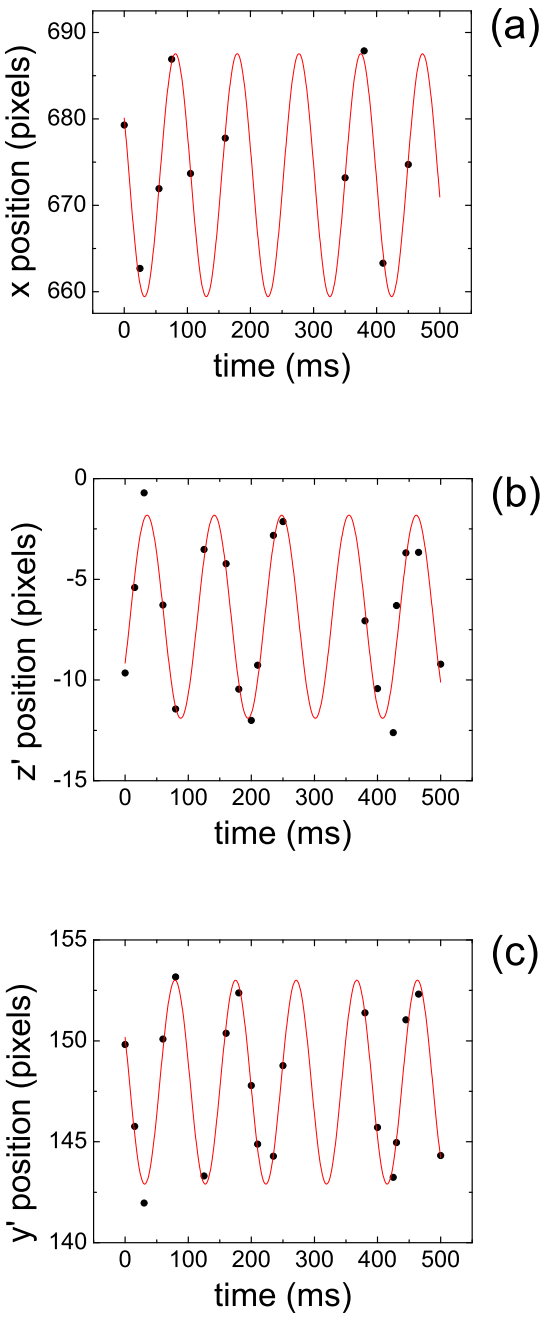

Figure 2.7: Slosh data for each of the principal axes of the trap, obtained from images of a thermal gas taken after time-of-flight with a 28 ms expansion time. This data gives trap frequencies of 10.21 $\times$ 9.37 $\times$ 10.41 Hz for the $\hat{x}$ (a), minor (b) and major (c) axes. For the minor and major axis slosh data, we have had to take our normal images, oriented in $\hat{y}$ and $\hat{z}$, and rotate them by 45 degrees. For the $\hat{x}$ data, we use a different imaging axis and camera.

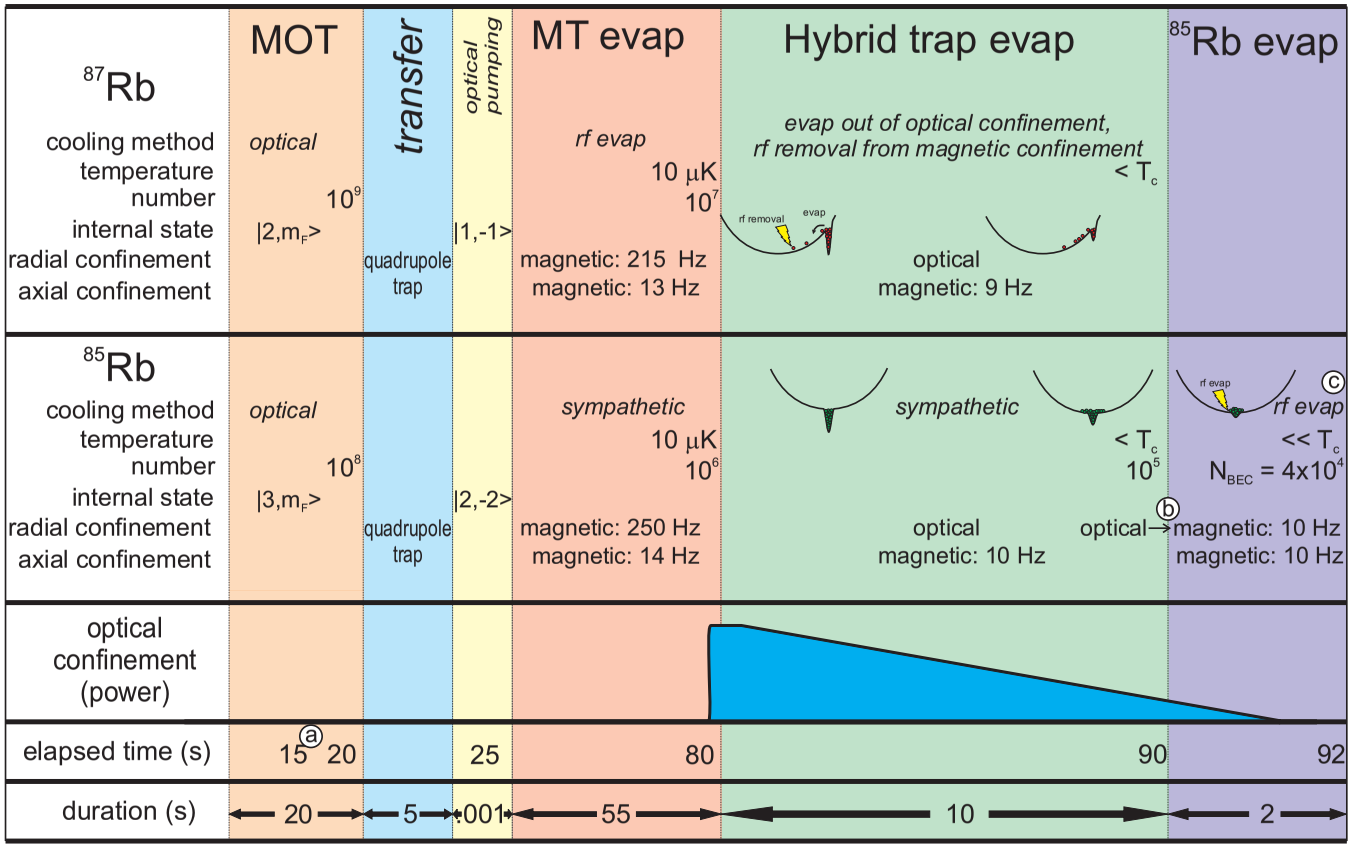

Figure 2.8: Big picture view of the duty cycle and cooling of our ^{85}Rb-^{87}Rb machine. Time is outlined on the horizontal axis (not to scale), with the respective parameters for ^{85}Rb and ^{87}Rb detailed in the figure. The hybrid trap evaporation is what we will be introducing in this section, as many of the concepts are new, and have not been discussed prior to this thesis. As we see from the figure, the confinement is due to the combination of a magnetic trap and an optical trap. The optical trap serves to both provide a mechanism to preferentially cool ^{87}Rb as well as to spatially overlap ^{87}Rb and ^{85}Rb, for efficient sympathetic cooling. The circled letters in the figure are further clarified as follows: (a) Note the ^{85}Rb MOT begins at 15 s. (b) During the ^{85}Rb evaporation the optical potential is giving way to the spherical magnetic trap, both cooling ^{85}Rb (via rf evaporation) as well as loading the weak, spherical trap. (c) This rf evaporation is different than most in that the rf knife is at a constant frequency versus time, while the aforementioned optical trap is weakened. This will be discussed more in Section 2.4.3.

magnetic trap described previously. The optical trap is aligned so that its position coincides with the equilibrium position of the ^{85}Rb potential. This optical trap position, however, is vertically offset from the equilibrium position of the ^{87}Rb potential due to the differential sag experienced by each species due to their different magnetic moments. Now lowering the optical potential has the effect of normal optical trap evaporation for the ^{87}Rb gas. The ^{85}Rb gas, on the other hand, is never directly evaporated on, but is spatially overlapped with ^{87}Rb, giving prime conditions for cooling all the way to quantum degeneracy sympathetically.

2.4.1 Laser cooling and the magnetic trap evaporation

The first step of bringing atoms from room temperature to quantum degeneracy is achieved via laser cooling in a magneto-optical trap (MOT). We find that we have better overall performance by loading more atoms from the MOT into the quadrupole trap (QT) by loading the atoms into a tight trap, which can confine atoms in the $|F = 3, m_F = 2\rangle$ and $|F = 3, m_F = 1\rangle$ states in addition to the $|F = 3, m_F = 3\rangle$ stretched state (previously only the stretched state was loaded). This effect can be seen in Fig. 2.9. Because we later optically pump the atoms into the desired final spin state, $|F = 2, m_F = -2\rangle$, (after transferring the gas from the QT to the magnetic trap), we are not as worried about atoms in other, non-stretched, spin states. In the end, higher ^{87}Rb number is better for our evaporation performance, since most of our cooling comes from the evaporation of ^{87}Rb atoms.

We load a much smaller number of ^{85}Rb atoms than ^{87}Rb atoms in the MOT so as to not load down the later stages of evaporation with the additional heat capacity. The reduction in the number of ^{85}Rb atoms is achieved with a couple neutral density filters that attenuate the ^{85}Rb MOT light to 50% of its previous value. We estimate that we now load an ^{85}Rb to ^{87}Rb number ratio of $\sim$ 1:10 in the two-species MOT. The atoms are further optically cooled (compressed MOT, see Ref. [49]) and subsequently loaded into a quadrupole trap and transferred to the science chamber.

This leads us to the first stage of evaporation, which is performed in the magnetic trap (MT). This trap is described in Ref. [49] and provides trapping for both ^{85}Rb and ^{87}Rb atoms in

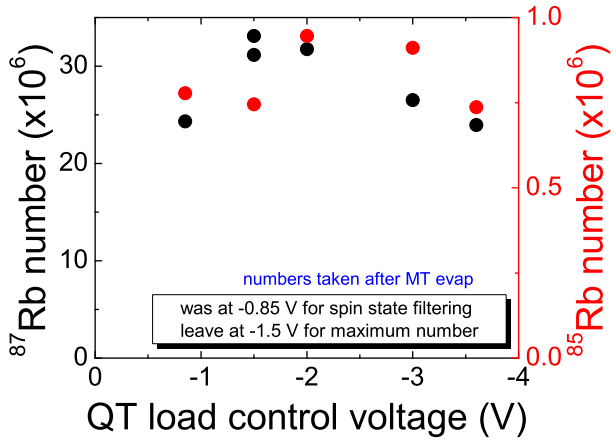

Figure 2.9: Quadrupole trap (QT) load after the MOT. In black, is the ^{87}Rb number after magnetic trap evaporation (left hand axis). In red is the ^{85}Rb number at the same stage of cooling, with the corresponding number on the right hand axis. Previously we worked with a weaker initial QT load (23 G/cm), which corresponds to a smaller current (horizontal axis), because of the additional spin-filtering this scheme provided. We later found this unnecessary for our new evaporation scheme, and now we load more atoms into the QT at a larger current (40 G/cm).

the $|F = 2, m_F = -2\rangle$ and $|F = 1, m_F = -1\rangle$ states, respectively, with measured trap frequencies of 215×12.5 Hz for ^{87}Rb. The corresponding trap frequencies for ^{85}Rb should be $\omega_{87}\sqrt{\mu_{85}/\mu_{87}}$, with μ_{85} and μ_{87} the corresponding magnetic moments of the ^{85}Rb and ^{87}Rb species being trapped, and ω_{87} the corresponding angular trap frequency for ^{87}Rb. In this trap, the ^{87}Rb gas is evaporatively cooled using rf transitions driving the ^{87}Rb atoms to the $|F = 1, m_F = 0\rangle$ state. The ^{85}Rb gas is cooled sympathetically through its thermal contact with the ^{87}Rb gas. We evaporate to a temperature of 10 μK, finding that this gives the best conditions for ^{85}Rb later on in the experiment.

After the rf evaporation in the magnetic trap, we load the gas into the optical trap. It should be noted here that the laser for the OT is no longer the 1030 nm ELS laser mentioned in Ref. [49]. We now use a multi-mode fiber laser at 1090 nm manufactured by SPI Lasers. After the ELS laser died, we tried a 1064 nm multi-mode fiber laser, but found that this light was resonant with a ^{85}Rb molecular transition, and we were not able to make condensates. We turn on the optical trap while the MT is still on, and then turn off the MT confinement. In Fig. 2.10, we look at the

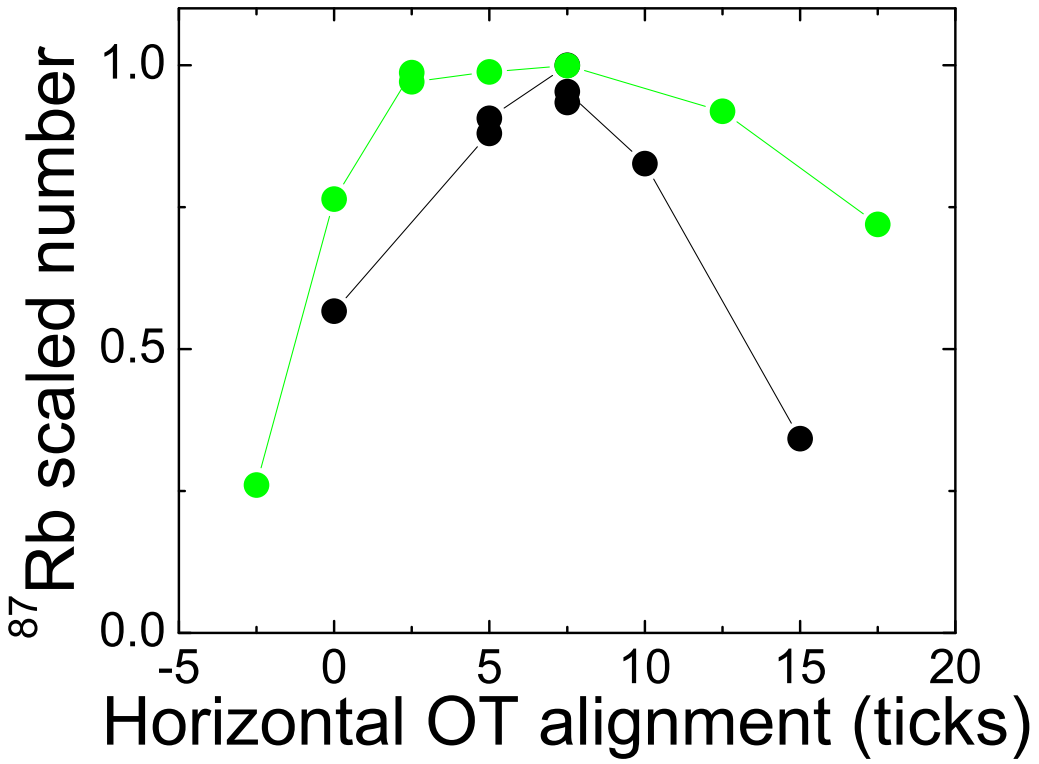

Figure 2.10: Optical trap loading techniques. On the vertical scale is the ^{87}Rb number, normalized to the peak number, after one stage of optical trap evaporation. On the horizontal axis is the position of the optical trap at the atoms, in the experimental units of "ticks" on our knob used for alignment. We find that by loading the optical trap earlier, while the magnetic confinement is still on (green points) we are less sensitive to the optical trap position than if we had used the technique of "catching" the atoms after turning off the magnetic trap (black points). This will prove crucial for optimizing both the load from the MT into the OT as well as the subsequent load from the OT in to the weak, spherical trap.

sensitivity of the OT load to the relative alignment of the MT and the OT. This is an important consideration since later on we will see that the alignment between the OT potential and that of the weak, spherical trap is crucial, but that the spherical trap center is not necessarily aligned with that of the MT. In the figure, we see that the current OT loading procedure is less sensitive to the OT alignment than a sudden transfer technique that we used previously.

2.4.2 Hybrid trap evaporation and the grooming of a ^{85}Rb BEC

We would like to take advantage of the sympathetic cooling afforded in an optical trap, but still be left with the spherical trap geometry we carefully designed for our new magnetic trap. At the end of the day, our solution seems somewhat straightforward: physically combine the two. We refer to this scheme as our "hybrid trap", and the evaporation and sympathetic cooling of atoms trapped in this configuration will be discussed in this section.

To develop a conceptual picture, we model the trap potentials for both ^{85}Rb and ^{87}Rb, in Fig. 2.11(a) and (b) respectively, at an early stage of the hybrid trap evaporation. On the vertical axis we show the total potential energy provided by the optical and magnetic traps, including the effect of gravity. The magnetic trap provides a broad, parabolic confinement, while the deep optical trap gives rise to a small dimple. The magnetic trap potential is different for ^{85}Rb and ^{87}Rb atoms due to the slightly larger magnetic moment of ^{85}Rb ($\mu_{85} = \frac{2}{3}\mu_B$, $\mu_{87} = \frac{1}{2}\mu_B$) for the spin states we cool. While in Fig. 2.11 one might be able to tell that the ^{87}Rb trap is $\sqrt{3/4}$ times weaker, the most striking effect of the magnetic moment difference is on the equilibrium position of the broad confinement when including gravity. This difference in sag is given by

$$\Delta y_{\text{sag}} = \frac{g}{2B''}\left(\frac{m_{85}}{\mu_{85}} - \frac{m_{87}}{\mu_{87}}\right) \tag{2.10}$$

where B'' is the curvature of the total magnetic field. In the 10 Hz spherically symmetric trap $\Delta y_{\text{sag}} = 1.7$ mm, and this is a primary reason why sympathetic cooling all the way to quantum degeneracy is not feasible with this trap.

We choose the position of the optical trap potential to coincide with the center that of the

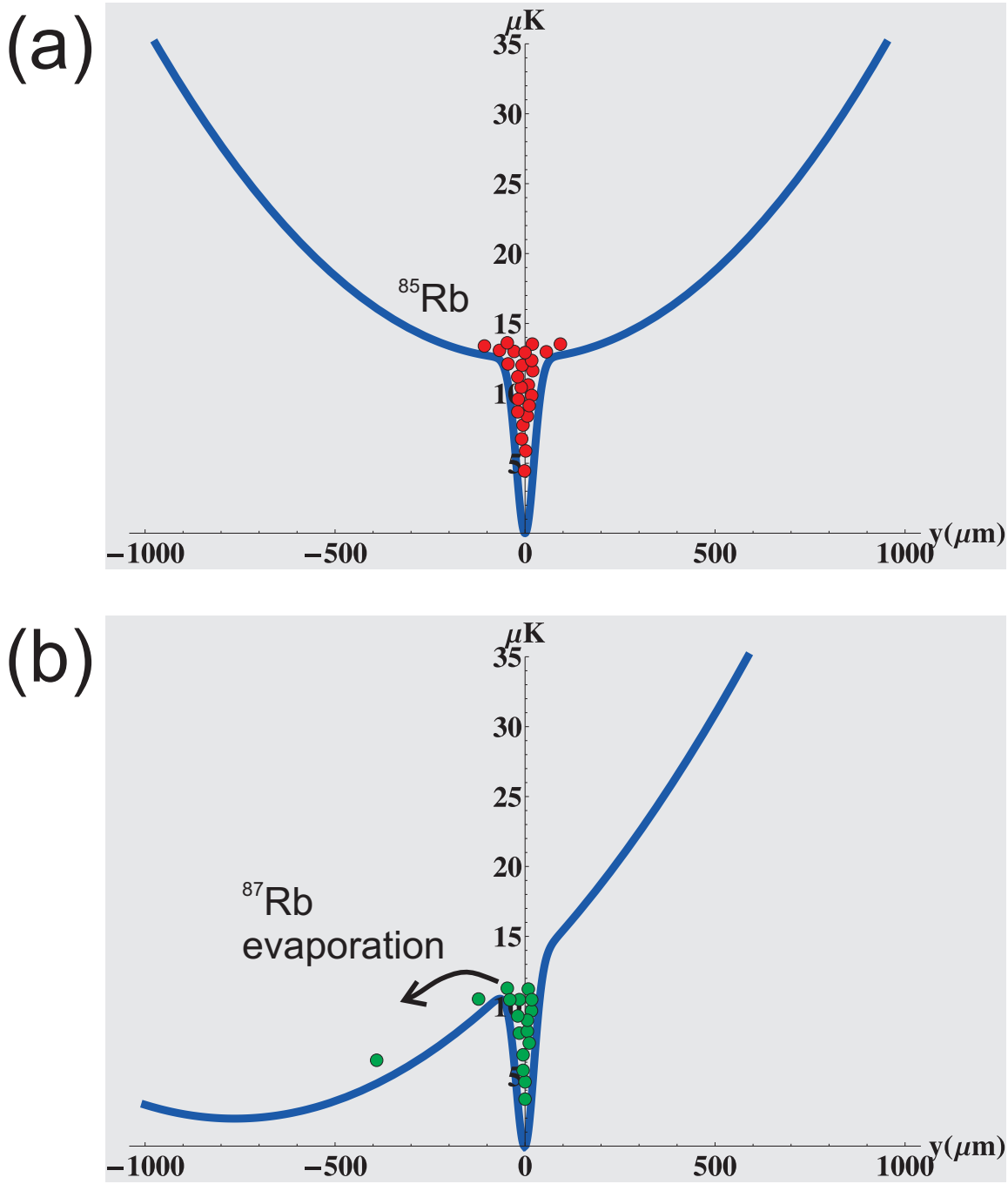

Figure 2.11: Modeled potentials during the hybrid trap evaporation for both ^{85}Rb (a) and ^{87}Rb (b). The vertical axis is potential energy, in units of μK, while the horizontal axis is the position in the vertical, y direction, in units of μm. The broad confinement is due to the magnetic trap, while the tight potential is due to the optical trap. During the hybrid trap evaporation the depth of the optical trap potential is lowered. For ^{85}Rb (a) the result is a trap frequency that is getting smaller and smaller as the optical trap potential is lowered. For ^{87}Rb the effect of lowering the optical potential is the same as how normal OT evaporation works, with the most energetic of the ^{87}Rb atoms spilling over the lip of the potential towards $-y$. These freshly evaporated atoms are later hit with an rf knife, resonant with the $|F = 1, m_F = -1\rangle$ to $|F = 1, m_F = 0\rangle$ transition, leaving the newly untrapped atoms free to fall under the force of gravity. With this hybrid trap evaporation, we are able to cool ^{85}Rb with minimal number loss, as ^{87}Rb is the species directly being evaporated.

broad trapping potential for ^{85}Rb atoms. At the start of the hybrid trap evaporation, there is no magnetic confinement at all, and the deep optical trap is the only potential the atoms know. This means that the ^{85}Rb and ^{87}Rb gases are well overlapped. When the magnetic trap is first ramped on, the optical potential is so deep that, for the most part, the atoms are oblivious.

Of course, we are not in the business of loading optical traps, but rather evaporating towards degeneracy. In the hybrid trap evaporation scheme, this is achieved in exactly the same way as with a conventional optical trapping scheme [61, 62], whereby we lower the laser intensity and hence lower the depth of the optical confinement. During this hybrid trap evaporation we also manipulate the magnetic field, setting it at 168.5 G to minimize ^{85}Rb losses, as was done similarly in Ref. [49] and Ref. [52]. For the ^{87}Rb gas, lowering the depth of the optical confinement has the desired effect of preferentially "spilling" out the most energetic of the atoms. The key to sympathetic cooling with the hybrid trap evaporation is that as the trap depth is lowered, ^{85}Rb atoms don't spill out but are instead loaded into the final, weak magnetic trap.

The energetic ^{87}Rb atoms actually "spill" into a conservative potential and will reach their turning point and eventually redeposit their energy back into the ensemble. Therefore, we zap them with rf, driving them to a state with zero magnetic moment, so that they fulfill their destiny of going splat on the bottom of our science chamber. In the last stages of the hybrid trap evaporation scheme, we change our bias field to a value that gives the soon-to-be condensate a positive, 100 a_0 scattering length. Eventually, the optical trap can no longer support ^{87}Rb and we lose all the ^{87}Rb atoms. At this point a significant ^{85}Rb BEC has been born.

2.4.3 A final cut: the ^{85}Rb rf knife

Once the last bits of the ^{87}Rb gas have been evaporated away, we are left with a cloud of ^{85}Rb atoms that has reached the onset of quantum degeneracy with a significant condensed fraction. However, this gas is still not fully in the 10 Hz spherical trap. What is left is to reduce the remaining optical potential until it is completely gone, that is, remove the last elements of the hybrid trap.

The transition from the hybrid confinement to a purely magnetic trap presents an interesting regime in terms of trapping potentials for our condensate. We have found that at this stage of the experiment, we must introduce a ^{85}Rb rf knife, otherwise the BEC that ^{87}Rb has so selflessly sacrificed itself for will not survive the transition to the 10 Hz trap. This seems counter-intuitive at first, considering that our ramping down of the optical trap potential is adiabatic. One would naively suspect the phase-space density would remain constant and hence, so would the condensate fraction. One mechanism for destroying the ^{85}Rb condensates could be heating from inelastic collisions, but these timescales are much longer than the time it takes to go from the last stage of the hybrid trap to our spherical trap. So what gives?

A similar phenomena was observed by the Ketterle group [63]. In a configuration very similar to ours (an optical trap overlapped with a much weaker magnetic trap) they were able to create BECs by increasing the optical potential until the trap depth was equal to the chemical potential. They then observed the reversible destruction and revival of the condensate as they lowered the optical potential and then increased it again. A very similar mechanism is at work in our system. In an experiment quite similar to the Ketterle group's, we see both the destruction of ^{85}Rb BEC and subsequent revival as we lower and raise the optical trap depth, shown in Fig. 2.12. Here, we have plotted the BEC number (vertical axis) for a decreasing optical trap depth (bottom and top axes) as we either move towards a purely magnetic confinement (black points) or eventually ramp up the optical trap depth to where we started (red points).

The easiest way to think about this phenomena is by going to the limit of two different traps that are in thermal equilibrium, with the number of atoms in the broad, magnetic trap greatly outnumbering the atoms in the deep optical potential. In this limit, the gas of atoms contained in the magnetic trap can be thought of as a thermal reservoir. As we lower and raise the optical potential, the overall temperature of sample is fixed by this reservoir temperature (T_R). The fact that this configuration can seemingly spontaneously create (and destroy) a condensate comes about because of the much higher critical temperature for the deep optical potential (T_c^{optical}), compared to that of the weak magnetic trap (T_c^{mag}) which has a higher trap frequency ($T_c \sim \omega_{ho}$). With the

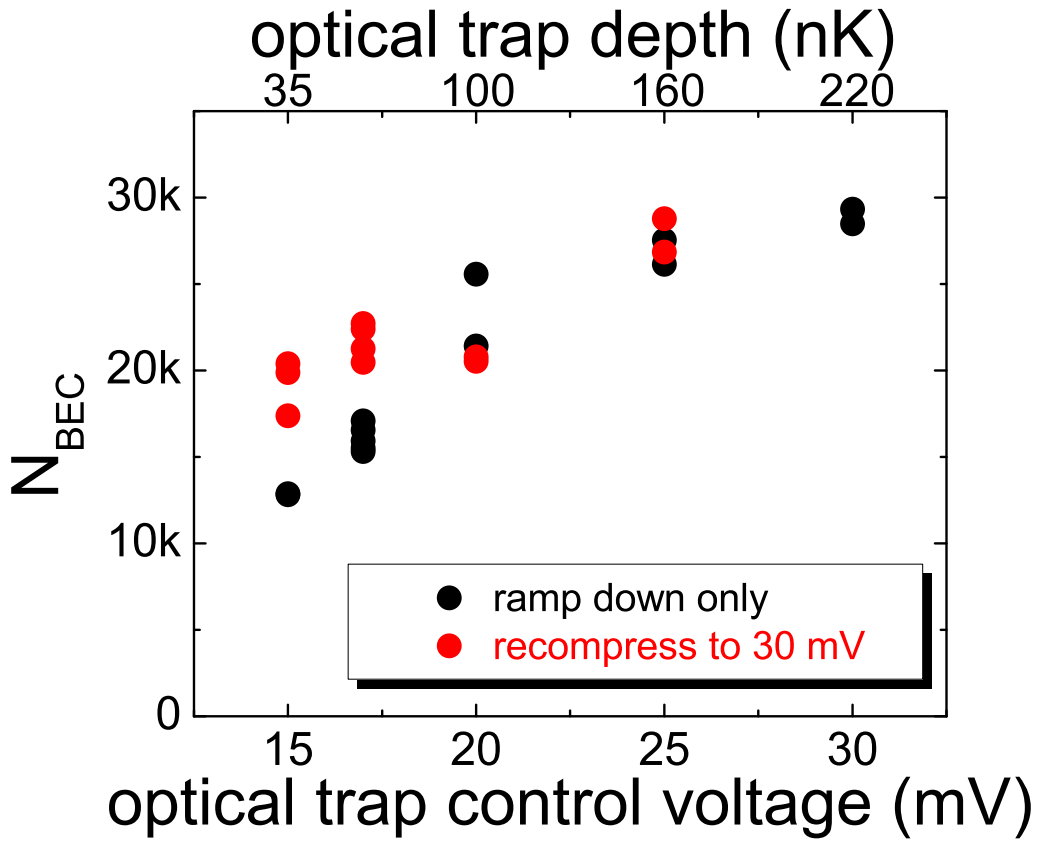

Figure 2.12: Evidence of the "^{85}Rb thermal reservoir" in the final transfer from the optical trap to the 10 Hz trap. Condensate number on the vertical axis is plotted versus the optical trap control voltage on the horizontal axis. The traps are modeled and the optical trap depth is then calculated from this model using the optical trap voltage. The optical trap power is given by $0.55\frac{\text{mW}}{\text{mV}}(V - 12\text{ mV})$. This optical trap depth is shown on the upper horizontal axis. The black points show the BEC being melted as the trap depth is lowered. We attribute this to ^{85}Rb atoms at a much smaller phase-space density (compared to those ^{85}Rb atoms in the optical dimple) with a significant population in the broader magnetic trap. The red points correspond to the measured BEC number when the optical trap depth is again lowered to the value shown on the x-axis, but then adiabatically ramped back to 220 nK (30 mV of control voltage). We see for these experiments that the BEC number has partially restored. This seemingly "reversible" process of BEC creation supports the proposed mechanism describing this process in the text. We attribute the fact that the BEC is not fully recovered by this process to inelastic collisions.

two systems in thermal equilibrium, all one needs for local condensation is for $T_c^{\text{optical}} > T_R$.

Another way of thinking about this is that while the two systems are in thermal equilibrium, the phase-space density is a local quantity. By lowering the potential of the optical trap, we are, in-effect, increasing the local phase-space density for those atoms due to a corresponding increase in density. This "adiabatic increase in phase-space density" was first put forth by Pinkse *et al.* [64].

To avoid melting our newborn condensate in going from the hybrid trap to the purely magnetic trap, we remove the most energetic ^{85}Rb atoms from the magnetic confinement with a ^{85}Rb rf knife. We apply this knife after the optical confinement can no longer support ^{87}Rb, roughly 2 s before the entire evaporation is over. We found that bringing the rf knife in closer to the trap bottom serves to fine tune the condensate number and fraction, as shown in Fig. 2.13. We keep the knife at a fixed frequency of roughly 120 kHz (6 μK) from the trap bottom to remove roughly 35,000 of the most energetic atoms. In understanding this unique evaporation, it is helpful to keep in mind that the $1/e^2$ waist of our focussed optical trap beam is roughly 50 μm, and the rf knife frequency corresponds to a position roughly 60 μm from the trap center. On a day-to-day basis this, along with the ^{85}Rb/^{87}Rb ratio controlled by the MOT fill, the final ^{85}Rb rf knife provides the experimenter with the two knobs needed to achieve large ^{85}Rb BECs from the hybrid trap evaporation.

2.4.4 How's it look? Imaging ^{85}Rb BEC

After it is all said and done, what we are left with is a ^{85}Rb BEC with zero measurable remnant ^{87}Rb to speak of. As presently constituted, however, our apparatus does not have the capability of absorption imaging ^{85}Rb atoms at high-magnetic field. This, in turn, means that we will have to play a couple tricks for imaging our condensates.

There are two issues to overcome when imaging the ^{85}Rb gas after expansion from the 10 Hz trap. The first is that with such a weak trap, the expansion time needed for the optical density (OD) to fall off to something reasonable (i.e. no saturation effects) for resonant absorption imaging

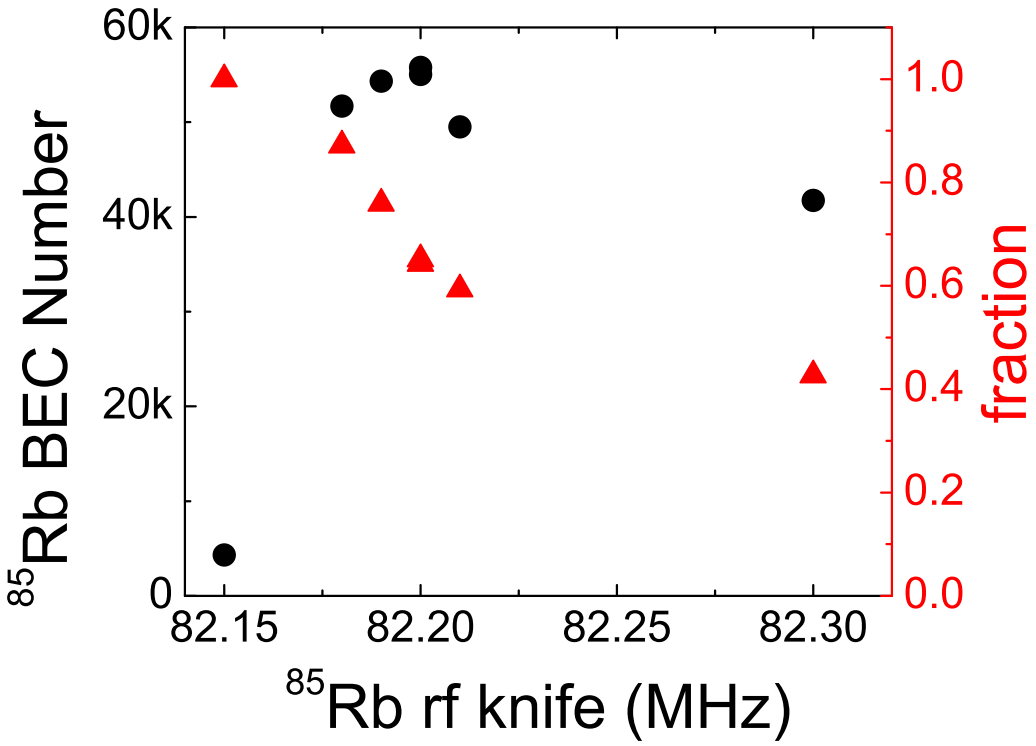

Figure 2.13: Final evaporation of the ^{85}Rb gas. The vertical axis on the left corresponds to the black circles, and gives the overall BEC number determined from a two-component Gaussian fit to the time-of-flight absorption image. The axis on the right-hand side corresponds to the red triangles, and gives the BEC fraction ($N_{\mathrm{BEC}}/N_{\mathrm{total}}$). The horizontal axis is the fixed frequency of the rf knife in question. The knife is on for 2 seconds of the evaporation and is the final tool we use for purifying our ^{85}Rb BEC.

is painfully long. In our science cell, we are limited to expansion times of about 30 ms before the BEC hits the cell wall that is 5 mm away. In order for our in-trap OD (~ 50) to fall off to something measurable, say 2, we would need to expand for at least 70 ms ($N_{\mathrm{BEC}} = \frac{2\pi}{5}(\frac{2\pi}{\lambda^2})\mathrm{OD}\ R^2$, where λ is the wavelength of the resonant light, and R the measured condensate radius [65]). For 30 ms of expansion, the BEC volume has increased by a factor of 8, but is still much too dense to image accurately. To work around this, we transfer a small fraction of the condensate into the upper, F=3 manifold via an inefficient adiabatic rapid passage (ARP). The small fraction transferred via the ARP is calibrated using a thermal gas (above T_c). The shot-to-shot fluctuation in the transfer efficiency is significantly smaller than the 10% shot-to-shot number fluctuation in our experiment.

The second imaging issue comes from the fact that ^{85}Rb has a large negative background scattering length of -450 a_0. Because we do not image at high-field, we must eventually hand over control of the scattering length to the background value at the moment of imaging. Condensates in the presence of a negative scattering length are unstable, and the attractive interactions induce a collapse [66]. This collapse leads to large, inelastic loss, which only leaves a thermal gas for the subsequent absorption images. For the large, relatively dense condensates we have in expansion, this attractive scattering length causes an implosion that leads to loss of atoms as well as loss of information in the time-of-flight image. This problem was solved previously in our experiment by leaving the magnetic field on during expansion, until the density had fallen off enough that collapse was no longer possible. In our 10 Hz confinement, however, the cloud does not possess the necessary kinetic energy to reach such a low-density regime in a reasonable amount of time. Therefore, in addition to leaving the magnetic field on during expansion, we also ramp the field to a value where the scattering length is roughly 500 a_0 right before turning off the trap confinement. This ramp in a gives the condensate extra energy in its expansion.

We model the expansion (and eventual implosion) of the BEC with the Pérez-Garcia model that was discussed in section 2.2.1. We choose a scattering length for the expansion that is well above what the model deems necessary, to avoid the possibility of local collapse due to fluctuations in the density that give rise to small regions of higher density. However, too high a scattering

length for the expansion ($a \sim 1000\ a_0$) can cause loss from three-body recombination, which we have observed as loss in our absorption images.

With an imaging scheme now in place for our ^{85}Rb condensates, we can take a step back and evaluate the performance of the hybrid trap evaporation. In Fig. 2.14, we show the number versus temperature for both ^{85}Rb and ^{87}Rb during the hybrid trap evaporation. Note that even though we do no direct cooling of ^{85}Rb, we still see loss. It is unclear where this loss comes from, but we speculate the cause is inelastic collisions, either ^{85}Rb-^{85}Rb collisions or, more likely, ^{85}Rb-^{87}Rb collisions. We also observe a discrepancy between the measured temperature of the ^{87}Rb gas and the ^{85}Rb gas near the end of the evaporation (corresponding to the coldest temperature in Fig. 2.14), even though both are thought to be in thermal equilibrium. We attribute this to the increased sag in the weaker optical trap potentials for ^{87}Rb. We describe the sag of ^{87}Rb in the optical trap as $y_{sag} = g'/\omega_\rho^2$, where ω_ρ is the radial trap frequency for ^{87}Rb due to the optical trap confinement and $g' = g/4$ is the downward acceleration experienced by ^{87}Rb at the optical trap position, were there no optical confinement. We remind the reader that the optical trap position has been chosen to correspond to the equilibrium position of ^{85}Rb in the purely 10 Hz spherical trap, while the equilibrium position of ^{87}Rb in the same trap is displaced $\frac{1}{3}g/(2\pi \times 10\ \text{Hz})^2$ from that of ^{85}Rb, due to ^{87}Rb's weaker magnetic moment. The magnetic confinement effectively weakens gravity for ^{87}Rb (reflected in g') while canceling out the force of gravity for ^{85}Rb. The fact that ^{87}Rb incurs sag effectively makes the ^{87}Rb trap frequencies smaller than those of ^{85}Rb.[1] The trap frequencies used to calculate the temperature of ^{87}Rb are those for ^{85}Rb, which we know experiences zero sag, by design.

An interesting comparison between the hybrid trap evaporation and our previous optical trap evaporation is in the relative number of ^{85}Rb to ^{87}Rb. Where as in the old evaporation, we began with roughly twice as much ^{85}Rb than ^{87}Rb, we are now operating on the other side of things,

[1] The parabolic confinement from an optical trap is an approximation valid at the center of the laser beam, which is described with a gaussian profile. We have modeled this beam profile and found that as one moves away from the center of the beam the parabolic approximation is no longer valid, and the confining potential looks effectively "weaker" to the trapped atoms, making for smaller trap frequencies.

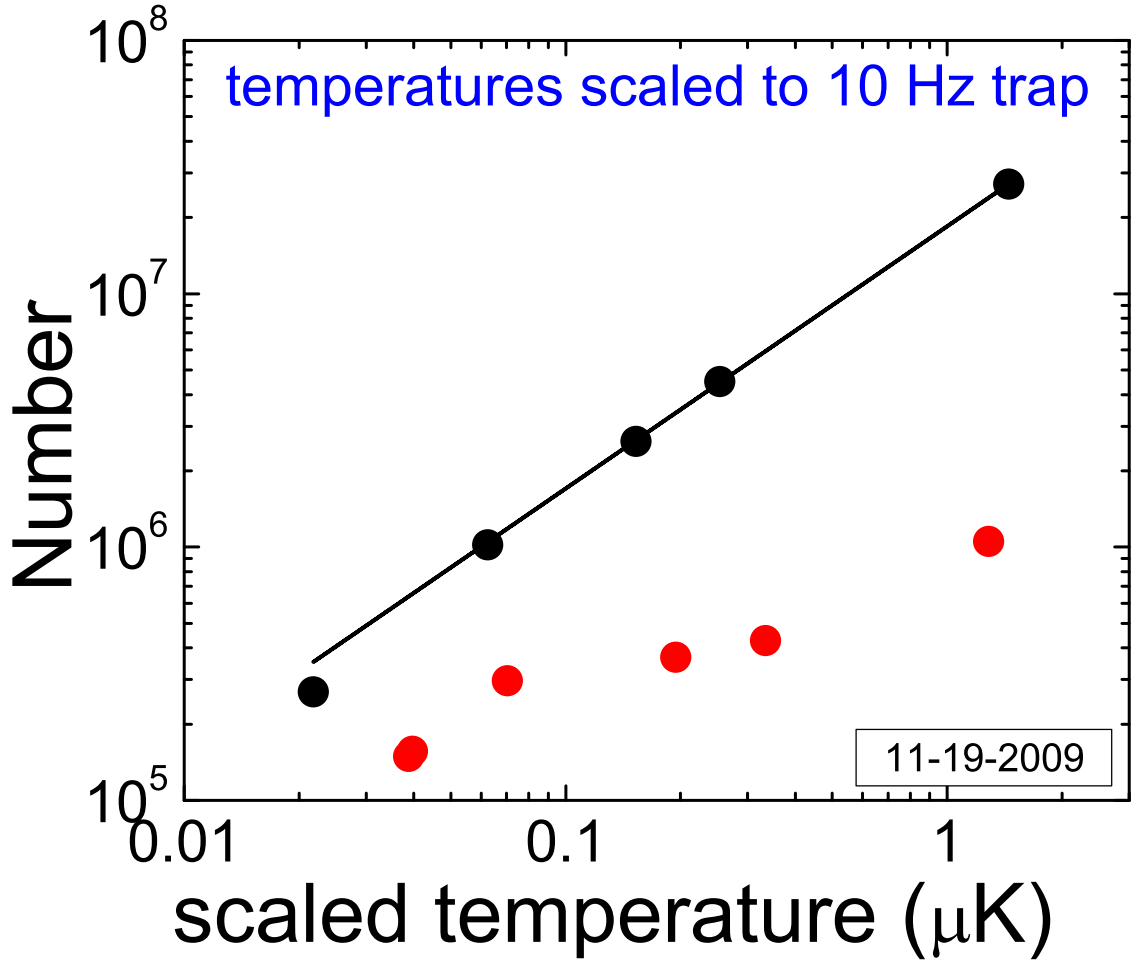

Figure 2.14: Evaporation trajectory for both ^{87}Rb (black) and ^{85}Rb (red). On the vertical axis we have the number of atoms at different points in the hybrid trap evaporation. All the data here is above the onset of condensation. The horizontal axis is the temperature of the clouds measured using time-of-flight expansion. These temperatures have been scaled ($T_{\rm scaled} = T_\rho(2\pi \times 10\ {\rm Hz}/\omega_\rho)^{2/3}$) to a 10 Hz trap, assuming an adiabatic transfer, so that we can, compare the phase-space density at different stages of the evaporation. The points here are taken at the same stages of evaporation, with the ^{85}Rb and ^{87}Rb clouds in thermal equilibrium. We attribute the disagreement between the temperatures of ^{85}Rb and ^{87}Rb to the increased sag distorting the optical potential, as described in the text. The ^{85}Rb number loss is minimal for this type of evaporation, reflecting only the inelastic losses to which we are defenseless, as no direct evaporation is done on ^{85}Rb during this stage of cooling (see Fig. 2.8). The efficiency of the evaporation is determined by a fit of the ^{87}Rb data to $N = \alpha T^\beta$, which gives an efficiency of $\beta = 1.04$ for this evaporation.

beginning our evaporation with roughly 30 times more ^{87}Rb than ^{85}Rb. This, I believe, more than anything illustrates the difference between the old way of simultaneous cooling in the all optical potential, and our new way of cooling in the hybrid geometry.

2.4.5 Shaving off the slosh

With the production of ^{85}Rb BEC now under control, we focus our attention to its stability in terms of center-of-mass oscillations, or slosh. Slosh is particularly damaging to the hybrid trap evaporation because there is relative slosh between ^{85}Rb and ^{87}Rb, owing to the different trap frequencies for ^{87}Rb and ^{85}Rb when confined magnetically. This is a problem for the sympathetic cooling of ^{85}Rb with ^{87}Rb, as the atom clouds will spend less time thermally overlapped when they experience different frequency slosh versus when they are both at equilibrium at the center of the trap. The most effective way to minimize slosh is with a careful alignment of the 10 Hz trap onto the optical trap. While this step is our primary method for staving off slosh in the radial direction, axially ($\hat{z}$) slosh direction is trickier to suppress since it largely comes from the initial load into the OT from the MT. In other words, it is here from the beginning and here to stay.

What we have found is that the proximity of the ^{87}Rb rf knife to the trap bottom during the earlier stages of the hybrid trap evaporation can have a positive effect on the axial slosh. We show the effect of the ^{87}Rb rf knife frequency (horizontal axis) on the gas in Fig. 2.15. In Fig. 2.15(a) we see the danger of bringing in the knife too close, as it effectively destroys our ^{87}Rb coolant and leaves us with hot ^{85}Rb clouds. In Fig. 2.15(b) the beneficial effect (the amplitude of the center-of-mass oscillations) of the rf knife is also shown. We take advantage of this effect by leaving the knife 200 kHz detuned from the trap bottom. Reduction of slosh is also beneficial to the performance of the hybrid trap evaporation.

2.4.6 The barber's take

So, after all is said and done, having developed this cooling scheme, we are in a unique position to analyze the pros and cons. All in all, after the magnetic trap was designed and working well,

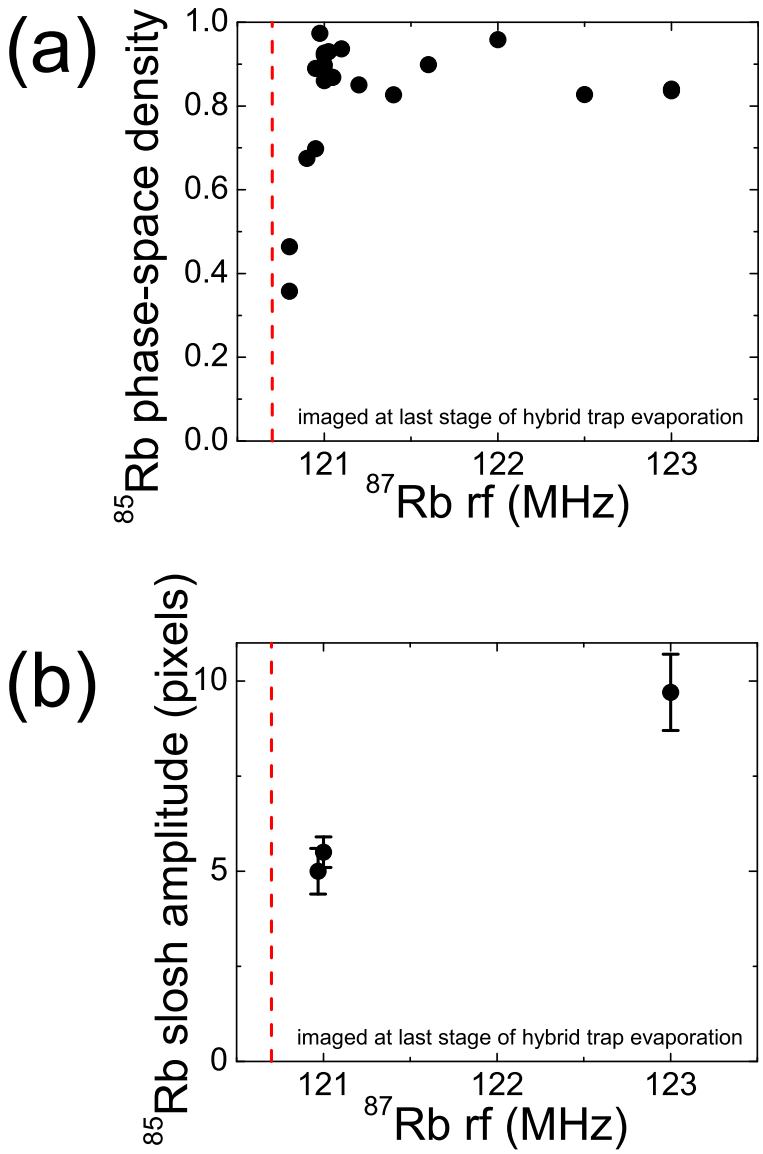

Figure 2.15: Effects of the ^{87}Rb rf knife applied during the hybrid trap evaporation on the final ^{85}Rb phase-space density (a) and slosh of the ^{85}Rb cloud (b). The horizontal axis for both plots corresponds to the frequency of the ^{87}Rb knife being applied. The resonant frequency at the bottom of the trap is depicted by the red dashed vertical line. In (a) we see how cutting too close to the trap bottom has a detrimental effect on ^{85}Rb evaporation performance, as seen by the low PSD at the smallest rf detunings. Here, we presume that the ^{87}Rb is not effectively evaporating, with the knife cutting farther and farther into the cloud than would be ideal. In (b), however, we see how there is a benefit to bringing the ^{87}Rb knife in close to the trap bottom, as the amplitude of the ^{85}Rb slosh (vertical axis) has been reduced as a result of the closer knife. We attribute the reduced ^{85}Rb cloud's slosh to the reduced slosh of the ^{87}Rb cloud (the ^{87}Rb knife essentially damping the oscillations) who effects the ^{85}Rb cloud through collisions. This slosh data was taken on clouds whose rms size was 22 pixels, corresponding to a temperature of 130 nK. Through a similar set of experiments we have seen that a knife that is 200 kHz (10 μK) or 130 μm away from the hybrid trap center presents the best compromise in terms of minimizing the axial slosh, while still leaving enough ^{87}Rb in the trap to adequately perform its role in the hybrid trap evaporation.

it took two months, from inception of the hybrid trap evaporation scheme to production of ^{85}Rb BECs. I think that for *any* graduate student, that would be, fractionally speaking, a fairly quick turn-around. Our scheme routinely produces ^{85}Rb condensates of 40,000 atoms, with condensates of 90,000 atoms on the best of days[2] . More importantly, however, these condensates are in a weak, 10 Hz spherical trap that is ideal for the study of strongly interacting BEC physics, which is the goal of this lab.

The major issue with this evaporation is that it relies heavily on the alignment between the 10 Hz trap and the optical potential. This alignment is presently a painstaking process that usually eats up the better part of a work day in the lab. It is also one that must be revisited every few weeks or so, as the traps will tend to drift out of alignment. When the traps are misaligned the creation of ^{85}Rb BEC is nearly impossible, with the ^{87}Rb and ^{85}Rb having different modes of oscillations, making for poor thermal overlap. Also, as mentioned before, with more degrees of freedom comes more opportunity for things to go wrong. This seems like an unavoidable trade-off in experimental physics, however, as we will always be pushing towards more complicated experiments.

The particular cooling scheme laid out here requires the species being cooled to be magnetically trappable. However, this idea could be extended to species that were not magnetically trappable, as the only criteria one really needs is to apply a magnetic field gradient that cancels out the effects of gravity of the species of interest and a "coolant" species that has a different magnetic moment. I believe this scheme could be quite promising for species that are difficult to cool on their own because of inelastic collisions. Here, minimizing the absolute number of this species is favorable, which the sympathetic cooling in the hybrid trap provides. Another benefit of this cooling scheme is that one can ensure that there is no coolant species, ^{87}Rb in our case, left at the end of the evaporation. This is important for experiments where the interactions between the coolant and the science species are non-negligible.

[2] Check it! File number 138, May 6th, 2010.

Chapter 3

Bragg spectroscopy

Having designed and implemented a trap with our scientific goals of studying strongly interacting BECs in mind, we now can look past the system of interest and begin to consider the relevant probes. One such probe, Bragg spectroscopy, looks tailor-made for studies at large na^3, as it is quick probe relative to three-body loss and breathing timescales that can complicate the signal. We will present data showing the success we have had with Bragg spectroscopy investigating condensates at large na^3. In addition, the concepts of Bragg spectroscopy will be laid out, which is relevant for the next chapter's discussion of a photon-counting technique for Bragg spectroscopy.

I will present this chapter in three parts, beginning by telling the reader first about *what* Bragg spectroscopy probes: the dispersion relation of a BEC. This will serve to motivate both this chapter and the next. I will then present the theoretical underpinnings of *how* Bragg spectroscopy works by giving two equivalent pictures of the Bragg process. Finally, I will give the pertinent experimental considerations in measuring a Bragg response. This chapter will both lay the ground work of the next chapter, as well as provide motivation for measuring the Bragg response in a new way.

3.1 Measuring the dispersion relation of an interacting BEC

Bragg spectroscopy offers the experimenter a means to measure the dispersion relation, which is defined as the energy-momentum relationship for excitations, of a BEC. In measuring the dispersion of a condensate, we probe fundamental excitations of the system. Many of these excitations

play a role in the macroscopic observations discussed in Chapter 1.

To measure the dispersion relation with Bragg spectroscopy, we drive an excitation with momentum $\hbar k$ with two coherent lasers, referred to as the Bragg beams. In Fig. 3.1(a) we show the BEC response measured in a time-of-flight (ToF) image, where the horizontal and vertical axes correspond to momentum space. Because of the condensate's small momentum spread, the excitations appear as a distinct atom cloud whose position corresponds to $+\hbar k$ momentum on the horizontal axis. We determine the response of the system by counting the number of atoms at $\hbar k$ excitations (N_{+k}) in the ToF image. We can later normalize N_{+k} to the total number of atoms to determine the fraction of atoms excited.

We determine the energy for resonant excitations spectroscopically. That is, we vary the frequency difference of the Bragg beams, and measure the corresponding response of the system, while keeping k constant. Note that by changing the frequency difference between the two Bragg beams we can create and measure momentum excitations in either the $+k$, as well as the $-k$ direction. In Fig. 3.1(b) we show data for a typical Bragg spectrum, plotted as the response versus the probe frequency. The response is given in terms of the transferred number fraction, which is defined as the net response of the system, $(N_{+k} - N_{-k})/N_{\text{total}}$. For example, a transferred number fraction of 100% (-100%) would correspond to a ToF image where the entirety of the cloud is at the $+k$ ($-k$) position.

We typically fit the data shown in Fig. 3.1(b) to a two-gaussian function of the form $A(e^{-(\omega-\omega_0)^2/2\sigma^2} - e^{-(\omega+\omega_0)^2/2\sigma^2})$. A fit to this form is drawn as a black line in the Figure 3.1(b). The peak Bragg response is characterized by the fit parameter A. The resonant frequency of the k excitation is given by ω_0, while σ describes the rms width of the Bragg lineshape.

To map out the dispersion relation, we could measure the resonant frequency, ω_0, of excitations at different k. We plot in Fig. 3.1(c) what such a dispersion relation would look like for both a free particle (black line) as well as for a weakly interacting BEC (red line). Bogoliubov predicted

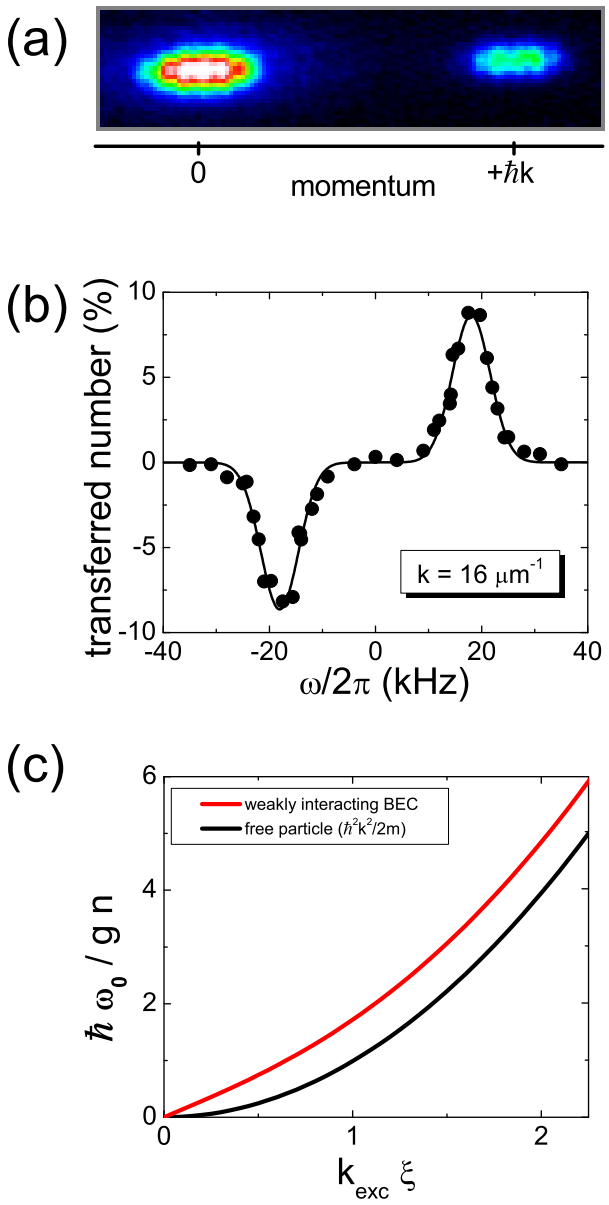

Figure 3.1: Three pictures of Bragg spectroscopy. (a) Time-of-flight (ToF) absorption image taken to measure Bragg excitation. The response is measured by counting the number of atoms (N_{+k}) in the small cloud at position $+\hbar k$. Excitations at $-\hbar k$ measured similarly. (b) An example Bragg spectrum at fixed k for ^{85}Rb at $a = 100a_0$. Transferred number is given by $(N_{+k} - N_{-k})/N_{\text{total}}$. The detuning between the Bragg beams, ω, is shown on the horizontal axis. We fit the data to a lineshape whose functional form is described in the text. Lineshapes are modeled as two gaussian functions, centered at $\pm\omega_0$. The Bragg resonance, ω_0, is determined from the center frequency of the lineshapes, as determined by the fit. (c) Dispersion relation, as could be measured through Bragg spectroscopy at different k. On the horizontal axis is the momentum of the excitation, in units of the inverse healing length, ξ^{-1}. On the vertical axis is the excitation energy, normalized to the interaction energy. Notice that for the case of a weakly interacting condensate (red line) there are two regimes, $k\xi < 1$ and $k\xi > 1$, where the dispersion goes as k (phonon regime) or k^2 (single-particle regime), respectively. In the phonon regime, the slope of the dispersion curve corresponds to the speed of sound in a condensate. The black line is the solution for a free particle, given by $\hbar\omega_0 = \hbar^2k^2/2m$. Note that far into the single-particle regime the excitation energy for the weakly interacting condensate differs from the free particle case (black line) by gn. Thus Bragg spectroscopy at large k can be used to determine the interaction energy of a condensate.

the dispersion of a weakly interacting condensate, which we can write as [24]

$$\hbar^2\omega_0^2 = (\hbar^2k^2/2m)(\hbar^2k^2/2m + 2gn). \tag{3.1}$$

We consider this well-understood case of weakly interacting BEC as a platform upon which to build understanding of the strongly interacting case that interests us. As laid out in Ch. 1, and seen in Fig. 3.1(c), there are two distinct regimes for excitations, delineated by the product of $k\xi = 1$ (where $\xi = \hbar/\sqrt{2mgn} = 1/\sqrt{8\pi na}$ is the healing length). We will separately discuss the dispersion relation of a BEC in these two regimes of $k\xi > 1$ and $k\xi < 1$ in the following sections.

3.1.1 Single-particle excitations

Single-particle, high momentum ($k\xi > 1$) excitations in a Bose-Einstein condensate are, for me, the most straight-forward and intuitive to understand. The energy of these excitations have a familiar, quadratic dependence on momentum that goes as $\hbar^2k^2/2m + gn$. This is quite similar to that of a free particle, like a baseball, whose energy goes as $\hbar^2k^2/2m$ (see black line in Fig. 3.1). The fact that we are not performing Bragg spectroscopy on baseballs, but rather interacting BECs modifies things slightly, but the quadratic nature of the excitation is still present.[1]

One can understand how two-body interactions between the atoms in the condensate modify the dispersion of high-k excitations by considering the energy of the system. To create an excitation at high momentum, we are effectively removing an atom from the condensate ($-\mu_{\mathrm{BEC}}$) and adding an excitation at high momentum ($+\hbar^2k^2/2m + 2gn$), where the high momentum excitation has both a kinetic energy ($+\hbar^2k^2/2m$) and an interaction energy ($2gn$) to be taken into account. In light of this, we modify the free particle dispersion

$$\lim_{k\xi\gg 1} \hbar\omega_0 = \frac{\hbar^2k^2}{2m} + 2gn - \mu_{\mathrm{BEC}} \tag{3.2}$$

As discussed in Ch. 2, the chemical potential for interacting condensates comes about because of the interactions between the atoms, and $\mu_{\mathrm{BEC}} = gn$. For the excited particles, with momentum

[1] For review on the energetics of baseballs and softballs, I refer the reader to the annual DAMOP breakout session: Working Group on Trajectories.

$\hbar k$, there are equal direct and exchange contributions to the interaction energy between the high momentum particles and atoms in the BEC. This leaves us with an interaction energy of $2gn$. This gives a dispersion for Bragg spectroscopy in agreement with Bogoliubov's prediction in the high momentum limit

$$\lim_{k\xi \gg 1} \hbar\omega_0 = \frac{\hbar^2 k^2}{2m} + gn \tag{3.3}$$

This difference between the free particle dispersion and that of an interacting condensate is reflected in the constant offset at high momentum between the black and red line in Fig. 3.1(c). Because this offset, or line shift, is exactly the interaction energy, gn, Bragg spectroscopy at large $k\xi$ offers a direct probe of the interaction energy. This interaction energy, while well-understood for a weakly interacting BEC, presents to us one of the "carrots" we have been trying to catch for the strongly interacting case where the LHY term (Eq. 1.3) is expected to modify this interaction energy.

3.1.2 Collective phonon excitations

The subject of phonons in a BEC is rich enough that a graduate student could devote an entire career to their study. What I present here will only be a few useful pictures in understanding the physics of phonons and how they relate to Bragg spectroscopy. I refer the reader to Dr. Tung's thesis [67] for a more thorough discussion.

In Fig. 3.1(c), the high momentum, single-particle excitations that are quadratic in k give way to excitations that depend linearly on k at low momentum, where the excitation energy goes as

$$\lim_{k\xi \ll 1} \hbar\omega_0 = \hbar\sqrt{\frac{gn}{m}}k \tag{3.4}$$

The crossover to collective, phonon excitations occurs when the wavevector of the excitation is equal to one over the healing length, $k = \xi^{-1}$. The healing length is of fundamental importance to the physics of interacting Bose-Einstein condensates and it can be thought of as the minimum distance over which the BEC wavefunction (or density) can vary significantly. In the condensed matter community, ξ is referred to as the coherence length.[2] As an example, we consider a box

[2] In atomic physics, the term coherence length has been taken to describe our lasers. As prudent researchers, we

potential where the density of a BEC would be uniform until it reached the edges of the box, where the density must drop to zero. The healing length is the distance in space that the density takes to go from zero to its uniform value. This fundamental length scale, where the quantum pressure ($\hbar^2/2m\xi^2$) balances out the interaction energy (gn), manifests itself in such phenomena as the minimum size of a vortex core.

Phonons, on the other hand, can be thought of as a manifestation of the interactions in a Bose-Einstein condensate, since phonon modes only exist for $k\xi < 1$. For a condensate to support phonon modes, the interaction energy, gn, must be finite. Phonons also reflect the BEC interactions in the speed at which they propagate, $c_{\mathrm{BEC}} = \sqrt{gn/m}$. This is the speed of sound in a BEC. This intimate relationship between interactions and phonon excitations motivates their study in the strongly BECs we aim to probe.

We understand the collective nature of phonons through experiments done by Vogels *et al.* [68], which verified the quasiparticle basis of phonons predicted by Bogoliubov [24]. In these experiments, they were able to both create a phonon excitation through low momentum Bragg spectroscopy, and then probe this momentum class using a second Bragg probe at high momentum, as suggested by Brunello *et al.* [69]. The experimenters demonstrated the collective nature of a phonon excitation by first creating N_{ph} phonon excitations in the $+k$ direction and then probing them to find that they were composed of $N_{\mathrm{ph}}u_k^2$ excitations in the $+k$ direction and $N_{\mathrm{ph}}v_k^2$ excitations in the $-k$ direction. Furthermore, they confirmed that these quasiparticle amplitudes (u_k^2 and v_k^2) agreed with Bogoliubov's predictions in the phonon regime of excitations $u_k^2 - v_k^2 = 1$ and $u_k^2 \approx 1/2k\xi > 1$.

For Bragg spectroscopy, excitations in the phonon regime are typically measured in the same way as their free-particle cousins, using ToF imaging. The quasi-particles described above are projected onto corresponding single-particle excitations by turning off the trapping potential [70]. This projection is understood by considering that the cloud expands once the trapping potential is gone, and therefore with the density (and hence the interactions) rapidly decreases. As we know,

know better than to offend our lasers.

a non-interacting condensate can only support single-particle excitations. This fact explains the transfer of phonon-excitations to single-particle excitations.

However, resolving these low momentum excitations in a ToF image is not easy. Practically speaking, the excitations corresponding to phonons will never cleanly escape the radius of the cloud, which is set by the interaction energy. This is easy to see if one considers that phonon energies are almost by definition less than the chemical potential of the condensate. Otherwise, phonons would have enough energy to "pop out" of the condensate and be distinguishable, single-particle excitations. This makes the resultant image analysis much more difficult [70, 27].

3.1.3 Dispersion at large na^3 and the roton

To take inventory, there exists a fully understood dispersion relation for a weakly interacting BEC, which has been experimentally verified [27, 70]. There also exists a measured dispersion relation in superfluid He, with a few theoretical underpinnings, which was presented in Ch. 1. Our stated experimental challenge is to connect these two wildly different regimes.

We show in Fig. 3.2 the first Bragg experiments accessing the strongly interacting regime. This part of my thesis work, which I will refer to as the 2008 Bragg experiments, was published in Ref. [54]. While we were enthusiastic about our results, and the departure from the mean-field physics depicted in red, we ran into unexpected complications in the data's interpretation. For one, although we were at a fixed momentum transfer of 16 μm^{-1}, our data begins in the single-particle regime ($k\xi = 4$ at $a = 150\ a_0$) and ends up in the crossover between the single-particle and the phonon regime ($k\xi = 2$ at $a = 900\ a_0$). Another hurdle to overcome in the interpretation of the data was a momentum-dependent scattering length as our largest values of a meant that $ka = 0.8$, which modifies the scattering amplitude from the usual low energy limit. These two effects are taken into account in the red theory line in Fig. 3.2, as described in the caption. Preliminary versions of data similar to this were presented in [49], with a brief discussion on some of the other theoretical treatments used to analyze the data.

In the end, this data suggested the existence of beyond-mean-field physics, as our data clearly

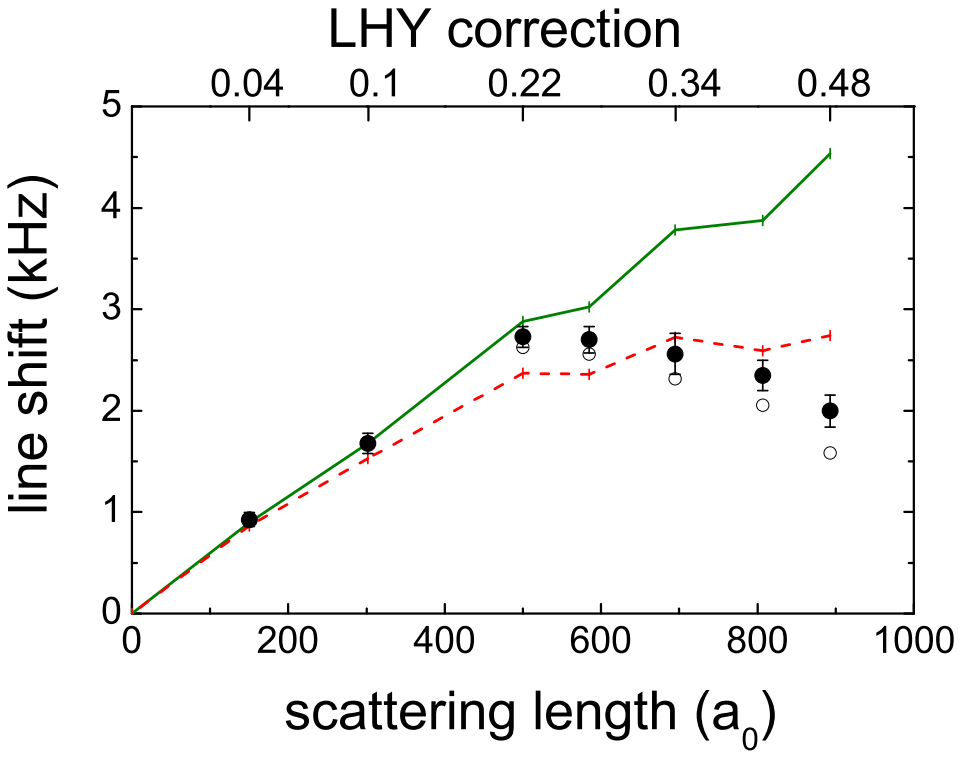

Figure 3.2: First Bragg experiments exploring the strongly interacting regime of dilute gas BECs. Vertical axis corresponds to the line shift: the offset between the measured Bragg resonance and the calculated free-particle result. In the single-particle regime, this would exactly correspond to the interaction energy gn. Horizontal axis represents the scattering length (lower axis) as well as the LHY correction to the energy $\frac{32}{3\pi\sqrt{8}}\sqrt{8\pi na^3}$ (upper axis). White circles correspond to the raw data, and black circles are the same data with an empirical correction for the thermal contribution. Green theory line is simply gn. Red theory line gives a result predicted by Beliaev [71] for a weakly interacting gas as the excitations go from the single-particle regime to the phonon regime (remember $k\xi$ is not held constant as a is changing), with a momentum-dependent scattering amplitude (ka is not small). To our knowledge there exists no theoretical treatment where a finite ka, $1/k\xi$ and $\sqrt{na^3}$ is taken into account, illustrating the theoretical complexity in interpreting these initial Bragg results.

disagrees with the theoretical prediction. However, Bragg data taken in this regime, at present, offers no way to *test* some of these theories, such as the LHY correction, due to the complications mentioned above. This will prove to be a driving motivation to go to lower-momentum transfer, which we will focus on in the next chapter.

To illustrate the regimes of excitations that have been studied to date, we chart the "experimental phase-space" that has been so far been mapped out in Fig. 3.3, where we plot na^3 versus $k\xi$. We use this plot to both understand the regimes that have been studied in interacting BECs, as well as the territory still uncharted in this many-body map. Depicted in black are the studies of weakly interacting BEC, while in blue we represent the neutron and X-ray scattering experiments performed on He II. In magenta, we have our 2008 Bragg spectroscopy experiments, which represent our first efforts to connect the weakly interacting BEC to the strongly interacting world of superfluid He [54].

A thesis on the study of strongly interacting BECs would be remiss without some discussion of the roton, which occurs in the regime of $k\xi$ and na^3 that is depicted by a hollow circle in Fig. 3.3. The roton corresponds to an anomalous local minimum in the dispersion relation of He II that occurs near $k\xi = 1$. One might speculate that a similar phenomena might be observed in the dispersion relation of an atomic BEC at large na^3. Richard Feynman presented his take on a roton with his "smoke ring" interpretation [72]. This was really just a modification to his proposal of a roton excitation consisting of a density current, where he now included some backflow, which both conserved current and was thought to better agree with the experimental data [73]. Feynman argues that the roton excitation's lower energy is a consequence of its wavelength, k^{-1}, being equal to the interparticle spacing. He postulated that density variations would be easier to arrange at this characteristic wavelength compared to other wavelengths, and that this would be reflected in a lower energy needed to excite them.

One of the motivations of this work is to further explore the experimental phase-space shown in Fig. 3.3 and probe some of the rich, many-body physics that has not been studied in an atomic Bose system. We hope that with such studies we can get a clearer understanding of the beyond

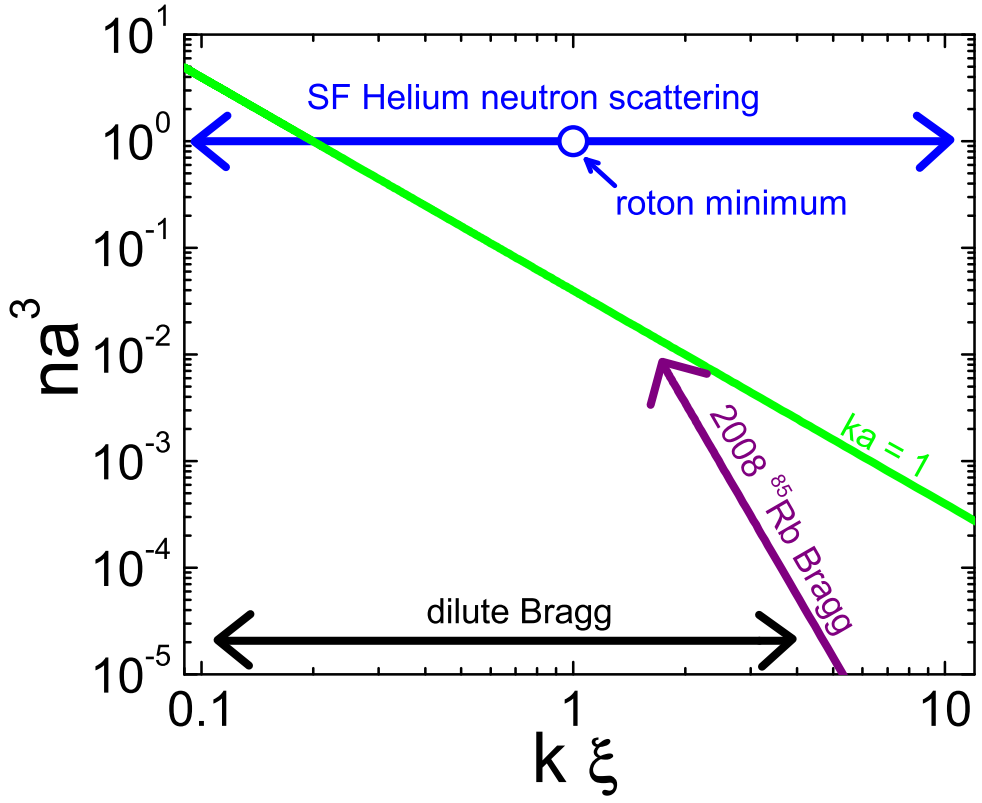

Figure 3.3: Charting the "experimental phase space", or regimes, where the dispersion relation has been experimentally tested for interacting BECs. On the vertical axis is the diluteness parameter, na^3. On the horizontal axis is the excitation wavevector, normalized to the healing length, $k\xi$. The black line illustrates the experiments that have been done with dilute gas BEC's, such as in Ref. [27]. The magenta line corresponds to the experiments performed in our lab in 2008 [54]. We plot in blue the regimes covered by studying the strongly interacting BEC that motivates us, superfluid liquid He, with the roton minimum depicted by the hollow circle. We also highlight in green another interesting competition of length scales, by plotting $k = a^{-1}$. This proved to be an additional complication to the experiments of 2008 and illustrates another interesting regime in this map of different regimes for the many-body physics of bosons.

mean-field physics that dominates these systems, and perhaps even knock on the door of the elusive roton.

3.2 Two pictures of Bragg spectroscopy

In Bragg spectroscopy, we probe the sample with two incident laser beams, and through the beams' collective effort a k momentum excitation is produced when the difference frequency between the two beams, ω, is equal to the excitation resonance frequency, ω_0. One of the most beautiful insights of quantum mechanics is the concept of wave-particle duality: two independent ways of looking at something, each never telling the full story by themselves, but when taken together reveal the true nature of the physics. Here, we also have two different ways to look at this Bragg process. These are both *equivalent*, and *complete* descriptions in and of themselves. We present both of these concepts to give the reader a deeper insight into Bragg. Each picture has its own merits and, when taken together, reveal the true story of Bragg spectroscopy.

3.2.1 A moving grating

Bragg spectroscopy owes its name to analogous experiments referred to as Bragg scattering. In these experiments a crystal medium is probed with incident X-rays. At particular incidence angles ϕ, constructive interference occurs and an X-ray diffraction pattern is seen at the corresponding reflectance angle ϕ. This diffraction pattern is intimately related to the lattice spacing of the crystal, with constructive interference established by Bragg's law

$$2d\sin(\phi) = i\lambda \tag{3.5}$$

where d is the lattice spacing, ϕ the angle of incidence and reflection, i an integer and λ the wavelength of the incident light.

In Bragg spectroscopy, the crystalline lattice structure has been replaced by an optical lattice created by the interference of two laser beams (referred to as beam 1 and beam 2). We write the

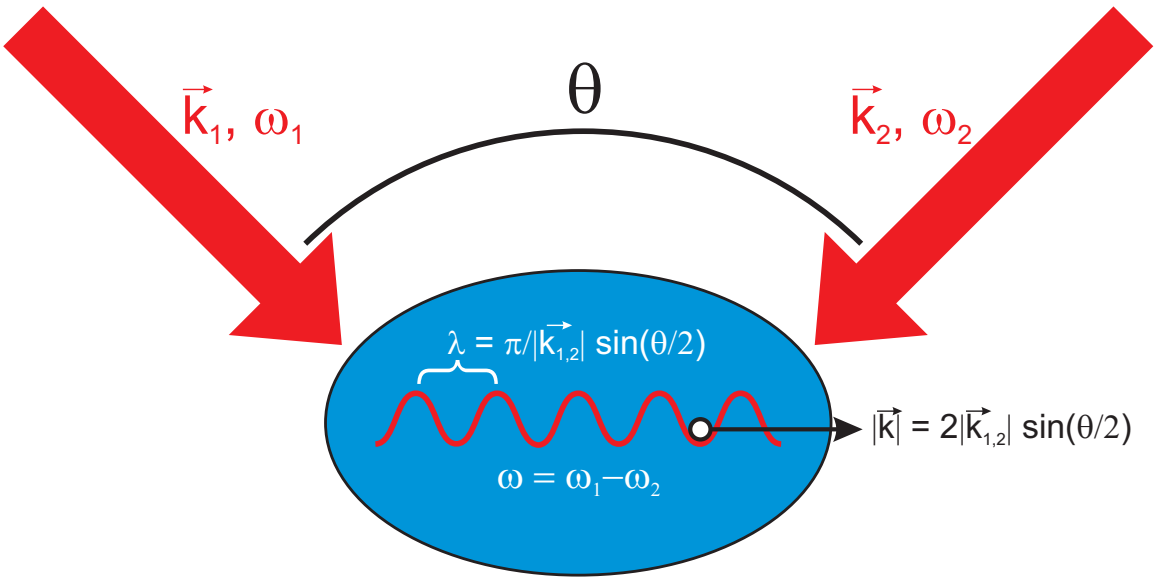

Figure 3.4: Moving grating picture for Bragg spectroscopy. The two coherent laser beams create an interference pattern in the condensate, shown as the periodic lattice in red. Because the beams are at different frequencies this optical lattice travels through the condensate with some velocity, $c = \frac{\omega}{|k|}$, and transfers momentum $\hbar k = 2\hbar k_{1,2} \sin(\theta/2)$ to the excitations. This picture is useful in considering the magnitude of the momentum transfer, Doppler shifts, as well as the competing lengthscales involved (e.g. ξ vs k^{-1}).

electric field produced by beam 1 (similarly for beam 2) as

$$\vec{E}_1(\vec{r},t) = \frac{E_0}{2}\left(\cos(\vec{k}_1\cdot\vec{r}-\omega_1 t)\right)\frac{\vec{k}_1}{k_1} \tag{3.6}$$

where $\vec{k}_1$ is the wavevector and ω_1 the optical frequency of beam 1. We write the magnitude of $\vec{k}_1$, the wavenumber, as k_1. For simplicity, we will set the phase of both fields equal to zero and assume that the amplitude of the electric field, $\frac{E_0}{2}$, is the same for both beams. The atoms experience a potential due to the AC Stark shift, which can be expressed as

$$U(\vec{r},t) = -\frac{1}{2}\alpha\left(\vec{E}_1(\vec{r},t)+\vec{E}_2(\vec{r},t)\right)^2 \tag{3.7}$$

where α is the AC polarizability of the atom at laser frequency ω [33]. We explicitly write Eq. 3.7 as

$$U(\vec{r},t) = -\alpha\frac{E_0^2}{8}\left(\cos^2(\vec{k}_1\cdot\vec{r}-\omega_1 t)+\cos^2(\vec{k}_2\cdot\vec{r}-\omega_2 t)+2\frac{\vec{k}_1\cdot\vec{k}_1}{k_1k_2}\cos(\vec{k}_1\cdot\vec{r}-\omega_1 t)\cos(\vec{k}_2\cdot\vec{r}-\omega_2 t)\cdot\right) \tag{3.8}$$

We take a time average over the optical periods so that the first two terms collective contribution is to shift the potential by $-\alpha E_0^2/8$. For simplicity, we will define $U'(\vec{r},t) = U(\vec{r},t)+\alpha E_0^2/8$ and $\alpha' = \frac{\alpha}{4}\frac{\vec{k}_1\cdot\vec{k}_1}{k_1k_2}$ and employ a trigonometric identity to write

$$U'(\vec{r},t) = -\alpha'\frac{E_0^2}{2}\left(\cos(\vec{k}_1\cdot\vec{r}-\omega_1 t+\vec{k}_2\cdot\vec{r}-\omega_2 t)+\cos(\vec{k}_1\cdot\vec{r}-\omega_1 t-\vec{k}_2\cdot\vec{r}+\omega_2 t)\right) \tag{3.9}$$

We again time average over optical periods (in this case $2\pi/(\omega_1+\omega_2)$) and are left with a potential in the form of a traveling wave

$$U'(\vec{r},t) = -\alpha'\frac{E_0^2}{2}\cos\left(\vec{k}\cdot\vec{r}-\omega t\right) \tag{3.10}$$

where $\vec{k} = \vec{k}_1-\vec{k}_2$ and $\omega = \omega_1-\omega_2$. To find the magnitude of $|\vec{k}|$ we write

$$|\vec{k}| = k = \sqrt{(k_1-k_2\cos\theta)^2+k_2^2\sin^2\theta} \tag{3.11}$$

where θ is the angle between the two Bragg beams. We simplify the above knowing that $|\vec{k}_1|\approx|\vec{k}_2|$ (as both Bragg beams are derived from the same laser) and define $k_{1,2} = |\vec{k}_1|$ giving

$$k = 2k_{1,2}\sqrt{\frac{1-\cos\theta}{2}} = 2k_{1,2}\sin\frac{\theta}{2} \tag{3.12}$$

A cartoon of such an arrangement is shown in Fig. 3.4 to illustrate the moving grating picture. The optical lattice travels through the condensate at velocity $c = \omega/|k|$. This potential lattice will in turn transfer its momentum k to the gas, resulting in a momentum excitation in the gas of wavevector $\vec{k} = \vec{k}_1 - \vec{k}_2$. This process is quite similar to Bragg scattering, where the stationary crystal lattice changes the momentum of the incident X-rays, while in Bragg spectroscopy, the incident optical lattice changes the momentum of the stationary deBroglie waves of the atoms.

The moving grating picture is useful in conceptualizing Bragg excitation in a BEC. One can compare the wavelength of the excitation, $2\pi/k$, to the healing length. One can imagine that lattice spacings longer than the healing length are allowed to modify the BEC wavefunction, and in doing so coherently result in collective excitations. Short-wavelength lattice, on the other hand, vary on a lengthscale smaller than that which the condensate wavefunction can change. Here the only BEC response is to promote a particle from the condensate to a single-particle excitation.

Laser stability requirements are also easily born out of the moving grating picture. Naively, one might expect that the relevant parameter for laser stability would be the linewidth of the laser compared to that of the Bragg spectrum (what sets this width will be discussed in Section 3.4.1). This could mean laser linewidths of a few 100 Hz![3] In truth, it is the *interference* between the two beams that make the Bragg grating, meaning that the relevant comparison is between the coherence length of the laser and k^{-1}. Because coherence lengths of diode lasers are typically on the order of several cm, and the Bragg grating spacing at most a micron, this is rarely an issue. This does, however, point to requirements for stability of posts and various other mounted optics in a Bragg experiment, as significant amounts of vibrations, coupled to a mirror for example, could be enough to perturb the Bragg grating.

[3] While this might seem trivial in the eyes of one Laser General Ye, it would be quite an undertaking for us with our external cavity diode lasers, where our linewidths are typically on the order of 100 kHz.

3.2.2 A 2-photon transition

The picture of Bragg spectroscopy that connects best with the atomic physicist's perspective is that of a coherent, two-photon transition process of absorption of a photon from one laser beam, and stimulated emission of a photon into the other laser beam. This process is diagramed in Fig. 3.5(a). For me, this picture is the most clear in terms of the momentum transfer, as conservation of momentum tells us that the absorption process ($+\hbar\vec{k_1}$) and emission process ($-\hbar\vec{k_2}$) must account for the total momentum transferred to the excitation, ($\hbar\vec{k} = \hbar\vec{k_1} - \hbar\vec{k_2}$).

In the two-photon framework, we show a corresponding level diagram in Fig. 3.5(b). Here, the quantum levels we couple are the zero momentum state and the excited, $\hbar k$ momentum state. We will use a virtual state (dashed line in Fig. 3.5), that is detuned Δ from the electronically excited state, to couple the two momentum states. I particularly like this picture because it shows how the Bragg process is very much analogous to a two-photon Raman transition, where now the traditional $|\uparrow\rangle$ and $|\downarrow\rangle$ states have been replaced by $|k = 0\rangle$ and $|k = k\rangle$ states. Indeed, the atom optics community takes advantage of this coherence and uses Bragg excitation as an "atomic beam-splitter", creating two states whose phase relationship is well defined and set by the interfering Bragg lasers [74].

Of course, with a coherent, two-photon process, there is an associated two-photon Rabi frequency, which we write

$$\Omega_{2\text{-ph}} = \frac{\Omega_1\Omega_2}{2\Delta} \tag{3.13}$$

where Ω_1 (Ω_2) is the Rabi frequency associated with beam 1 (2) and the electronically excited state, and Δ is the detuning between beams 1 and 2 and that same electronically excited state. In Eq. 3.13 we have neglected ω_{exc}, the small frequency difference between beams 1 and 2, as $\omega_{\text{exc}} \ll \Delta$. The two-photon Rabi frequency, in turn, allows us to predict the strength of our Bragg signal. In the low-excitation, linear regime, we have

$$\int_0^\infty \Gamma(\omega)d\omega = S(k)\frac{\pi}{2}\Omega_{2\text{-ph}} \tag{3.14}$$

where $\Gamma(\omega)$ is the scattering rate into the k momentum state and $S(k)$ the static structure factor

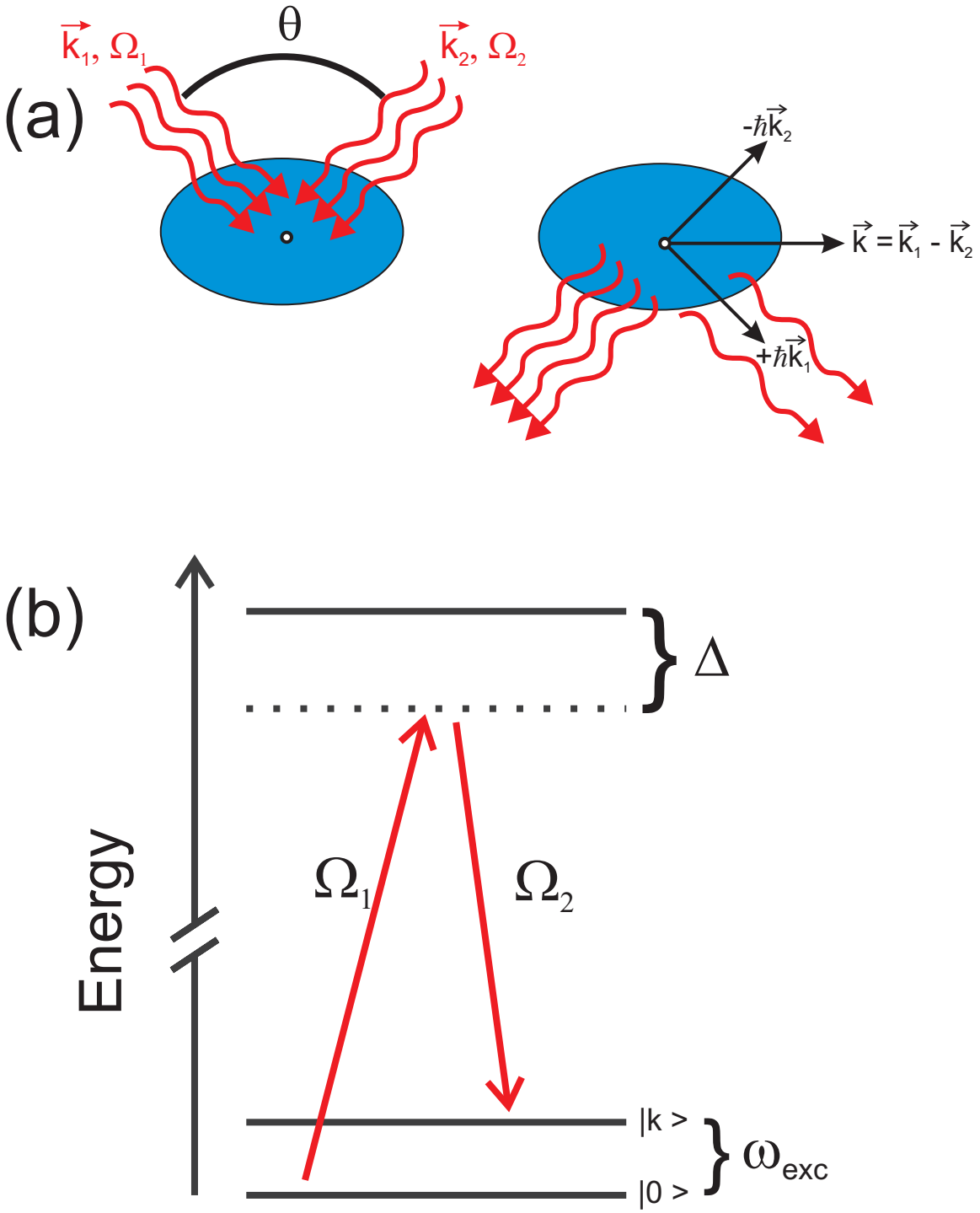

Figure 3.5: Two-photon transition picture for Bragg spectroscopy. (a) Cartoon of absorption of a photon from beam 1 and stimulated emission of a photon into beam 2, and the corresponding momentum transfer. Because momentum must be conserved, this excitation has a net momentum of $k = 2k_{1,2}\sin(\theta/2)$. (b) Level diagram depicting the 2-photon transition. The dashed line represents the virtual state, detuned Δ from the electronic transition (note that $\Delta \gg \omega$). The two light fields used to couple the $|k = 0\rangle$ state and the $|k = k\rangle$ state are described by Ω_1 and Ω_2. The resultant 2-photon Rabi frequency is then $\Omega_{2\text{-ph}} = \Omega_1\Omega_2/2\Delta$.

[75, 76]. We will discuss $S(k)$ in detail later, but typically it is a number between zero and one.

3.2.3 Calculating $\Omega_{\text{2-photon}}$

We would now like to connect the two-photon Rabi frequency to experimental parameters, namely, the intensities of our laser beams. We know that we can write the single-photon Rabi frequency for a two-level system as

$$\Omega_{\text{2-level}} = \frac{1}{\sqrt{2}}\sqrt{\frac{I}{I_{\text{sat}}}}\Gamma \tag{3.15}$$

where Γ is the decay rate (or natural linewidth) of the excited state and $I_{\text{sat}} = \pi hc\Gamma/3\lambda^2$ [77]. In the case of ^{85}Rb, we have $\lambda = 780$ nm, $\Gamma = 2\pi \times 6.07$ MHz and $I_{\text{sat}} = 1.67$ mW/cm^2 [78]. We note that I_{sat} is defined for a "cycling" transition of ^{85}Rb.[4]

In most cases, one does not have a two-level system, as there are often many possible states. We account for this by rewriting the two-level Rabi frequency for arbitrary initial and final states, essentially scaling I_{sat}. The scaling is given by the appropriate coupling between the dipole moment ($e\vec{r}$) and the polarization of the light ($\hat{\epsilon}$), normalized to the cycling transition. We thus write

$$\Omega = \frac{1}{\sqrt{2}}\sqrt{\frac{I}{I_{\text{sat}}}}\Gamma\frac{\langle F_f', m_f|\hat{\epsilon}\cdot e\vec{r}|F_i, m_i\rangle}{\langle F' = 4, m = -4|\hat{\epsilon}(\sigma^-)\cdot e\vec{r}|F = 3, m = -3\rangle_{\text{stretch}}} \tag{3.16}$$

For laser light driving the cycling transition, we recover Eq. 3.15.

We can rewrite Eq. 3.16 in terms of Clebsch-Gordan coefficients (given in references like [78, 77]). Invoking the proper selection rules, we have

$$\Omega = \frac{1}{\sqrt{2}}\sqrt{\frac{I}{I_{\text{sat}}}}\Gamma\sum_{\Delta F,\Delta m} c_{\Delta F,\Delta m}P_{\Delta m} \tag{3.17}$$

where $c_{\Delta F,\Delta m}$ are the Clebsch-Gordan coefficients that couple the initial state $|F_i, m_i\rangle$ to the final state $|F' = F_i + \Delta F, m_f = m_i + \Delta m\rangle$, normalized to the stretch transition. $P_{\Delta m} = \hat{\epsilon}\cdot\vec{r}$ describes the coupling between the photon and the atomic transition, able to drive $\Delta m = \pm 1, 0$ transitions, and normalized so that $P_{+1}^2 + P_{-1}^2 + P_0^2 = 1$.

[4] For example, in ^{85}Rb a cycling transition would be perfect σ^- light coupling the $|F = 3, m_F = -3\rangle$ to the $|F' = 4, m_F = -4\rangle$ transition.

We can now extend this to the case of a coherent, two-photon transition. From Eq. 3.13 we write

$$\Omega_{\text{2-ph}} = \frac{\Omega_1\Omega_2}{2\Delta} = \frac{\sqrt{I_1 I_2}}{4\Delta I_{\text{sat}}}\Gamma^2 \sum_{\Delta F,\Delta m} c_{\Delta F1,\Delta m1} c_{\Delta F2,\Delta m2} P_{\Delta m1} P_{\Delta m2} \delta_{\Delta F1,\Delta F2} \delta_{\Delta m1,\Delta m2} \tag{3.18}$$

where we have introduced the Kronecker delta function because by definition in Bragg spectroscopy our atoms do not change their hyperfine states in the process. We introduce I_1 and $P_{\Delta m1}$ as the intensity and polarization of the transition for laser beam 1, and likewise for laser beam 2. Imposing the conditions of the Kronecker delta function leaves us with

$$\Omega_{\text{2-ph}} = \frac{\sqrt{I_1 I_2}}{4\Delta I_{\text{sat}}}\Gamma^2 \sum_{\Delta F,\Delta m} |c_{\Delta F,\Delta m}|^2 P_{\Delta m1} P_{\Delta m2} \tag{3.19}$$

We take, as an example, the case of ^{85}Rb at low magnetic field, with our atoms in the $|F = 2, m_F = -2\rangle$ state. We will assume that both beams are launched parallel to the magnetic field axis, and the light is linearly polarized driving $\Delta m = \pm 1$ transitions. We write the polarization of the beams as $P_{+1} = P_{-1} = 1/\sqrt{2}$. From the Clebsch-Gordan coefficients, then

$$\Omega_{\text{2-ph}} = \frac{\sqrt{I_1 I_2}}{4\Delta I_{\text{sat}}}\Gamma^2 \left(\frac{2}{3}\right) \tag{3.20}$$

This factor of 2/3 is not all that surprising, as this is the limit for far-detuned light, regardless of polarization; this is pointed out in Ref. [78].[5]

We have measured the Bragg response by counting the number of atoms transferred to the $\hbar k$ momentum excitations and integrating the lineshape to calculate $S(k)$, in turn giving a measured Rabi frequency as established by Eq. 3.14. We can also predict a Rabi frequency from the measured intensities of the laser beams at the atoms and find that our predicted scattering rate agrees reasonably well. We do, however, observe a systematically lower response (~ 20 %) than Eq. 3.20 would predict, which we can attribute to a number of factors. In particular, misalignments of the polarization between beams 1 and 2 would systematically lower our scattering rate. Collisions between the excited fraction and the BEC before imaging would also contribute to a lower measured scattering rate, since this would reduce the number of atoms imaged at $\hbar k$ momentum.

[5] This is a *very* useful result, since typically we perform these experiments at high magnetic field ($\sim$ 160 G) where F and m_F are no longer good quantum numbers for the excited state and the Clebsch-Gordan analysis is more complicated.

3.3 Structure factor: $S(k)$

The static structure factor, $S(k)$, and what it means in the context of condensed matter physics can fill a textbook chapter all by itself [79]. In this section, we will discuss $S(k)$ in the context of Bragg measurements and interacting condensates. In general, $S(k)$ is defined as the Fourier transform of the density correlation function, and is unity for an uncorrelated gas.

The proud parent of $S(k)$ is the dynamic structure factor $S(k,\omega)$, where $S(k) = \int_0^\infty S(k,\omega)d\omega$. In fact, were it not for the broadening mechanisms inherent in Bragg experiments, our lineshapes frequency dependence would exactly correspond to the dynamic structure factor. In addition, one can take ω_0 to be $\int \omega S(k,\omega)d\omega$.

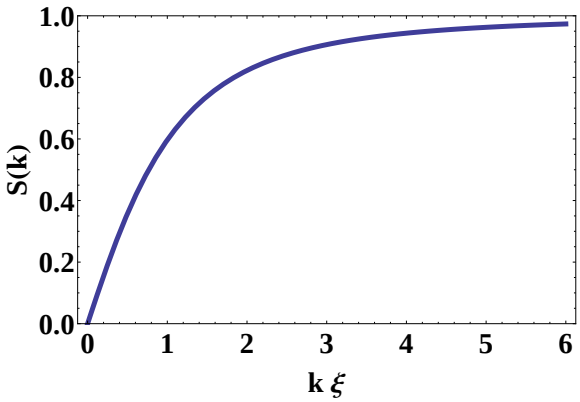

Figure 3.6: Predicted static structure factor from Eq. 3.21 for a weakly interacting condensate. Vertical axis is the structure factor, $S(k)$, while the horizontal axis corresponds to the wavevector of the excitation, k, normalized to $1/\xi$. $S(k) = 1$ is what one would expect for an uncorrelated gas. Experimentally, smaller $S(k)$ means a Bragg transition that requires more laser intensity for the same scattering rate.

The structure factor's importance in Bragg spectroscopy experiments is elucidated in Eq. 3.14, which gives the strength, or scattering rate, of the Bragg process. From Feynman's relation [72], $S(k) = (\hbar k^2/2m)/\omega_0$, we can predict $S(k)$ for a trapped condensate and write [80]

$$S(k) = \frac{15}{4}\left(\frac{3+\beta}{4\beta^2} - \frac{3+2\beta-\beta^2}{16\beta^{5/2}}\left(\pi + 2\arctan(\frac{\beta-1}{2\sqrt{\beta}})\right)\right) \tag{3.21}$$

where

$$\beta = 2gn_{\rm pk}/\left(\frac{\hbar^2 k^2}{2m}\right) \tag{3.22}$$

We plot the predicted $S(k)$ for a weakly interacting BEC, at zero temperature, in Fig. 3.6. One notes that for large $k\xi$, $S(k)$ approaches unity, indicating a lack of correlations. On the other hand, in the phonon regime, $S(k)$ approaches zero. This is due to quantum depletion, which takes atoms from the zero momentum state and promotes them to low-energy excitations at low k [33]. Because these phonons excitations are generated in pairs of $\pm\hbar k$ with opposite phase, they tend interfere destructively and suppress density fluctuations, resulting in $S(k) < 1$ [70, 27]. Experimentally, $S(k) < 1$ has the effect of making the excitations harder to drive for the same $\Omega_{\text{2-photon}}$, so that one has a lower Bragg scattering rate.[6]

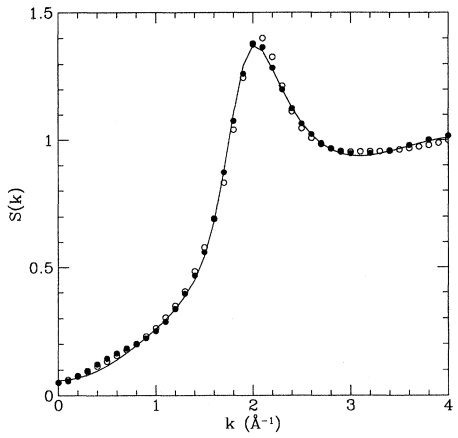

Figure 3.7: Measured $S(k)$ for He, reprinted from Ceperley [81], where the vertical axis corresponds to $S(k)$ and the horizontal axis to the wavevector of the excitation, given in inverse angstroms. Notice the peak in $S(k)$, where $S(k)$ is greater than one, occurs at the same momentum as the roton minimum. Black circles correspond to neutron scattering experiments, white circles to X-ray scattering and the solid line is a path-integral Monte Carlo calculation.

In superfluid Helium, $S(k) > 1$ at the roton minimum. We reprint measurements of $S(k)$ done on He II in Fig. 3.7 [81]. This peak in $S(k)$ can be understood through the aforementioned Feynman relation. The static structure factor, then, presents the experimenter with another measurable

[6] We should note that the above results are in the zero temperature limit. For finite temperatures $S(k)$ is *greater* than unity for $k\xi < 1$ [33]. This has yet to be experimentally observed, however. With the current techniques of measuring the Bragg response, the contributions from thermal excitations cancels out [70].

observable of a roton excitation.

In light of the He II peak in $S(k)$, the structure factor for an atomic gas BEC at large na^3 has been calculated using Monte-Carlo techniques [82]. These calculations also revealed a corresponding peak in $S(k)$, which is analogous to that of a roton. The results from Steinhauer *et al.* show that for an $na^3 = 0.011$ (which corresponds to an LHY correction to the energy density of 64%) a maximal value of $S(k) = 1.08$ is found. It should be noted that this, however, is a non-universal result, as the peak in $S(k)$ is sensitive to the inter-atomic potential at lengthscales of $100a_0$, which corresponds to the effective range of the interaction. We mention this, however, to further illustrate the importance of measurements of $S(k)$ when considering pursuit of the elusive roton.

In light of these observations, we reexamine our 2008 Bragg experiments in Fig. 3.8. Here, we plot $S(k)$ versus the interaction strength. The data has been scaled so $S(k) = 1$ at small values of a. The trend towards smaller $S(k)$ as a increases is due to the excitations approaching the phonon regime, as $k\xi$ also gets correspondingly smaller at larger a. This effect is reflected in the theory line shown in red. Ultimately this data appears too noisy to measure the small peak in $S(k)$ that has been predicted. These experiments would have to be reworked if an accurate measure of $S(k)$ is the goal.

3.4 Challenges in resolving ω_0

While Bragg spectroscopy serves as a powerful probe of strongly interacting BECs, accurately measuring ω_0 is not without its own hurdles. Here I lay out some of the challenges in determining ω_0 from the net Bragg response; these are important to keep in mind for future experiments.

3.4.1 Contributions to the Bragg width, σ

For the goal of resolving ω_0 spectroscopically, it is always the case that, with all things being equal, the smaller the spectral width (σ) of a feature, the better one can measure ω_0. To give a sense of scale, we consider an experiment aimed at measuring the LHY correction at a modest value

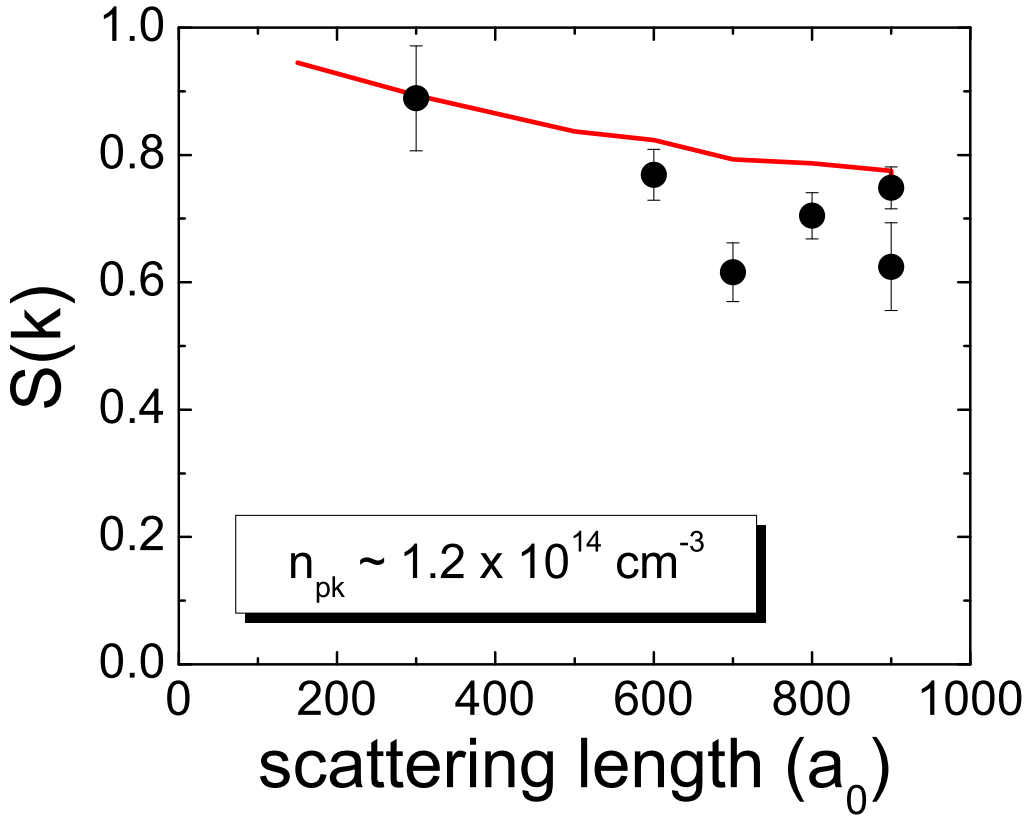

Figure 3.8: Static structure factor measured in the 2008 Bragg experiments (black circles) [54]. We plot $S(k)$ on the vertical axis and the scattering length on the horizontal axis, given in units of Bohr radii. The experimental data has been scaled to give the predicted result in the well-understood case of a weakly interacting BEC, at 300 a_0. The downward trend seen here is indicative of the experiments accessing smaller values of $k\xi$ as the interaction energy is increased (hence $\xi = (8\ \pi n a)^{-1/2}$ is decreased) at fixed $k = 16\ \mu\text{m}^{-1}$. A simple theoretical prediction from Eq. 3.21 illustrating this effect is seen in the red line.

of $na^3 = 6 \times 10^{-4}$. For a typical density in our experiment of 5×10^{12} cm^{-3}, the LHY correction would be 15% of $2\pi \times 350$ Hz worth of interaction energy, or 50 Hz! This illustrates the importance of taking every possible step towards minimizing σ so that one can best measure ω_0. For this reason, we list the factors that contribute to the width of Bragg spectra so that the experimenter can attack these problems head-on. We list all of the factors that we know to contribute to the width of the Bragg spectra in terms of rms gaussian widths, so that we may take all of these factors and add them in quadrature to predict σ.

3.4.1.1 Inhomogeneous density

Provided the density of our gas was homogeneous, the excitations infinitely long lived, with no extraneous mechanisms for broadening, our Bragg lineshapes would be delta functions. Our condensates, however, are trapped, with an inhomogeneous density that is peaked at the center of the trap. In Bragg spectroscopy, different parts of the condensate will have different interaction energies, and hence different, local ω_0.

We therefore use a local density approximation to account for the density distribution of our condensate. Because the density distribution is asymmetric about the average density, the resultant spectrum is correspondingly asymmetric about the average ω_0. We calculate the rms width of this distribution in the single-particle (large $k\xi$) regime and get [83]

$$\sigma_{\text{Inhom S-P}} = \sqrt{\frac{8}{147}} g n_{\text{pk}}/\hbar \tag{3.23}$$

where n_{pk} denotes the peak density of the condensate. In the phonon regime (small $k\xi$), this contribution to the width is approximated as [80]

$$\sigma_{\text{Inhom Ph}} \simeq 0.3\ \bar{c}k \tag{3.24}$$

where $\bar{c} = \frac{32}{15\pi}\sqrt{g n_{\text{pk}}}/m$ is the average speed of sound in the condensate.

3.4.1.2 Fourier broadening

In a perfect world, we would probe the condensate perturbatively, with pulses that were infinitely long and infinitely weak. In reality this is not feasible for our trapped gas, as the duration of the Bragg pulse must be short compared to the trap period in order to have well-defined momentum states for the entirety of the pulse duration. In addition, for experiments where the density is changing (e.g. due to expansion of the cloud or due to collective density oscillations of the BEC) one would also like to keep the pulse length short compared to the timescale for density change, so that the interaction energy, gn, remains relatively constant.

We define Fourier broadening as the energy uncertainty associated with the finite duration of a Bragg pulse, τ_{pulse}, which, more often that not, is the dominant contributor to the spectral width of Bragg lineshapes. Historically, we have used square pulses to turn on and off our Bragg light; this gives rise to the well-known sinc function in the frequency domain. Because the width of our Bragg lineshape will be a convolution of all the broadening mechanisms, we find it useful to approximate the sinc function with a gaussian so that we may add the widths in quadrature. It has been shown that the width of this gaussian due to a square pulse of duration τ_{pulse} is [49]

$$\sigma_{\text{Fourier}} = 2\pi \times \frac{0.36}{\tau_{\text{pulse}}}. \tag{3.25}$$

3.4.1.3 Doppler broadening

As mentioned earlier, the uncertainty principle tells us that the finite size of our condensate comes at the cost of an associated broadening of the BEC momentum distribution, $\Delta p = \sqrt{21/8}\hbar/R$, where R is the size of the BEC in the direction of $\vec{k}$. This momentum broadening gives rise to an associated Doppler broadening of the Bragg lineshape, which is most easily understood in the moving grating picture. The resultant contribution to the Bragg lineshape is then [84]

$$\sigma_{\text{Doppler}} = \sqrt{\frac{21}{8}}\frac{\hbar}{mR}k \tag{3.26}$$

3.4.1.4 Breathes

Just as Δp gives rise to Doppler broadening, so will other contributions to the characteristic width of the BEC momentum distribution. This is particularly important for studies of BEC at different na^3, as breathing modes are often induced after ramping the scattering length (as discussed in Ch. 2), and this can broaden the BEC momentum distribution. For a breathe mode with an rms velocity averaged over the cloud of $\vec{\mathrm{v}}_{\mathrm{breathe}}$, the resultant contribution to the Bragg lineshape width is

$$\sigma_{\mathrm{breathe}} = \vec{\mathrm{v}}_{\mathrm{breathe}} \cdot \vec{k} \tag{3.27}$$

3.4.1.5 Collisional broadening

Scattering of excited atoms will also contribute to broadening of Bragg spectra. A collision can be thought of as a decay mechanism that effectively sets a lifetime on the $|\vec{k}\rangle$ state, and this lifetime in turn results in a lorentzian lineshape. Again, because we typically work in a regime where this is only one factor contributing to the overall width, we make a gaussian approximation to the lorentzian so that we may later add all of the widths in quadrature. The width due to scattering of high momentum excitations in the single-particle regime is given by

$$\sigma_{\mathrm{collision}} = 0.48 \times 8\pi n a^2 \frac{\hbar k}{m} \tag{3.28}$$

3.4.1.6 Momentum uncertainty from the beam waist

In general, Bragg spectroscopy experiments are set up with collimated beams. As we will see in the next chapter, however, there are occasions where it is beneficial to focus the beam down to a small waist. Because of the tight focus of the beam, the k-vector of the light is spread out and this momentum uncertainty contributes a width of its own. Bragg spectroscopy with a tightly focussed beam is referred to as Kapitza-Dirac scattering, and can be used to scatter into multiple momentum states [85, 86]. For a Bragg beam waist of $\mathrm{w}_{\mathrm{laser}}$, we can describe this broadening as

$$\sigma_{\text{K-D}} = \frac{2}{\text{w}_{\text{laser}}} \frac{d\omega}{dk} \tag{3.29}$$

$$\sigma_{\text{K-D}} = \frac{4}{\text{w}_{\text{laser}}\sqrt{2m}} \frac{\hbar^2 k^2/2m + gn}{\sqrt{\hbar^2 k^2/2m + 2gn}} \tag{3.30}$$

3.4.2 σ versus ω_0

Aside from the obvious benefits of minimizing σ for accurate measurements of ω_0, there is another, more subtle motivation that is particularly relevant when measuring a *net* response, such as the total momentum transfer. We have found that the characteristic, antisymmetric shape of our Bragg spectra (positive peak at $+\omega_0$ and negative peak at $-\omega_0$) requires us to keep the ratio of σ/ω_0 small. In Fig. 3.9(a), we show this effect by plotting simulated Bragg spectra of differing widths, keeping the amplitudes and resonance frequencies constant. The relevant parameter when comparing these spectra is σ/ω_0, the ratio of the width to the absolute frequency of the Bragg resonance. Shown are $\sigma/\omega_0 = 0.2, 0.5, 2.0$ in green, blue and red, respectively. The problem, which will manifest itself as a fitting systematic, is that at relatively large widths (e.g. $\sigma/\omega_0 = 0.5$ or 2.0) the two gaussian lineshapes are no longer independent, as one can see in Fig. 3.9(a). In this regime, the competing $\pm\hbar\vec{k}$ lineshapes have "eaten" into each other, resulting in fit parameters that are highly coupled. One can understand the fitting routine's struggle in determining ω_0 at large σ/ω_0 by comparing the dashed black line to the red line in Fig. 3.9(a). The dashed black line here corresponds to an ω_0 that is *twice* that of the red spectrum, yet the two look nearly identical.

To determine the necessary criteria for a trustworthy measurement of ω_0, we simulated Bragg lineshape data and performed least-squares fits to determine ω_0, just as we would in an actual experiment. The results of our analysis are shown in Fig. 3.9(b). Here, we fit to the same antisymmetric gaussian function of the form $A'(e^{-(\omega-\omega_0')^2/2\sigma'^2} - e^{-(\omega+\omega_0')^2/2\sigma'^2})$. We plot the accuracy of the fit (ω_0'/ω_0) versus the relative fitted widths of the lineshapes σ'/ω_0'. From these simulations, we see that once $\sigma'/\omega_0' > 0.5$, significant error is introduced to the measurement of ω_0. *Especially* disconcerting is that this error is not reflected in the error bars returned by our fitting routine. From

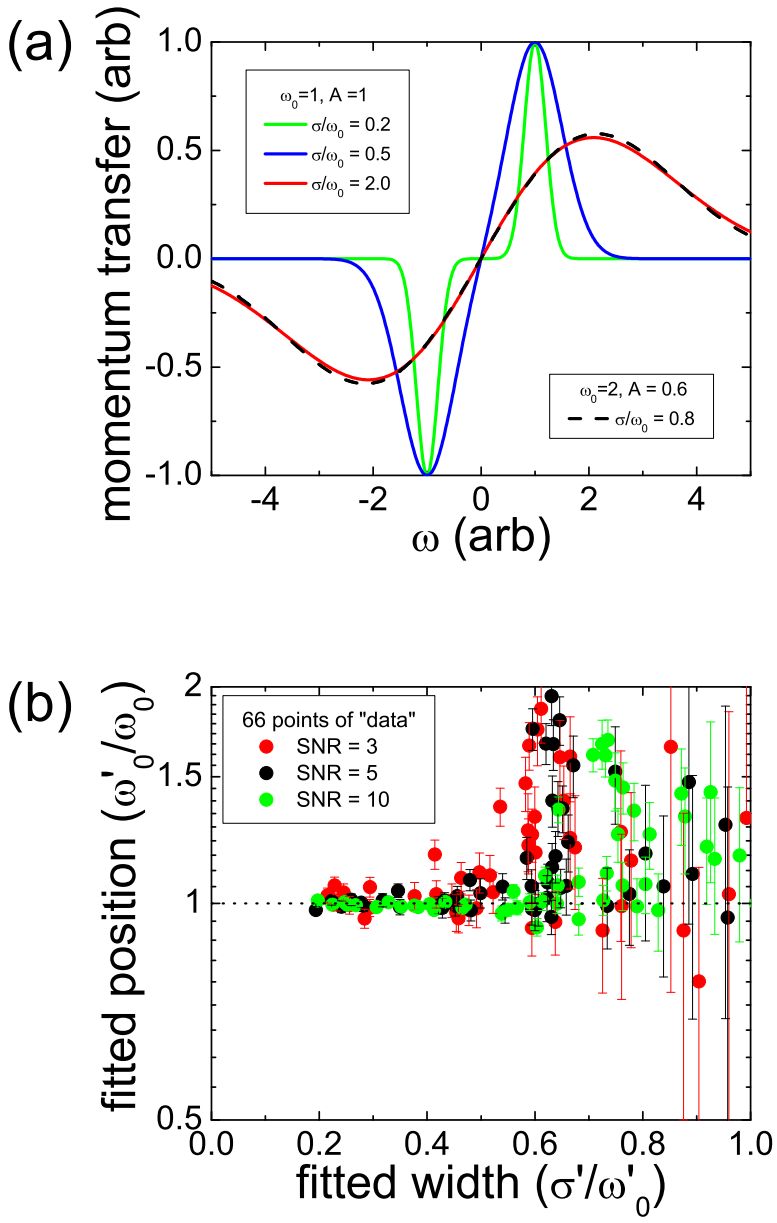

Figure 3.9: Difficulty in measuring ω_0 at large σ/ω_0. (a) Bragg lineshapes illustrating the effects of a large σ/ω_0. Green, blue and red lineshapes all correspond to the same amplitude and resonance ω_0, but have different widths σ (see the legend). The dashed black line, on the other hand, is a lineshape with a factor of 2 larger ω_0 than the red lineshape it resembles. This shows how the parameters of the lineshapes, A, ω_0 and σ are now strongly coupled, making fits of lineshapes with large σ/ω_0 untrustworthy. (b) Results of fits to artificial data generated at various values of σ/ω_0. On the vertical axis is the ratio of the fitted Bragg resonance (ω_0') versus the actual Bragg resonance used to generate the data (ω_0). On the horizontal axis is the fitted width, σ' normalized to ω_0'. The dashed line indicates a good fit, where $\omega_0' = \omega_0$. Different colored points represent different amounts of noise added into the artificially generated data. These "fake" data sets consisted of 66 data points. We add in artificial noise by replacing A with random numbers generated from a normal distribution. The signal-to-noise ratio (SNR) described in the legend is defined as the ratio of the peak to the variance of the distribution used to generate A. In other words SNR $= A/\sigma_{\text{variance}}$. From this analysis we conclude that to accurately determine ω_0, one requires that $\sigma' < 0.5 \times \omega_0'$.

the simulations, we can also see that the general trend is a systematic increase in ω_0'. From these results we conclude that an accurate measure of ω_0 requires that the measured width be less than half the measured resonance position, i.e. $\sigma'/\omega_0' < 0.5$.

3.4.3 Detection

While we have presented a number of hurdles to overcome in the *measurement* of a Bragg signal, another primary concern is the *detection* of a Bragg signal at large na^3. As mentioned, one of the goals of this thesis is to use Bragg spectroscopy to probe smaller values of $k\xi$ while accessing higher values of na^3. The most straightforward way to do this would be to change the geometry of our Bragg beams to access smaller values of k.[7] This is challenging on two fronts. First is the tricky business of measuring low momentum excitations. The groups that have successfully done this employed a great deal of image processing where multiple absorption images are first averaged together to minimize noise. They then performed surface fits on the images with three independent gaussian peaks, corresponding to the original condensate momentum ($\hbar k = 0$) and the peaks at $\pm\hbar k$ momentum. In addition, the condensates used in these experiments are much larger in number (10^7 for the experiments in Ref. [70], 10^5 for the Ref. [27]) than the 4×10^4 we typically work with for ^{85}Rb.

The second complication arises from the small mean free path, given by $(8\pi na^2)^{-1}$ induced by our jump to large a. We found in our ToF images at large na^3 that the cloud we expected at momentum $\hbar k$ had been largely extinguished (see Fig. 3.10). To circumvent this difficulty we borrowed a trick from a colleague, Cindy Regal. After the Bragg pulse, we made the scattering cross-section so large that excitations never had a chance to escape the BEC, but instead deposited their momentum to the center-of-mass (COM) momentum of the gas as a whole. Measuring the change in the COM momentum then gives us the net effect of the Bragg excitations [49].

Practically speaking a marriage of these two techniques is irreconcilable. The small momen-

[7] We note that in Fig. 3.3 the purple line corresponding to the 2008 experiments was done in a much different trap, and hence density, than we currently have, as discussed in Ch. 2. If we were to perform Bragg spectroscopy at $k = 16\ \mu\text{m}^{-1}$ ($\theta = 180^0$) with these new condensates, we would experimentally explore a line that began at $na^3 = 10^{-5}$, $k\xi \sim 10$.

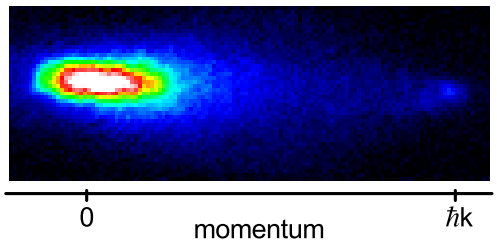

Figure 3.10: Effects of large a on ToF images used in Bragg analysis. Due to the much shorter mean free path at large a, the excitations do not cleanly escape from the condensate during the expansion. This contrasts the behavior at small a shown in Fig. 3.1(a). The scattering of excitation in ToF complicates measuring the Bragg response, as described in the text.

tum we are looking to excite via the Bragg process would shift the COM momentum only a small amount, and our signal-to-noise in the previous experiments was already marginal for the largest values of na^3. What is needed is a different approach to the problem of measuring phonons in a strongly interacting condensate. Our development of one such approach is presented in the next chapter.

Chapter 4

Photon counting for Bragg spectroscopy

In the last chapter we presented the reasons why Bragg spectroscopy is a useful probe in the study of interacting condensates, and we presented our results of Bragg spectroscopy measurements in the strongly interacting regime. However, all of this work at large na^3 has, to date, been performed at relatively high momentum transfers ($k = 16\ \mu\text{m}^{-1}$), where time-of-flight imaging of Bragg excitations in a system with strong interactions was viable. To fully understand the dispersion relation of our system, one would like to probe low-momentum excitations as well. Typical measurement schemes for Bragg excitations would have to be reworked at large na^3 and low-momentum transfer, for reasons put forth in the previous chapter. With this thought in mind we embarked on a new type of measurement technique for Bragg spectroscopy: photon counting.

We present here our efforts and results towards that end, which can also be found in Ref. [87]. This section is meant to not only chronicle our system, but also to present the reader with the necessary knowledge to implement a similar system on their own. I believe that photon-counting for Bragg spectroscopy could be quite fruitful not only for measuring the dispersion of a strongly interacting condensate, but also as a novel probe of cold atomic gases. A few possible experiments are mentioned at the conclusion of this chapter.

4.1 Motivation

Any experiment designed to probe excitations requires the same essential components: a way to excite the sample and a way to measure the response. To drive the excitations one applies a

field to perturb the typically small ($\sim 10^5$) number of atoms, and obtains spectra by measuring the response of the ultracold gas as a function of the driving field frequency. In ultracold atom experiments, this response has almost always been measured in essentially the same way: after the perturbation, the atom cloud is imaged and the response is observed as some change in the density distribution of the imaged cloud.

There exists, however, in any excitation spectroscopy, an alternative way to measure the response of the quantum gas to a driving field. Just as the quantum gas has responded to the probe field, the probe field must have an equivalent response to the quantum gas. In this chapter, we present a technique to measure this complementary information in Bragg spectroscopy by measuring the change in the number of photons in one of the laser fields used to drive the Bragg excitations. While in this work we use Bragg spectroscopy, this technique may more generally be applicable to other excitation spectroscopies as well. For ultracold atoms the challenge, of course, is to have adequate signal-to-noise in measuring photon number to detect the Bragg response. For smallish atom samples, this will typically require a photon shot-noise limited measurement. To that end, we detail the experimental setup and the techniques of a heterodyne based detection scheme used to realize shot-noise limited photon counting. We also explore the advantages and limitations of this technique.

Regardless of the method used to measure a Bragg response, adequate signal-to-noise will always be a prerequisite. The signal is set by the number of Bragg excitations, which is typically less than 10% of the total atoms in the sample in order to probe the linear response. For our ^{85}Rb condensates, that would correspond to some 4,000 excitations. If we allow for 100,000 photons in the weak beam, this corresponds to a signal-to-noise ratio (SNR) of $4,000/\sqrt{2 \times 10^5} = 9$ on resonance. This assumes a quantum efficiency of 1, as well as shot-noise limited detection. With these considerations in mind, it becomes clear that for a successful measurement of a Bragg response using a photon counting technique, only a shot-noise limited measurement on the weak beam photons will suffice.

One well established tool for making shot-noise limited measurements of light is to use de-

tectors in their discrete, or Geiger, mode of operation. Both avalanche photodiodes and photo multiplier tubes can be used for such measurements. The principal behind this technique is to time resolve the individual photons so that one measures them digitally. The advantage of such a measurement is that the photon signal itself is digitized, only has to be above some threshold to register, and hence the noise is of little consequence. However, in considering this option for our purposes, we found that avalanche photodetectors suffer from pulse-pile-up for the powers we use, while photo multiplier tubes suffer from quantum efficiencies in the IR, only 5% or so, which is too low to be useful.

Let us consider the alternative of using detectors in their linear mode of detection. Silicon photodetectors have quantum efficiencies as high as 90% and capacitances on the order of 3 pF. However, for the pulse lengths we seek ($\sim$ 1 ms) the Johnson noise associated with the necessary feedback resistor corresponds to the shot noise of a 1 μW beam at 780 nm and therefore makes direct shot-noise-limited measurements impossible for the powers used in these experiments. Our solution to these challenges is one as old as the AM radio: heterodyning.

4.2 Heterodyne detection

To further motivate heterodyne detection, we consider the following scheme. We direct the weak Bragg beam onto a photodiode, and after some stages of amplification directly measure a voltage, S_{direct} proportional to the number of photons per second incident on the detector. To illustrate the role of shot-noise, we consider our signal to be proportional to the number of photons, N_{weak}, that hit the detector in some time τ. In terms of an average voltage, the signal is $S_{\mathrm{direct}} = Re\eta N_{\mathrm{weak}}/\tau$, where η is the quantum efficiency of the detector, e is the charge of an electron, and R is the transimpedance gain of the amplifier.

The signal-to-noise ratio, SNR_{direct}, on this direct weak beam detection is given by

$$SNR_{\mathrm{direct}} = \frac{Re\eta N_{\mathrm{weak}}/\tau}{\sqrt{\delta_{\mathrm{S}}^2 + \delta_{\mathrm{e}}^2}} \tag{4.1}$$

where the shot-noise associated with the photocurrent is $\delta_S = (Re/\tau)\sqrt{\eta N_{\mathrm{weak}}}$. Other sources of

noise (dark noise from the detector, Johnson noise introduced in the amplification stages, noise on background light incident on the detector, etc.) will be referred to as electronic noise, and are represented by δ_e. Shot-noise limited detection is defined as the regime where δ_e is an insignificant contribution to the total noise ($\delta_e^2 \ll \delta_S^2$). In this case,

$$SNR_{\text{shot-noise}} = \sqrt{\eta N_{\text{weak}}}. \tag{4.2}$$

Shot-noise limited detection is difficult to achieve in direct detection, where for typical experimental values of $\tau = 1$ ms, $N_{\text{weak}} = 10^5$, $\eta = 85$ %, we might expect $\delta_e = 500 \times \delta_S$ for the 0.001 pA/$\sqrt{\text{Hz}}$ of a low-noise transimpedance preamplifier.

We use a heterodyne scheme to overcome these difficulties. The idea of heterodyne detection is to amplify the signal *optically* before detection, so that electronic noise is of no consequence. We do this by measuring the beat of the weak beam against another, more intense beam, which we will refer to as the local oscillator (*LO*). Because the beat signal, S_{beat}, goes as the square root of the product of the intensities of the weak and the LO beam, we are left with a signal that is much stronger than that of the original, weak beam signal.

For the purposes of illustrating the heterodyne technique, we describe the weak and *LO* field as plane waves

$$\mathbf{E}_{\text{weak}} = E_{\text{weak}} \cos(kz - \omega_{\text{weak}} t)\hat{\mathbf{x}} \tag{4.3}$$

$$\mathbf{E}_{\text{LO}} = E_{\text{LO}} \cos(k'z - \omega_{\text{LO}} t + \phi)\hat{\mathbf{x}} \tag{4.4}$$

where we have included a relative phase, ϕ. When we spatially overlap the laser fields by matching the modes of the beams to make k' as close as possible to k, the resulting beat field is

$$\mathbf{E}_{\text{beat}} = \mathbf{E}_{\text{weak}} + \mathbf{E}_{\text{LO}} \tag{4.5}$$

Of course, what we measure are not the fields themselves, but rather the total power at the photodetector. After time-averaging over optical frequencies (represented by the angled brackets below), we write the optical power of the overlapped beams as

$$P_{\text{beat}} = c\epsilon_0 \langle |\mathbf{E}_{\text{beat}}|^2 \rangle = c\epsilon_0 \left(\frac{E_{\text{weak}}^2}{2} + \frac{E_{\text{LO}}^2}{2} + C E_{\text{weak}} E_{\text{LO}} \cos(\Delta\omega t + \phi)\right) \tag{4.6}$$

where $\Delta\omega = \omega_{\rm LO} - \omega_{\rm weak}$, and for simplicity, we have assumed $z = 0$. The contrast, C, is a number between zero and one that describes the quality of the mode-matching between the two beams.

The signal of interest to us is the amplitude of the heterodyne signal at frequency $\Delta\omega$. To measure this signal, we shine both beams onto a photodiode and then send the resultant photocurrent to a double-balanced mixer. The mixer is driven by an rf source at frequency $\Delta\omega$, thereby mixing down the heterodyne signal to DC at the mixer output. We then use a low-pass filter on the output, leaving only frequencies well below $\Delta\omega$.

After filtering and amplification our signal in volts is

$$S_{\rm beat} = \frac{Re\eta}{hc/\lambda} P_{\rm beat} = (2CRe\eta/\tau)\sqrt{N_{\rm LO} N_{\rm weak}}\cos\phi \tag{4.7}$$

where the transimpedance gain, R, includes the gain from the mixer. As one can see, our signal goes as $\cos\phi$, the phase difference between the two Bragg beams. Later we will show how we measure the other quadrature of this signal, which goes as $\sin\phi$. For now, however, we will assume that $\phi = 0$ for simplicity, and we have a SNR of

$$SNR_{\rm beat} = \frac{2CRe\eta\sqrt{N_{\rm LO} N_{\rm weak}}/\tau}{\sqrt{\delta_S^2 + \delta_e^2}} \tag{4.8}$$

The advantage of heterodyne is that one may arbitrarily increases the intensity of the *LO* light, so that the shot noise from the *LO* dominates the electronic noise, as well as the shot-noise from the weak beam itself. The total noise is then

$$\sqrt{\delta_S^2 + \delta_e^2} \simeq \delta_S = (Re/\tau)\sqrt{\eta N_{\rm LO}} \tag{4.9}$$

and we are left with

$$SNR_{\rm beat} = 2C\sqrt{\eta N_{\rm weak}} \tag{4.10}$$

Of interest to us, of course is the weak signal, rather than that of the beat. The corresponding SNR of $N_{\rm weak}$ is then

$$SNR_{\rm weak} = \frac{1}{2} SNR_{\rm beat} = C\sqrt{\eta N_{\rm weak}} \tag{4.11}$$

which, for perfect contrast ($C = 1$), realizes our stated goal for a shot-noise limited measurement as in Eq. 4.2. These principles of optical heterodyning are well established, and we refer the reader to Refs. [88, 89, 90] for a more thorough discussion.

Keep in mind that to this point the SNR we have been considering is that of the weak beam. For the actual Bragg experiments our signal is not the weak beam, but N_{Bragg}, the number of Bragg excitations. These Bragg excitations are subtraction measurements, measured with respect to a background number of weak beam photons. We can write the associated signal-to-noise ratio as

$$SNR_{\mathrm{Bragg}} = \frac{1}{\sqrt{2}} \frac{N_{\mathrm{Bragg}}}{N_{\mathrm{weak}}} SNR_{\mathrm{weak}} = \frac{C\sqrt{\eta}}{\sqrt{2}} \frac{N_{\mathrm{Bragg}}}{\sqrt{N_{\mathrm{weak}}}}. \tag{4.12}$$

From Eq. 4.12 one can see that to maximize the SNR of a Bragg experiment one would like to both maximize the number of Bragg photons (again, typically fixed by the overall condensate number) while minimizing the number of weak beam photons. The tradeoffs of such requirements for optimum signal-to-noise ratios will be discussed in following sections.

The measured LO shot noise also serves to calibrate the overall gain of our system, R. Provided one knows η (which is readily available from the photodiode's datasheet) and has a calibration for N_{LO} (which is straightforward for the relatively high power of the LO beam), one can rewrite Eq. 4.9 as

$$R = \delta_S \frac{(\tau/e)}{\sqrt{\eta N_{\mathrm{LO}}}} \tag{4.13}$$

4.3 Layout and construction

While the principle behind shot-noise limited heterodyne detection is straightforward, the implementation of such a technique has a number of subtleties which we lay out here. We illustrate both the optical and the rf design in Fig. 4.1. The two Bragg beams, which we label "weak" and "strong", intersect at the location of the BEC. The third, much more intense LO beam functions only to amplify the weak beam for our heterodyne detection, and avoids the atoms altogether. All three beams are derived from the same laser, and are offset in frequency after passing through

acousto-optical modulators (AOM). The rf sources driving the AOMs are phase-locked to each other in order to ensure coherence between the Bragg beams. The weak and LO beams are combined on a beamsplitter that provides good spatial overlap of the two beams, but causes some attenuation of the weak beam. This, along with other sources of attenuation (e.g. scattered weak beam light from the cell wall, imperfect reflections off of mirrors, etc.) can be included in Eq. 4.11, simply by replacing η with a lower, effective quantum efficiency for the detection system. For the best signal-to-noise ratio we would like to measure as much of the weak beam as possible. This must be balanced, however, with our need for large enough LO power to overwhelm the electronic noise. Typically, we work with 90% reflection of the weak beam and 10% transmission of the LO beam, which corresponds to 250 μW of LO power.

In the following sections, we discuss how we maximize our SNR for the photon-counting technique. We begin the discussion with the considerations of the optical design, and then move on to the rf considerations.

4.3.1 Mezzanine level

A primary challenge for shot-noise limited detection with a heterodyne interferometer is to minimize any jitter in the relative phase (ϕ) between the two beams. As we will see later, this phase jitter introduces noise that prevents us from achieving shot-noise limited detection for long Bragg pulses. We find that the biggest source of instability in the relative phase is due to the optical fibers. These fibers are sensitive to mechanical vibrations and acoustical noise. Therefore, we use relatively short fibers, 1 m in length, to minimize phase jitter between the two beams, while still providing the necessary filtering of the spatial mode. In order to have such short fibers, we built the Bragg optics shown in Fig. 4.1 on a small breadboard erected above our larger optical table. We lovingly refer to this as the mezzanine level, which can be seen in Fig. 4.2. Also shown in the figure are the various other steps we have taken to reduce the coupling of mechanical vibrations to the fibers: these steps are described in the caption. We found that minimizing the physical contact between the fibers and other elements, such as posts, proved crucial in achieving shot-noise limited

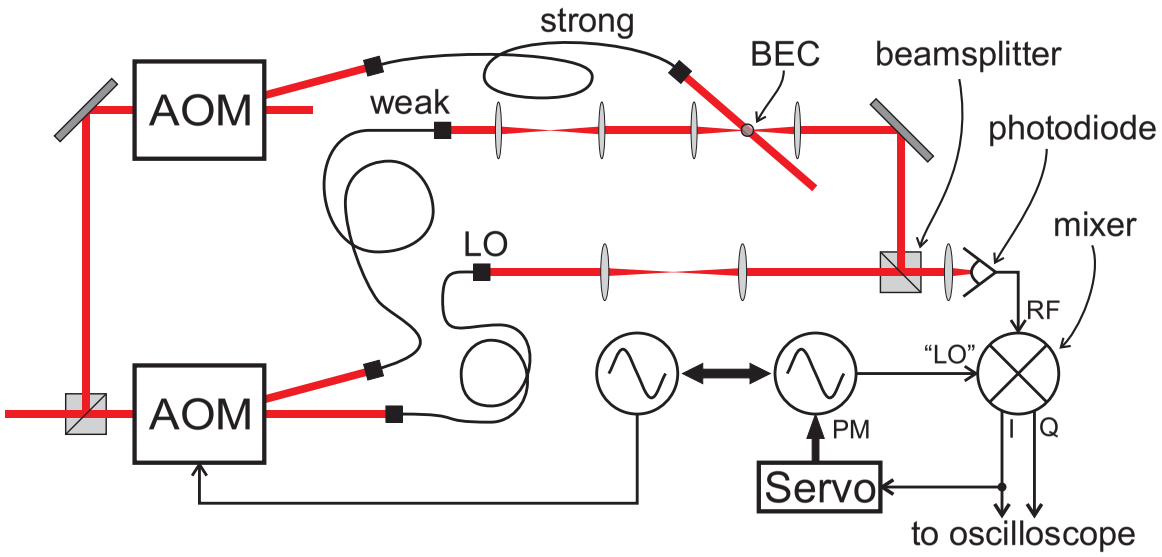

Figure 4.1: Diagram of the heterodyne setup for Bragg scattering via photon counting. Three beams (labeled weak, LO and strong) are derived from the same laser source and individually fiber coupled. The optics for the LO telescope are chosen to give the same spatial mode as that of the weak beam. After being combined on a beamsplitter, the weak and LO beams illuminate a photodiode and the beat signal is sent to a demodulating mixer. The two quadrature outputs of the demodulator, I and Q, are sent to an oscilloscope for the measurement. Also illustrated in the figure is a servo loop that functions to minimize the phase fluctuations between I and Q. The servo minimizes the demodulator output, I, by feeding back to a phase modulation port of the synthesizer that drives the LO port of the mixer. This synthesizer is phase-locked to the synthesizer driving the weak beam AOM. Not shown in the schematic is the synthesizer driving the strong beam AOM, which is also referenced to the weak AOM synthesizer.

measurements on longer timescales.

4.3.2 Contrast

A principal challenge in maximizing the signal-to-noise ratio of the heterodyne detection is achieving a contrast, C, as close to unity as possible. In Eq. 4.11, we see that the signal-to-noise ratio scales linearly with the contrast. Therefore, we would like the best possible mode-matching between the two beams, both spatially as well as in terms of polarization. In light of these two requirements, we launch the two beams into identical, polarization-maintaining fibers (shown in Fig. 4.1 and Fig. 4.2). The weak and the LO beams subsequently pass through different sets of lenses, which serve to match the focussed size of the weak beam to that of the BEC, as well as to match the spatial mode of the LO beam to that of the weak when they recombine on the beamsplitter. To avoid interactions between the intense LO light and the atoms, the LO beam has its own optical path that avoids the vacuum chamber and the atoms. In addition, we have an optical isolator (not shown in figure) in between the beamsplitter and the photodiode to extinguish LO light backreflections off of the photodiode that interact with the atoms.

To measure and maximize the contrast we replace the light launched into the weak beam fiber with light at the same frequency as the LO. With this homodyne interferometer, one can easily assess the quality of the contrast by eye, by looking at the pattern of the interference fringes, as shown in Fig. 4.3(a). Our procedure is to first align the beam such that the fringes are a circular pattern of rings, as seen in Fig. 4.3(b). We then optimize the collimation of the LO beam (achieved by manipulating the relative distance between two lenses in the LO telescope) by minimizing the total number of rings, and are left with an interference pattern like that shown in Fig. 4.3(c). We found this to be an essential step in getting good contrast.

Once the beams are closely mode matched by eye, we perform the final steps of alignment by directly monitoring the DC output of the photodetector. We found it useful to modulate the phase of one of the beams, enough to wrap around 2π, by placing a glass slide in one of the beam paths. This slide was angled so that its surface made an acute angle with the beam. We mounted this

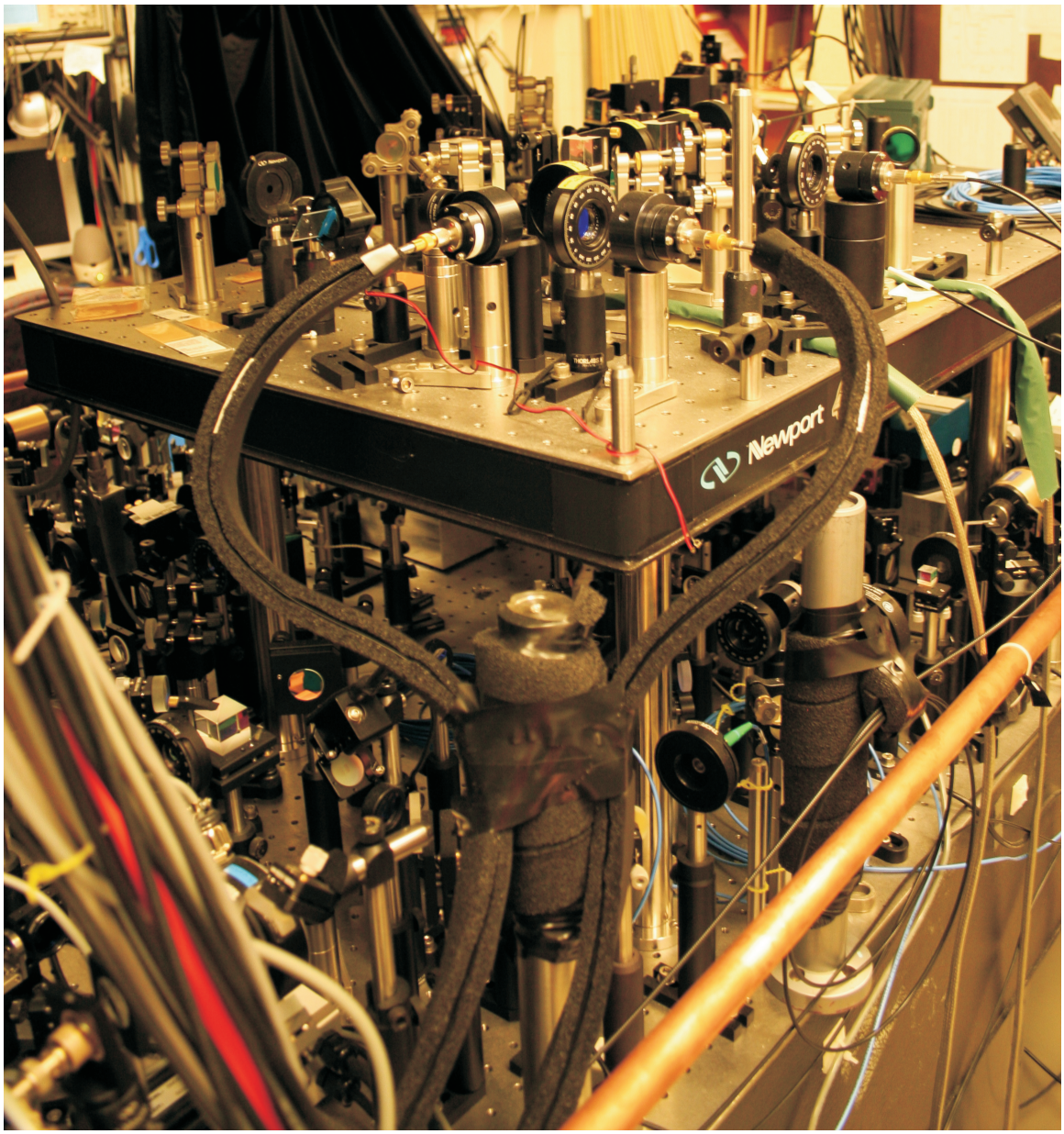

Figure 4.2: A photograph of our newly remodeled optical table, showing what we refer to as the "mezzanine level". We found this additional breadboard necessary so that we could work with short, 1 m fibers. Several steps were taken to reduce phase jitter between the two beams. Large, 1/2 inch posts are used for all of the optics on the mezzanine. The weak and LO fibers are both wrapped in foam to minimize acoustical coupling to the fibers through air. We also minimize the number of times these fibers physically connect to the table or other posts. Two places are unavoidable: the input and output fiber couplers. We managed to only have the fibers touch one more post in the system, and here we have heavily wrapped the contact point with foam, as shown in the picture. Finally, the mezzanine itself is supported by 4 posts that are filled with lead shot to further dampen vibrations.

slide on a oscillating motor that would rotate the slide roughly 20° about its described equilibrium position. This phase wrapping gives us both fully constructive (P_{const}) and fully destructive (P_{dest}) interference. Using the measurements of P_{const} and P_{dest} we are able to quantify the contrast by analyzing Eq. 4.6. For the case of homodyne, $\Delta\omega = 0$ and we can take Eq. 4.6 and write fully constructive interference as

$$P_{\text{const}} = c\epsilon_0(\frac{E_{\text{weak}}^2}{2} + \frac{E_{\text{LO}}^2}{2} + CE_{\text{weak}}E_{\text{LO}}) \tag{4.14}$$

and fully destructive interference as

$$P_{\text{dest}} = c\epsilon_0(\frac{E_{\text{weak}}^2}{2} + \frac{E_{\text{LO}}^2}{2} - CE_{\text{weak}}E_{\text{LO}}). \tag{4.15}$$

If we then evaluate

$$\frac{P_{\text{const}} - P_{\text{dest}}}{P_{\text{const}} + P_{\text{dest}}} = C\left(\frac{2E_{\text{weak}}E_{\text{LO}}}{E_{\text{weak}}^2 + E_{\text{LO}}^2}\right) \tag{4.16}$$

Which, if one is careful to balance the powers of the weak and the LO beam so that they are equal, reduces to

$$C = \frac{P_{\text{const}} - P_{\text{dest}}}{P_{\text{const}} + P_{\text{dest}}} \tag{4.17}$$

4.3.3 Strong beam

A stated goal is to minimize the total number of photons in the weak beam. If one hopes to keep the excitation rate (and hence the signal) constant for very low weak beam intensities, the intensity of the strong beam must be correspondingly increased (recall Eq. 3.13 $\Omega_{2\text{-ph}} = \frac{\Omega_1\Omega_2}{2\Delta}$). Note that this large mismatch between the two Bragg beam intensities is quite different from the usual situation when using atom-response detection, where there is no reason not to have equal intensities in the two beams.

Single photon processes, in particular off-resonant scattering of the stronger beam, limits the maximum permissible intensity in the strong beam, and this is one limit on the minimum photon number in the weak beam. We write the off-resonant scattering rate as [77]

$$\Gamma_{\text{off-resonant}} = \frac{(I/I_{\text{sat}})(\Gamma/2)}{1 + I/I_{\text{sat}} + 4(\Delta/\Gamma)^2} \tag{4.18}$$

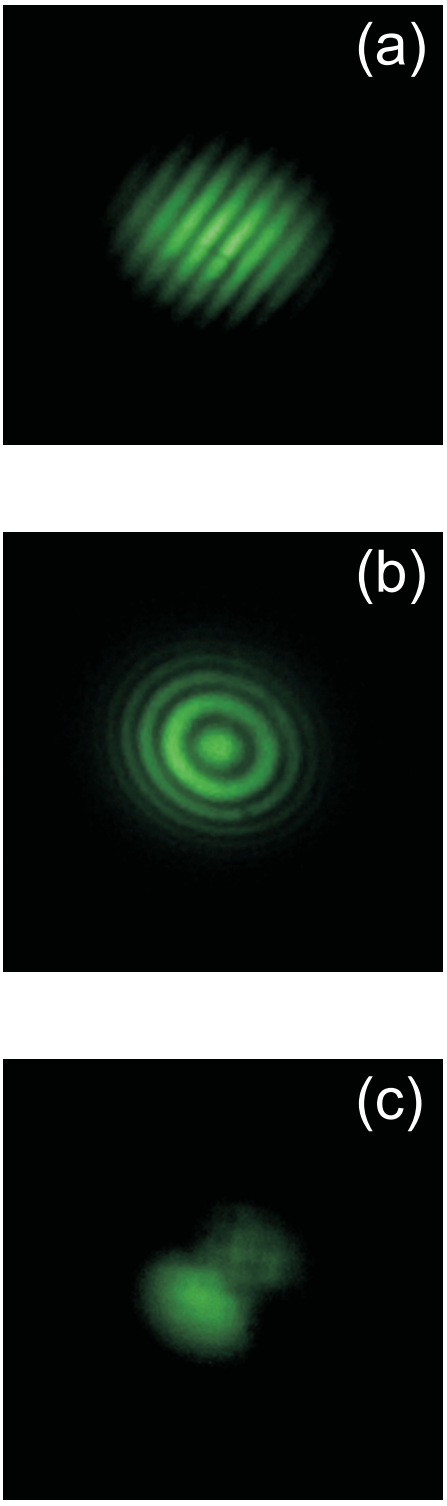

Figure 4.3: Pictures of homodyne interference fringes used for coarsely tweaking up the contrast. Both beams here at roughly equal powers. A -5 cm focal length lens was used to better see the fringes, which are incident on a white index card and seen through an IR viewfinder. (a) Densely packed parallel fringes indicating a large misalignment between the two beams. From these initial interference patterns one walks one of the beams so that the fringes become less dense and begin to look more circular, as in (b). Once the fringes are centered and circular all that is left to do is to manipulate the collimation of one of the beams, again trying to reduce the density of the rings until one is left with something like (c). From here one can use the DC output of the heterodyne photodiode to maximize the contrast, as described in the text.

where I is the intensity of the light, I_{sat} is the saturation intensity, defined in Ch. 3, Γ is the natural linewidth of the electronic transition, and Δ the detuning of the light from the electronic transition. In the limit of large detuning, which is typical for Bragg experiments, the off-resonant scattering can be approximated as

$$\Gamma_{\text{off-resonant}} \approx \frac{\Gamma I/I_{\text{sat}}}{8(\Delta/\Gamma)^2} \tag{4.19}$$

One can ask if there is any benefit to working at a larger detuning, as $\Gamma_{\text{off-resonant}}$ goes as $1/\Delta^2$. However, the Bragg excitation rate (in the low excitation regime) go as $\Omega_{\text{2-ph}}^2$ and has the same $1/\Delta^2$ dependence on the detuning. Hence, whatever is won in terms of a reduced single-photon scattering rate at larger Δ is subsequently lost in the signal. In other words, for a fixed weak beam intensity and Bragg excitation rate, we will always suffer the same amount of strong beam scatter, in the limit of large detuning.

As the effects of strong beam scatter are independent of Δ, we choose to work with a smaller detuning of $2\pi \times 2.3$ GHz compared to our previous Bragg experiments [54]. We do this to minimize the amount of rf that is sent to the strong beam AOM, as it is picked up on our photodiode, writing extra noise to our weak beam measurements. Working at smaller detunings allows us to access higher $\Omega_{\text{2-ph}}^2$ for the same amount of rf power sent to the AOM.

4.3.4 LO beam

The LO light provides optical gain for the weak beam. Because this LO power is used to ultimately determine the number of photons we detect in the weak beam (see Eq. 4.7) we find it useful to servo the power of the LO beam to keep it from drifting shot-to-shot. We do this by monitoring the DC output of the photodiode used for the heterodyne detection and actively feeding back to a AOM that controls all of the Bragg light power before it is split off for the strong, weak, and LO beams. It was hoped that the reduced intensity noise might make our photon-counting quieter on a per-shot basis, but this was not the case. This would be understandable if the LO power drift were caused by something that only affected the LO beam path and not the weak beam, as the servo would be quieting the LO beam at the expense of making the weak beam noisier. This

further supports our belief that the ultimate limit on the photon-counting noise performance is not intensity noise of the laser beams but phase jitter.

In spite of putting much care into diverting the LO beam from the science chamber (ensuring that it does not interact with the condensate), we still saw an effect of the LO light on the BEC. We tracked this down to light that had been reflected off the face of the photodiode and made it back to the atoms via the weak beam path. We subsequently installed an optical isolator just before the photodiode and fixed this issue.

4.3.5 Weak beam

For the best signal-to-noise, provided a shot-noise limited measurement is available, we need to minimize the total number of photons in the weak beam, as seen in Eq. 4.12. One consideration in the weak beam photon number is the spatial profile of the weak beam with respect to the condensate. A beam whose cross section is much larger than that of the condensate, for example, would have photons that could never interact with the condensate, and these photons would only add to the shot-noise of the measurement and not to the signal. We tailor the spatial profile of the weak beam by focussing the weak beam onto the atoms, attempting to match the transverse spatial profile of the weak beam to that of the condensate in order to minimize the number of extra photons that will never contribute to the signal.

We can model this effect by taking the overlap integral between the BEC density profile and the gaussian profile of the weak beam to calculate the number of Bragg excitations expected on resonance. The overlap integral is calculated as

$$\int_0^\infty \int_{-\infty}^\infty \int_0^{2\pi} S(k) \frac{\pi}{2} \frac{\Omega_{\text{2-ph}}^2(\rho, z)\tau\sigma_{\text{Bragg}}^{-1}}{\sqrt{2\pi}} n_{\text{BEC}}(\rho, z)\rho \; d\rho \; dz \; d\phi \tag{4.20}$$

where

$$\Omega_{\text{2-ph}}(\rho, z) = \left(\frac{\Gamma^2}{4\Delta}\right)\left(\frac{\sqrt{I_{\text{strong}}(\rho, z) I_{\text{weak}}(\rho, z)}}{I'_{\text{sat}}}\right) \tag{4.21}$$

where Eq. 4.21 is the same as that given by Eq. 3.19, with I'_{sat} the saturation intensity scaled by the Clebsch-Gordan coefficients. The intensity of the weak beam as a function of ρ and z is given by

$I_{\text{weak}}(\rho, z)$ (similarly for the strong beam). The BEC density profile is given by $n_{\text{BEC}}(\rho, z)$, which we calculate in the Thomas-Fermi limit, as in Ref. [55], $S(k)$ the static structure factor calculated from Eq. 3.21 and σ_{Bragg} is the rms width of the Bragg lineshape, which for these calculations we assume to be dominated by Fourier broadening, as described by Eq. 3.25.

We find that for our ^{85}Rb condensates with a Thomas-Fermi radius of 13.5 μm, a 15 μm beam waist matches the spatial profile of the BEC quite well. In this thesis, we define the beam waist as the radius at which the intensity has dropped off to $1/e^2$ of its peak value. From this model we calculate that for a 1 ms long Bragg pulse, with the strong and weak beams intersecting at a 10.5° angle (corresponding to $S(k) = 0.8$) and 10^5 photons in the weak beam, we will excite 7×10^3 atoms out of 4×10^4 BEC atoms, when on resonance. This corresponds to a SNR of 10, with only 3% of the condensate scattered due to the strong beam, provided we are measuring 90% of the weak beam light.

Because a 15 μm beam waist is difficult to measure directly on a CCD camera due to the finite size of the pixels, we determine the beam waist with a simple knife-edge measurement, as shown in Fig. 4.4. This measurement is done by measuring the beam power on a photodiode as a

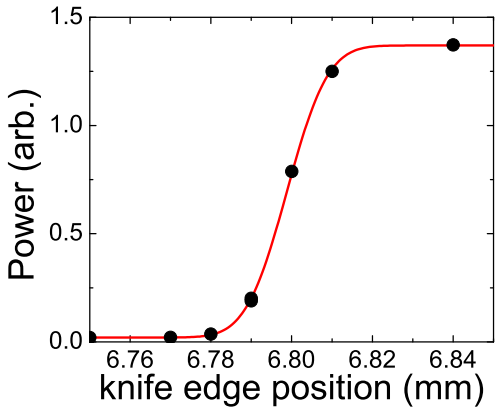

Figure 4.4: Typical knife-edge measurement to determine the weak beam waist. Plotted on the vertical axis is the light power incident on a photodiode versus the position of a razor blade (horizontal axis) as it is moved into the beam. The fitting method to determine the weak beam waist is described in the text. The data shown here corresponds to a beam waist of 16.0(3) μm.

function of the position of a razor blade which is perpendicular to the beam and is drawn across the beam. We record the fraction of light that makes it to the detector as a function of the position of the razor blade, which is mounted on a translation stage. From this, we determine the beam waist by fitting the data shown in Fig. 4.4 to a functional form laid out by de Araújo *et al.* [91]

$$P(x) = \frac{P_0}{1 + e^{a_1 s + a_3 s^3}} \tag{4.22}$$

where P_0 is the power in the beam and $s = 2(x - x_0)/\mathrm{w}_{\mathrm{weak}}$ is described by the beam waist $\mathrm{w}_{\mathrm{weak}}$, the position of the razor blade x, and the position of the center of the weak beam x_0. The coefficients $a_1 = 1.597106847$ and $a_3 = 7.0924013 \times 10^{-2}$ have been determined by de Araújo *et al.*

In minimizing the number of weak beam photons, it is possible to approach a regime where the number of Bragg photons scattered is a significant fraction of the weak beam photons themselves. In this regime, the transverse spatial profile of the weak beam intensity along the $\vec{k}$ direction has been modified due to the scatter of Bragg photons out of (or into) the weak beam, which can, in effect, burn a "hole" in the probe. We therefore keep the total number of photons in the region of overlap between the weak beam and the BEC cross-section large compared to the number of excitations.

4.3.5.1 Weak beam alignment

If aligning a 50 μm optical trap onto a relatively hot gas of atoms is akin to pulling teeth, then aligning a 15 μm beam onto a Bose condensed gas would be something more along the lines of pulling tonsils.[1] In order to control the position of the weak beam at the atoms in a precise way, we tilt a plate of glass that is mounted inside a telescope for the weak beam, as shown in Fig. 4.5. This design has the advantage of giving fine control of the weak beam position (50 μm at the atoms for every mm of micrometer displacement on the glass plate's mount) while also having no measurable hysteresis.

In Fig. 4.6 we show typical data used for alignment of the weak beam light to the trapped condensates. The alignment procedure is to essentially blast the atoms out of the trap with weak

[1] For a good reference on other "tonsil pulling endeavors" I refer the reader to Dr. Stutz' thesis [92]

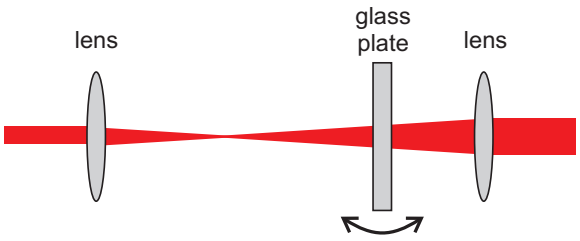

Figure 4.5: Glass plate placed in between the two lenses of a telescope for the weak beam. We precisely align the weak beam onto the BEC by changing the angle of the plate with respect to the weak beam. Because the weak beam will pass through a focussing lens just before the atoms (see Fig. 4.1), the beam *angle* with respect to the axis of the focussing lens must be changed in order to manipulate the weak beam position at the focus. For this reason we cannot place the glass plate outside the telescope, as its effect on a collimated beam would be to only *displace* it with respect to the focussing lens axis.

beam light that we shift to be on resonance as we vary the position of the weak beam with respect to the atoms. We then fit the log of the number of atoms remaining to an inverted gaussian, this is shown in red in the figure. We take the center of the gaussian lineshape as the best alignment. Typically, we use very pure ^{85}Rb condensates for this procedure, with the rf ^{85}Rb evaporation knife

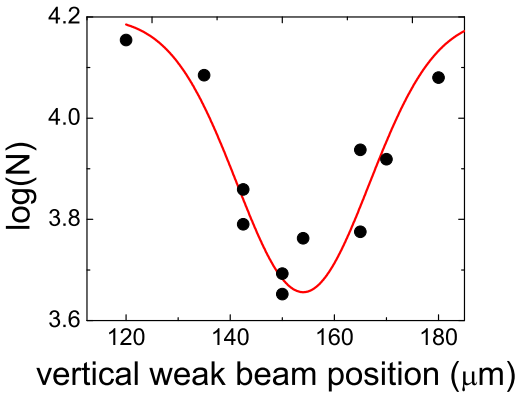

Figure 4.6: Typical number loss data used to align the weak beam onto the condensate. On the vertical axis, we plot the log of the number of BEC atoms, and on the horizontal axis we plot the position of the weak beam near the condensate. We should mention that the rms width of this feature does not predict the correct weak beam waist ($w_{\mathrm{weak}} = 2\sigma_{\mathrm{RMS}}$), but instead predicts a waist that is roughly 3 times larger than measured with the knife-edge for this data. This could be attributed to saturation effects of the high OD condensate on the 10 μs resonant blast light.

on for both the 10 μs blast pulse as well during 500 ms hold time in the trap after the blast. This 500 ms hold is meant to enhance the effect of the light on the measured loss, allowing for more rethermalization and giving the rf knife a chance to remove more atoms from the heated cloud.

4.3.6 RF

We also take steps to minimize the electronic noise (δ_e) that the LO's shot-noise must overcome. The relevant noise for the heterodyne setup is at the frequency of the beat note, $\Delta\omega$. Our photodiode circuit is designed to minimize the noise at this frequency ($2\pi \times 70$ MHz) by way of a standard "tank" circuit (an inductor that gives signals at $\Delta\omega$ a high impedance path to ground), shown in Fig. 4.7. We are able to reduce the receiver dark noise (dark noise from both the photodiode as well as the amplifier) to 2 pA/$\sqrt{\text{Hz}}$, which is the limit of today's state of the art transimpedance amplifiers.[2] The subsequent stages of amplification are chosen so that the noise they add is small compared to this noise.

The voltage from the photodetector then goes to an rf mixer. As shown in Fig. 4.1, the mixer is a four-terminal device, called an I,Q-Demodulator; this is essentially two mixers in one, with the rf input split between the two. Port I is the same as the IF output of a standard mixer, while the Q port is the output of a second mixer whose "LO" drive has a phase offset 90 degrees with respect to the phase of the I port's "LO" drive. In our application, the outputs of the demodulator have the form

$$S_I = 2CRe\eta\sqrt{\frac{N_{\text{LO}}}{\tau}\frac{N_{\text{weak}}}{\tau}}\cos\phi \tag{4.23}$$

$$S_Q = 2CRe\eta\sqrt{\frac{N_{\text{LO}}}{\tau}\frac{N_{\text{weak}}}{\tau}}\sin\phi \tag{4.24}$$

By summing the squares of S_I and S_Q, we are able to measure the amplitude of the beat signal, regardless of the relative phase ϕ. For a known LO beam power, $\propto N_{\text{LO}}/\tau$, our signal is directly proportional to the rate of weak beam photons, $\dot{n} = N_{\text{weak}}/\tau$. We measure S_I and S_Q with a digitizing oscilloscope and perform the sum in subsequent software analysis. We now have the

[2] For our photodetector, we use a Philips SA5211 Transimpedance amplifier. These transimpedance amplifiers are commonly used in the telecom industry to do exactly this: amplify a photocurrent at high BW with low-noise.

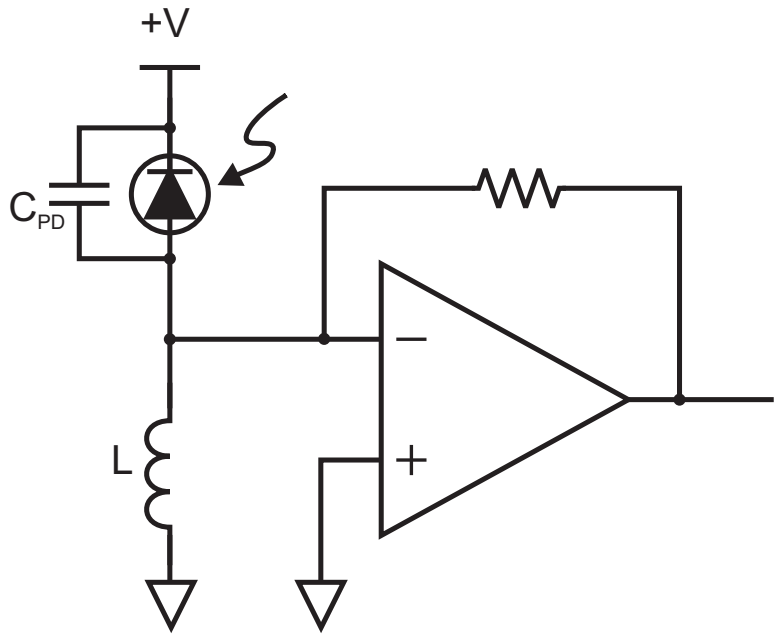

Figure 4.7: Tank circuit to minimizing the electronic noise of the photodiode circuit. The motivation is to reduce the voltage noise's (v_n) contribution to the electronic noise δ_e, leaving the current noise (i_n) as the dominant electronic noise source. The principle behind the tank circuit is that in choosing an appropriate inductor value, L, for a given internal capacitance of the photodiode ($\mathrm{C_{PD}}$), one can have a resonant LC circuit at $\omega_{\mathrm{res}} = 1/\sqrt{\mathrm{LC_{PD}}}$. The impedance of a parallel (both ground and +V offer zero impedance to an AC signal) LC circuit is given by $Z = -j\omega \mathrm{L}/(\omega^2 \mathrm{LC_{PD}} - 1)$, which, at $\omega = \omega_{\mathrm{res}}$ is infinity. In reality there are stray resistances that keep you from infinite impedance, by broadening the Q of the circuit. However, this high impedance $Z(\omega_{\mathrm{res}})$ does limit the contribution of the voltage noise, as $\delta_e = i_n + v_n/Z(\omega_{\mathrm{res}})$. We have verified that the electronic noise of our receiver is at the current noise limit for our transimpedance amplifier.

following expression for the total measured photon number in the weak beam

$$N_{\text{weak}} = (S_I^2 + S_Q^2)(\frac{\tau}{2CRe\eta})^2/N_{\text{LO}} \tag{4.25}$$

While, in principle, we now have a signal that is insensitive to the relative phase ϕ between the weak beam and the LO beam, the demodulator is imperfect, with non-linearities and voltage offsets in the I and Q outputs as well as deviations from the 90 degree phase offset applied to the LO drive. We therefore servo the phase of the rf driving the LO port of the demodulator, as illustrated in Fig. 4.1. The servo minimizes S_I by actively feeding back to the phase-modulation input of the demodulator's synthesizer (which is phase-locked to the other synthesizers used in the Bragg setup). This makes the quadrature sum less sensitive to demodulation imperfections.

4.4 Calibration and performance

As we mentioned previously, the overall calibration of the transimpedance gain of our system is calculated from Eq. 4.13. To do this, we measure the voltage noise δ_s, which is just the standard deviation of the voltage from one of the quadratures, at different LO powers. The LO powers are measured using a power meter. We plot the results of these measurements in Fig. 4.8. In this figure, we have calculated what we would expect for the LO photon shot noise (in W of optical power) using $(hc/\lambda)(1/\tau)\sqrt{N_{LO}} = \sqrt{P_{LO}hc/\tau\lambda}$ for the particular pulse length τ, and LO power P_{LO}. The slope, β of the linear fit to δ_s versus $\sqrt{P_{LO}hc/\tau\lambda}$ is $\beta = \sqrt{\eta}(e\lambda/hc)R$, with units of V/W directly giving the experimenter a useful conversion ($P_{\text{weak}} = \frac{S_I^2+S-Q^2}{\eta C^2(2\beta)^2}$) as well as the transimpedance gain of our system. In measuring δ_s, one must be careful that the noise is completely dominated by the shot noise of the LO photons. We therefore disregard noise data that is too close to the noise floor of the receiver (which is easily measured by turning off the LO light). We also disregard noise data taken at too high a bandwidth, where an inline low-pass AC filter would suppress fluctuations of the voltage above a certain bandwidth, thereby smoothing over the noise.

In Fig. 4.9, we present data illustrating the shot-noise limited performance of our heterodyne detection. We measure noise by taking the standard deviation σ in the measured weak beam photon

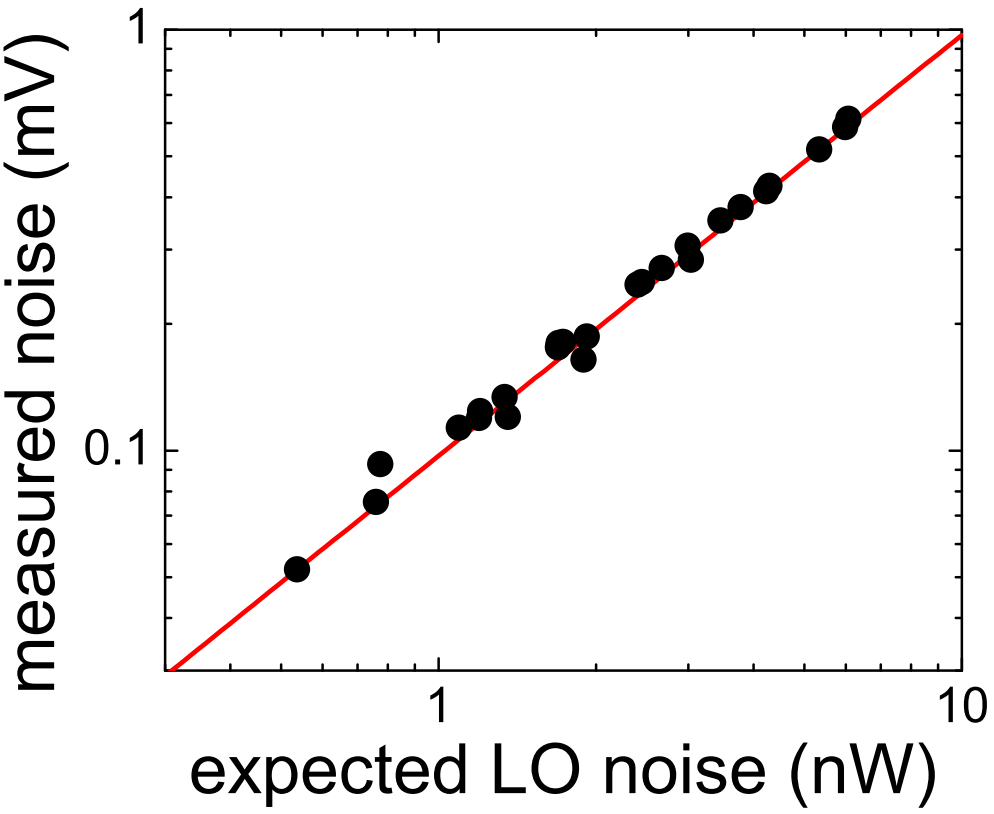

Figure 4.8: Typical calibration data used to determine R, the overall gain of our heterodyne system. On the vertical axis is the electronic noise, which we know to be dominated by the photocurrent shot-noise associated with the LO light. On the horizontal axis we plot the expected LO photon shot noise in terms of optical power (nW). The slope of this data, β has units of V/W, conveniently giving one a useful calibration for the system. In addition, one can determine $R = \frac{hc/\lambda}{e\sqrt{\eta}}\beta$ from this slope. For this calibration we varied the LO power between 100 μW and 720 μW, with τ ranging from 5 μs to 100 μs to give us a slope of 97,200(400) V/W, which corresponds to a gain of $R = 165.6(7)$ kΩ.

number for M consecutive pulses of equal length,

$$\sigma = \frac{1}{\sqrt{2}} \sum_{i=1}^{M-1} \sqrt{\frac{\left(N_{\mathrm{weak}_{i+1}} - N_{\mathrm{weak}_i}\right)^2}{M-1}} \tag{4.26}$$

where N_{weak_i} is the measured number of photons in the weak beam for pulse i. We plot the noise on our measurements of weak beam photon number, normalized to the expected shot-noise ($\delta_{\mathrm{shot}} = \sqrt{\eta N_{\mathrm{weak}}}$) for that particular pulse duration and laser power, as a function of the duration of a fixed intensity pulse. In the inset of the figure, we plot the same noise measurement for the case where the weak beam intensity is varied to keep the total number of photons fixed at a constant 10^5.

For a large range of pulse durations, the measurement is at, or within a factor of two of, the shot-noise limit. For pulses shorter than 1 μs the noise is artificially low due to an inline, low-pass filter. The increased noise at longer timescales sets an upper limit to the time available for our Bragg measurements and is probably caused by residual phase drift in our system. Servoing the laser power provided no significant improvement in the noise performance of our heterodyne detection.

4.5 Bragg experiments with photon counting

In Fig. 4.10, we show an example of a measured Bragg lineshape for a weakly interacting ^{85}Rb BEC. This data both demonstrates the viability of the photon-counting technique, as well as tests it against the benchmark of Bragg spectroscopy measurements: ToF imaging. On the horizontal axis, we have the frequency difference between the two Bragg beams, which sets the energy of the Bragg excitation. On the vertical axis, we have the Bragg signal, which is the number of excitations due to the Bragg process. We define this signal such that it can be either positive or negative, reflecting the direction of the momentum transfer. The number of excitations due to the Bragg pulse are counted in two different ways, and one can see that the photon counting and the time-of-flight imaging signals agree well with each other. The two sets of data were acquired simultaneously, with each cycle of the experiment providing both a photon-counting and an atom-

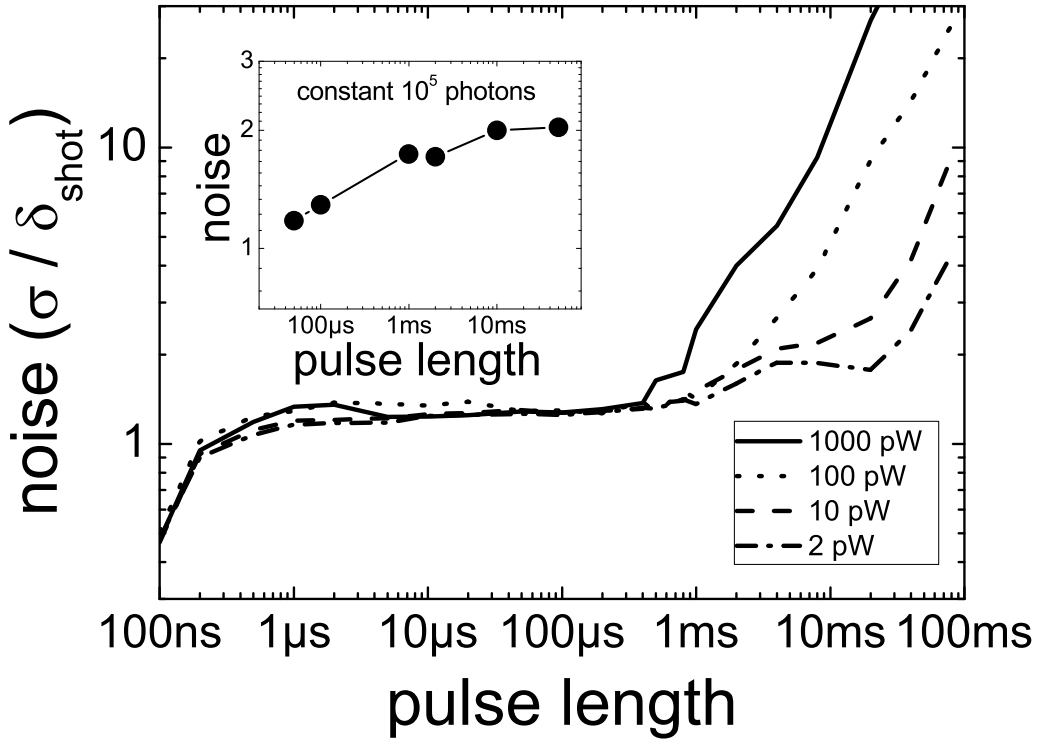

Figure 4.9: Noise performance of heterodyne detection for a LO power of 250 μW. The vertical scale is normalized to the shot-noise expected for the relevant pulse length and laser power detected. The legend shows the different weak beam powers used. At long time scales, our heterodyne scheme is no longer shot-noise limited, presumably due to the phase fluctuations between the LO and weak beams. The inset has the same normalized vertical scale, and shows data at different weak beam intensities that correspond to a fixed 100,000 photons. The inset is more relevant experimentally, as we typically try to keep the same ratio of Bragg excitations (fixed by the condensate atom number) to N_{weak} constant.

imaging data point, demonstrating the complementary nature of the two techniques. The lines in Fig. 4.10 are individual fits of the Bragg spectrum to two Gaussian functions. These fits can be used to extract a center frequency and an rms line width.

A potentially useful feature of a photon-counting measurement is the ability to measure the dynamics of Bragg excitations during a single laser pulse. We demonstrate this capability in Fig. 4.11, where we plot the number of excitations, $N_{\rm exc}$, as a function of time, τ. The data were taken using a condensate of 400,000 ^{87}Rb atoms, with the Bragg detuning set to be on resonance with the measured Bragg transition at $\omega = 2\pi \times 250$ Hz for a momentum transfer given by $k = 1.5\ \mu\text{m}^{-1}$. We expect $N_{\rm exc}$ to go as τ^2, however an interesting feature illustrated in Fig. 4.11 is the suppression of signal for pulses short compared to the inverse Bragg resonance, $\tau < \omega^{-1} = 0.3$ ms. For these short pulses, the associated energy uncertainty makes it impossible to resolve a $+k$ excitation from a $-k$ excitation. Photon emission from the one process cancels photon absorption from the other process. In our experiments, we did not observe Rabi flopping in the time-dependent data, which may be due to dephasing. For the measurements here, the weak beam profile used here was much smaller (7 μm $1/e^2$ waist) than that of the BEC (22 μm Thomas-Fermi radius), which complicates the Bragg response. We present this data, however, to illustrate a promising feature: the ability to resolve excitations in time within a single Bragg pulse. This feature is unavailable to the experimenter with traditional TOF imaging.

We have also observed asymmetries in the strength of the positive and negative frequency features of the Bragg lineshapes. We attribute this to the relatively small number of $N_{\rm weak}$ photons necessitated by the photon counting approach. A typical asymmetric lineshape is shown in Fig. 4.12. This effect was observed both using photon counting as well as traditional time-of-flight imaging to measure the Bragg excitation. We think that these asymmetries are related to the propagation effects (the aforementioned "hole burning") inherent when the number of Bragg photons is a significant fraction of $N_{\rm weak}$, although we have not been able to experimentally confirm this. The shape of the asymmetries, with the larger peak on the side where the weak Bragg beam is enhanced by Bragg photons, does support the idea of propagation effects being the culprit.

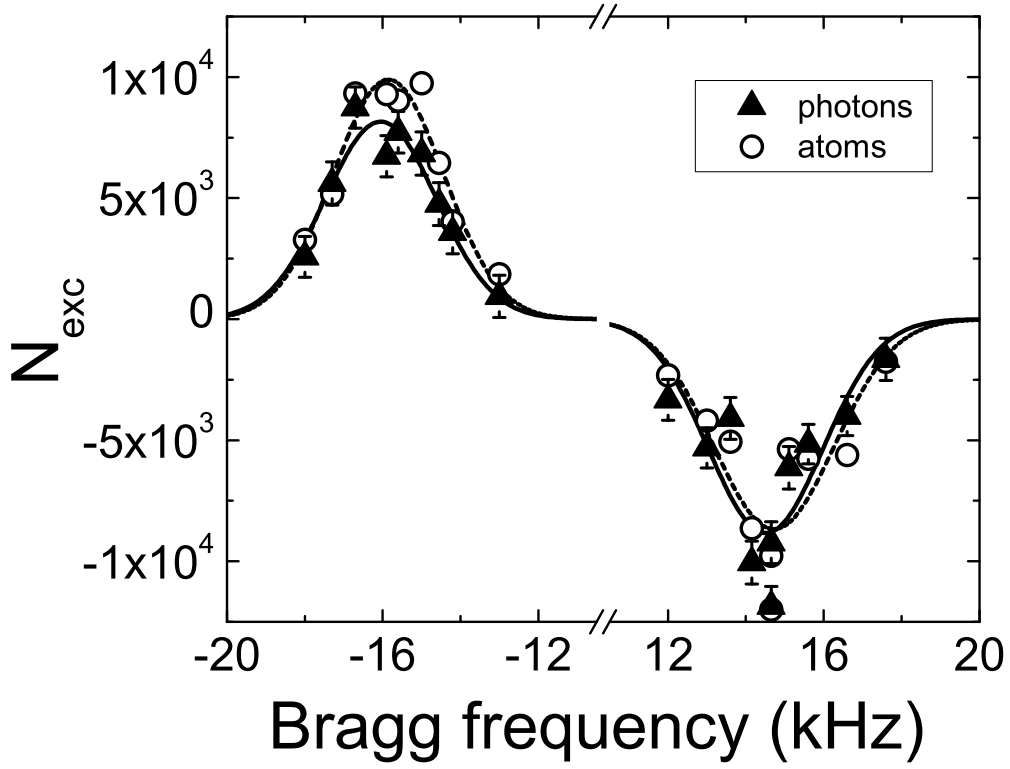

Figure 4.10: Bragg spectrum of a weakly interacting ^{85}Rb BEC of 5.5×10^4 atoms at k = 16 μm^{-1}, measured in two different ways. The horizontal axis shows the frequency difference between the Bragg beams. The vertical scale is the number of excitations measured using either traditional absorption imaging of ejected atoms (hollow circles), or the photon counting technique presented here (black triangles). Error bars on black points represent the shot-noise in the photon counting measurements. The photon counting measurements used three pulses of equal length. The first and the third pulses used only a single weak beam to make an average background measurement, with no Bragg excitation. During the second pulse, both Bragg beams illuminate the condensate to induce Bragg scattering and we subtract the averaged background to count the number of photons gained or lost in the weak beam due to the Bragg excitation.

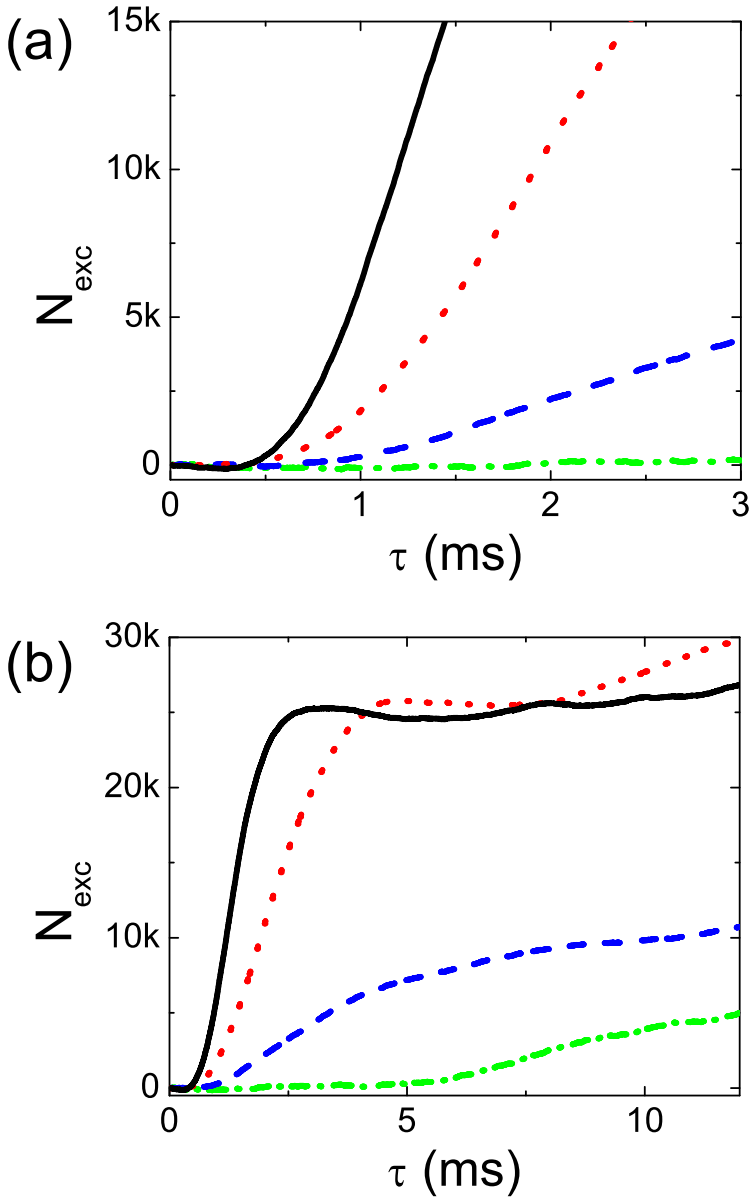

Figure 4.11: Integrated Bragg excitations measured with photon counting, as a function of time. Different colors correspond to the different drive amplitudes. The number of Bragg excitations is given by $N_{\rm exc} = \int_0^\tau (\dot{n}(t) - \dot{n}_{\rm avg})dt$, where $\dot{n}_{\rm avg}$ is the average rate of weak beam photons measured when no strong light is present. The Bragg beams are turned on at 0 ms, beginning the Bragg excitation process. Experiments are performed on resonance, for a BEC of 400,000 ^{87}Rb atoms. The two plots (a) and (b) correspond to the same data, plotted on different scales.

4.6 Outlook

We have demonstrated photon counting as a viable technique for Bragg spectroscopy in ultracold atoms. By measuring the response of the driving field to the atoms, one has a measurement independent of the traditional time-of-flight imaging of the atom cloud. Our heterodyne scheme achieves shot-noise limited detection and allows us to measure the number of photons added to, or depleted from, one of the Bragg beams.

Photon counting for Bragg spectroscopy is not without its own unique complications, however. Because the weak Bragg beam profile is roughly matched to the transverse profile of the condensate, careful alignment must be maintained for the photon counting approach. Also, this method is inherently a measure of the *net* effect on the probe. This is problematic for small momentum transfers, where the positive and negative frequency features of the lineshapes seen in Fig. 4.10 begin to merge for Bragg frequencies near zero. This complicates the analysis as described in the previous chapter. Ultimately, for this approach to be successful, I believe that investigations of photon counting would have to be at slightly larger momentum transfers where these effects are less important. In this regime, the technique could be investigated and characterized, and later extended to small k.

Still, this technique could find more success in systems whose atom number is large compared to the 40,000 we employ in our ^{85}Rb BECs. Furthermore, measurements of the scattered Bragg photons could open the door to new investigations of the temperature dependent structure factor, as proposed by Stamper-Kurn *et al.* [70]. This technique of measuring the probe in order to detect atom-light interactions could be applied to other types of ultracold atom spectroscopy as well [93], and it seems that the two technologies, photon counting and time-of-flight imaging, marry nicely.

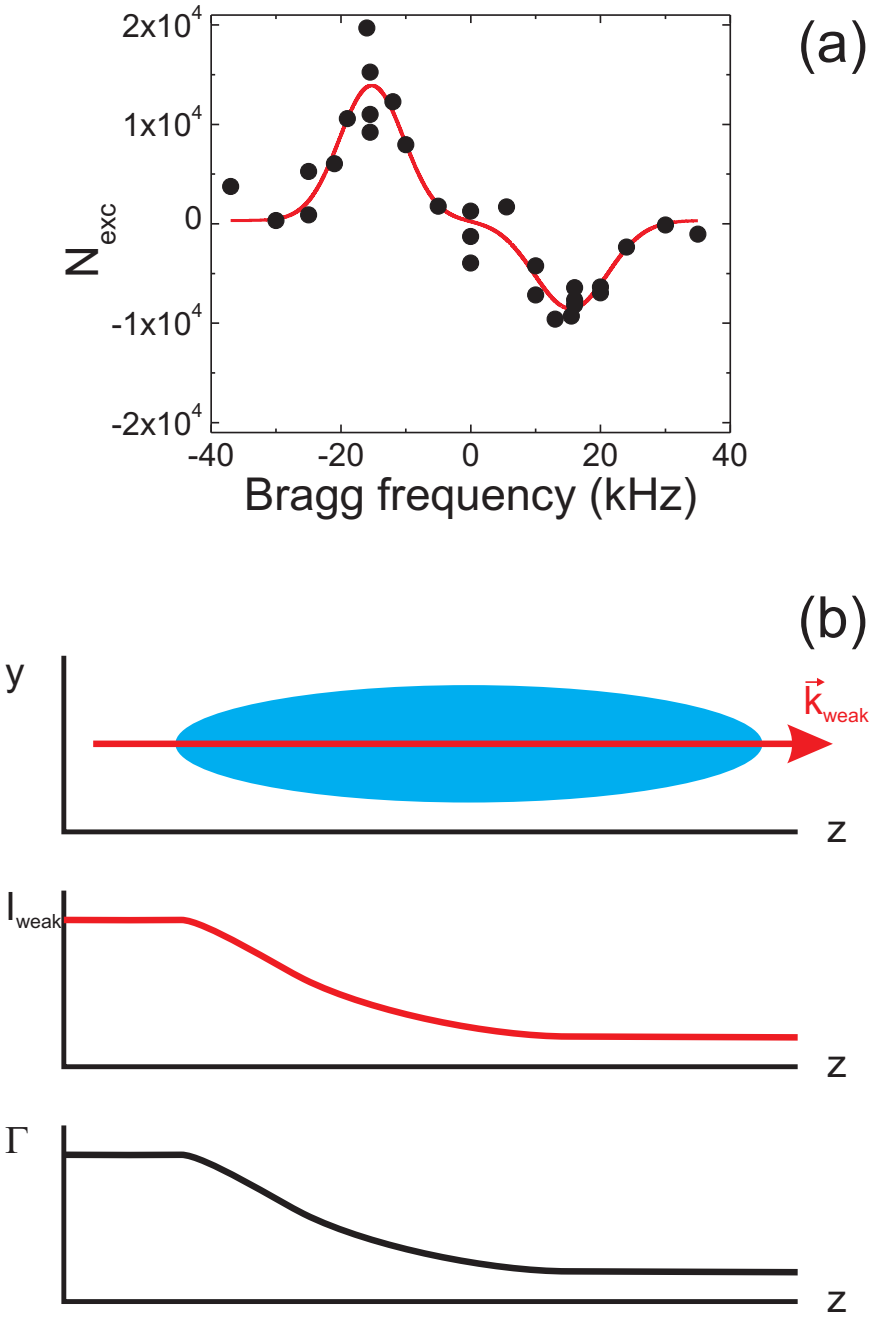

Figure 4.12: (a) Example of an asymmetric lineshape. Here the excitations were measured using the photon counting technique, but traditional time-of-flight imaging of Bragg excitations gave results consistent with the photon counting data. The peak corresponding to "extra" weak beam photons (here the one at -18 kHz) is larger in amplitude than the peak corresponding to depletion of the weak beam. For this reason, we speculate that this could be due to depletion of the weak beam. In (b) we illustrate the concept of depletion. For the case where the Bragg photons are large in number compared to the weak beam photons we see the weak beam being attenuated as it passes through the condensate. This, in turn, lowers the Bragg response of the weak beam, resulting in the smaller amplitude peak for the Bragg resonance corresponding to absorption of weak beam photons during the Bragg process. Attempts to quantify this effect, however, have so far been unsuccessful, as strong beam scatter makes studies in these regimes difficult.

Chapter 5

Contact spectroscopy

In this chapter I present the concept of the contact interaction and its usefulness in probing strongly interacting BEC. We will see that the contact connects the microscopic physics of short-range, two-body interactions to macroscopic, thermodynamic quantities in the system. Using rf we have made preliminary measurements verifying the existence of the contact interaction in a BEC. We observe both a dependance on a and see evidence of the high-momentum states that we are probing, in line with the predictions for a contact in a BEC.

The technique of contact spectroscopy looks promising in measuring the LHY correction to the energy of a BEC, something which to date has only been accomplished with extremely weakly bound dimers made of fermionic atoms [94]. Remarkably, this measurement matches the LHY prediction, even though the composite bosons in these systems are clearly not the hard spheres or point-like bosons described by the LHY theory. These intriguing results from strongly interacting fermionic atom gases highlight the need for a measurement of the LHY correction in a dilute gas of bosonic atoms, where one can directly test the LHY theory.

5.1 Making contact with an interacting BEC

Since the first chapter of this thesis, we have argued that the two-body interactions described by the scattering length a dominate the microscopic and macroscopic behavior that has been observed in BEC. In this chapter, we present the contact, a quantity that directly relates the two-body physics of s-wave scattering to bulk thermodynamic quantities. This is a universal result that

works in the context of Fermi gases as well, as it is only concerned with two-body physics.

One such way that the two-body interaction manifests itself in other physical characteristics of the interacting gas is through the momentum distribution, $n(k)$. For a certain range of momentum, all gases with two-body interactions will exhibit the same characteristic $1/k^4$ momentum distribution (this can be seen by taking the Fourier transform of the two-body scattering wavefunction). The contact quantifies the strength of this $1/k^4$ momentum tail for the particular gas in question, given by

$$\lim_{1/r_0 \,>\, k \,>\, n^{1/3}} n(k) = C/k^4 \tag{5.1}$$

where C is the contact (also referred to as the contact interaction), with units of length^{-1}. Note that the contact is an *extensive* parameter of the system, and for this reason we will often times normalize the contact to the total number of particles in the gas and write the contact per particle C/N.

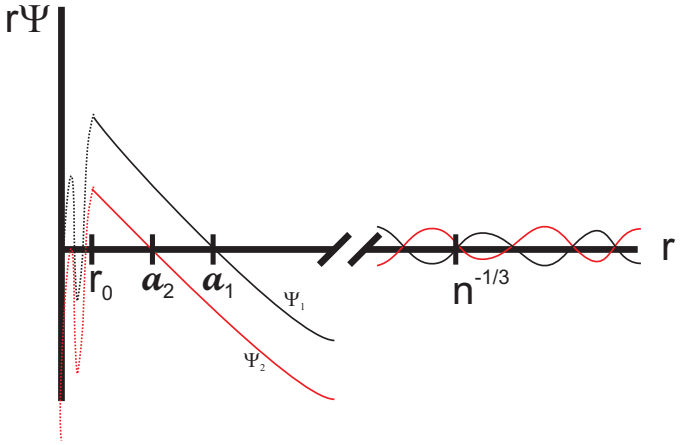

Figure 5.1: Two scattering wavefunctions (the Fourier transforms of which give $n(k)$) at different a, illustrating the limits of the contact interaction. For $r < r_0$, details of the interatomic potential cannot be ignored, setting a lower (upper) limit on r (k). For $r \sim n^{-1/3}$ the two wavefunctions are quite similar, as far as the Fourier transform is concerned, and can hence also be disregarded when considering the projection to the $1/k^4$ tail, setting an upper (lower) limit on r (k).

We can understand the limits in which Eq. refeq:5n2body is valid, $1/r_0$ and $n^{1/3}$, by considering the associated lengthscales. In Fig. 5.1 we present two scattering wavefunctions, each with its own scattering length, a_1, a_2. The lower limit of Eq. 5.1 (in terms of lengthscales) is set by the

effective range of the interaction, r_0. This is the lengthscale where the wavefunction can no longer be described by one simple scattering parameter a, and the details of the interatomic potential must be taken into account. For ^{85}Rb this is roughly 80 a_0 [95]. Because these short-range potentials are particular to each species, one does not expect a universal result (such as the $1/k^4$ tail) in this regime. We therefore ignore the curvature in the wavefunction for $r < r_0$ when we take the Fourier transform. Hence an $n(k) \sim 1/k^4$ must only be only valid for $k < r_0^{-1}$.

The other limit is set by the interparticle spacing $n^{-1/3}$. Notice in Fig. 5.1 that at such large distances there is only a subtle difference, essentially a phase shift, between ψ_1 and ψ_2. When taking the Fourier transform of this wavefunction, this subtlety is washed away and the $1/k^4$ tail is insensitive to changes in a at these large lengthscales (small k scales). In reality, the *actual* wavefunction (as opposed to the simplified picture of the scattering wavefunction) will be modified by the presence of other particles at distances $n^{-1/3}$, so that $n(k) \sim 1/k^4$ is unphysical for $k < n^{-1/3}$.

What is left is a parameter a that characterizes a universal feature seen in all gases, the $1/k^4$ tail. It would turn out that a will characterize a great number of macroscopic parameters, all of which can be related through C [96, 97, 98]. While the universal relations connecting C to these macroscopic parameters have been developed and tested in the context of Fermi gases [99, 100, 101, 102, 103, 104, 105], we know that the contact interaction is two-body. Because of this, the derivation of these universal relations also does not depend on the particle statistics and can therefore be generalized to our ^{85}Rb Bose gases as well [106]. We use these ideas as a measurement tool of the LHY correction.

One of these universal relations connects the contact of a gas to its energy through what is called the adiabatic sweep theorem [97]

$$\frac{dE}{da} = \frac{\hbar^2}{8\pi m a^2} C_{\mathrm{BEC}} \tag{5.2}$$

where E is the total energy of the gas. We write C_{BEC} here to alert the reader that this universal relation differs by a factor of two from the one considered by Tan [97] due to our Bose gas being

completely spin-polarized [107]. Combining this, with the LHY result (Eq. 1.3), yields the predicted contact for a condensate

$$\frac{C_{\mathrm{BEC}}}{N_{\mathrm{BEC}}} = 16\pi^2 n a^2 \left(1 + \frac{5}{2}\frac{128}{15\sqrt{\pi}}\sqrt{na^3} + \ldots\right) \tag{5.3}$$

where N_{BEC} is the condensate atom number. Notice that the LHY term is a 5/2 bigger correction for the contact interaction compared to the energy density (Eq. 1.3). This is because the adiabatic sweep theorem (to which the contact is proportional) does not address the energy directly, but instead tells us *how* the energy directly changes with a. This important distinction makes the contact a powerful tool for probing beyond-mean field physics, allowing us to probe large corrections to the contact at smaller values of na^3 than would be necessary if resolving the energy directly. This is an important consideration since we must always fight timescales associated with three-body recombination.

5.2 How rf spectroscopy connects

Spectroscopy in the radio domain has been a highly successful probe in the cold atom community, and has helped to unwrap the physics of the Feshbach resonance upon which this thesis is built [46]. For a more detailed discussion of rf spectroscopy and its usefulness I refer the reader to Dr. Stewart's thesis [108]. One might hope that it would again be a useful frequency domain for spectroscopy of strongly interacting condensates, falling somewhere between the success of the optical domain (the aforementioned Bragg spectroscopy), and the failures inherent in the spectroscopy of breathing modes (being too slow with respect to three-body loss). The problem with rf spectroscopy as a direct probe of interacting condensates, however, is due to the nature of the energy splitting between the states. With rf we probe a transition between different magnetic Zeeman sublevels. If we intend to use rf to directly resolve the interaction energies of a BEC (a few 100 of Hz) we must then be comfortably above the noise associated with this energy splitting: magnetic field noise. In our system, this noise is on the order of 5 mG or 30 ppm of our total field. In terms of the actual energy splitting, this corresponds to 4 kHz, which is 10 times larger than the

energy we are trying to resolve. If our goal is more bold, say resolving an LHY correction of 30%, the prospects of directly probing the energy with rf spectroscopy is even more bleak.

What the contact, and Tan's relations, allows for is a way to use rf to probe the energy, or more accurately dE/da, with rf that is detuned from the splitting associated with the Zeeman states. An extension of Tan's universal relations asserts that the $1/k^4$ tail gives rise to a tail in the rf lineshape that goes as $1/\omega^{3/2}$ for large detunings [109, 110], which was later verified [105]. Being able to work at such large detunings, where one is tasked with measuring the strength of our signal (rather than the resonance of our signal), makes our magnetic field noise tolerable.

5.2.1 Final-state effects

In our experiments, the rf transfers a small fraction of the spin-polarized atoms from the $|F = 2, m_F = -2\rangle$ state into the $|F = 2, m_F = -1\rangle$ state, which we refer to as the final state. We modify Braaten's result [111] for a gas with two spin states to take into account the fact that our gas is spin polarized and write

$$\lim_{\omega\to\infty} S(\omega) = \frac{\eta}{8\pi}\frac{\tau\Omega^2}{\omega^{3/2}}\frac{\alpha(a)}{\beta(\omega)}\sqrt{\frac{\hbar}{m}}C, \tag{5.4}$$

where

$$\int_{-\infty}^{\infty} S(\omega)d\omega = \eta\frac{\pi}{2}\tau\Omega^2 N. \tag{5.5}$$

Here τ is the rf pulse duration, Ω is the Rabi frequency, and N is the total number of atoms in our system. The imaging efficiency, η, will be discussed later in more detail. Despite the fact that Eq. 5.4 and Eq. 5.5 differ from Braaten's result by a factor of two, the *ratio* of the two formulas is the same in both cases. This is important because we will later be using Eq. 5.5 to normalize Eq. 5.4. In Eq. 5.4, the final-state corrections are encompassed in $\alpha(a) = (a'/a - 1)^2$, and $\beta(\omega) = 1+\hbar\omega/E'$, where $E' = \hbar^2/ma'^2$. These final state corrections are due to interactions between atoms in the final spin state and atoms in the initial spin state, and are characterized by an interspecies scattering length $a' = -565a_0$ for our system [112], a_0 being the Bohr radius.

5.3 Contact spectroscopy experiments

Our experiments probe 4×10^4 Bose-condensed ^{85}Rb atoms in a gas with a 60% condensate fraction. During the final stages of evaporation, the field is set to give a scattering length of 130 a_0, and the calculated averaged number density is 5×10^{12} cm^{-3}. After evaporation, we ramp the bias field in order to change a on a timescale that is fast compared to the trap period, but adiabatic with respect to $\hbar/ma^2$ ($\dot{a}/a < 0.01\hbar/ma^2$, $\dot{a}$ being the time derivative of a). To minimize magnetic-field gradients to less than 5 G/cm, we leave the atoms trapped but change the center position of the vertical confining potential.

An example of rf contact spectroscopy is shown in Fig. 5.2(a). We probe the condensate roughly 1 ms after the magnetic-field ramps using an rf pulse to drive the $|F = 2, m_F = -2\rangle$ to $|F = 2, m_F = -1\rangle$ transition, and our signal $S'(\omega) = S/\frac{\pi}{2}\tau\Omega^2 N$ (black circles) is the number of atoms transferred to the final spin state (S), normalized for the different pulse lengths and powers. The rf pulses are amplitude modulated to a Gaussian envelope and we selectively image final state atoms by ARPing them to an imaging, $|3, 0\rangle$ state, where our probe laser is far detuned from the atomic transition for atoms in the BEC. We fit $S'(\omega)$ to a Gaussian lineshape, also shown (black line in Fig. 5.2(a)). The center of this fit is taken to be the bare Zeeman splitting (ω_0). For small detunings, we use short pulses, with an rms width of 25 μs. At large detunings, we increase the weak signal by using pulses with a 200 μs rms width and 100 times more rf power. We outcouple at most 10% of the condensate and check that the signal depends linearly on $\tau\Omega^2$. We correct the signal for a small measured nonlinearity due to saturation effects, at the level of 10% for the tail and 7% for the main lineshape. For large negative detunings, we observe the expected $1/\omega^{3/2}$ tail (see inset of Fig. 5.2(a), with the Fourier-limited lineshape in black for reference). Because the rf drives stimulated emission to a lower energy final state, the interaction-induced $1/\omega^{3/2}$ tail is on the low frequency side of the rf resonance. At large positive detuning (see Fig. 5.3), we find that the signal is consistent with zero.

Shown in Fig. 5.2(b) is the spatial size of the outcoupled atom cloud in time-of-flight ex-

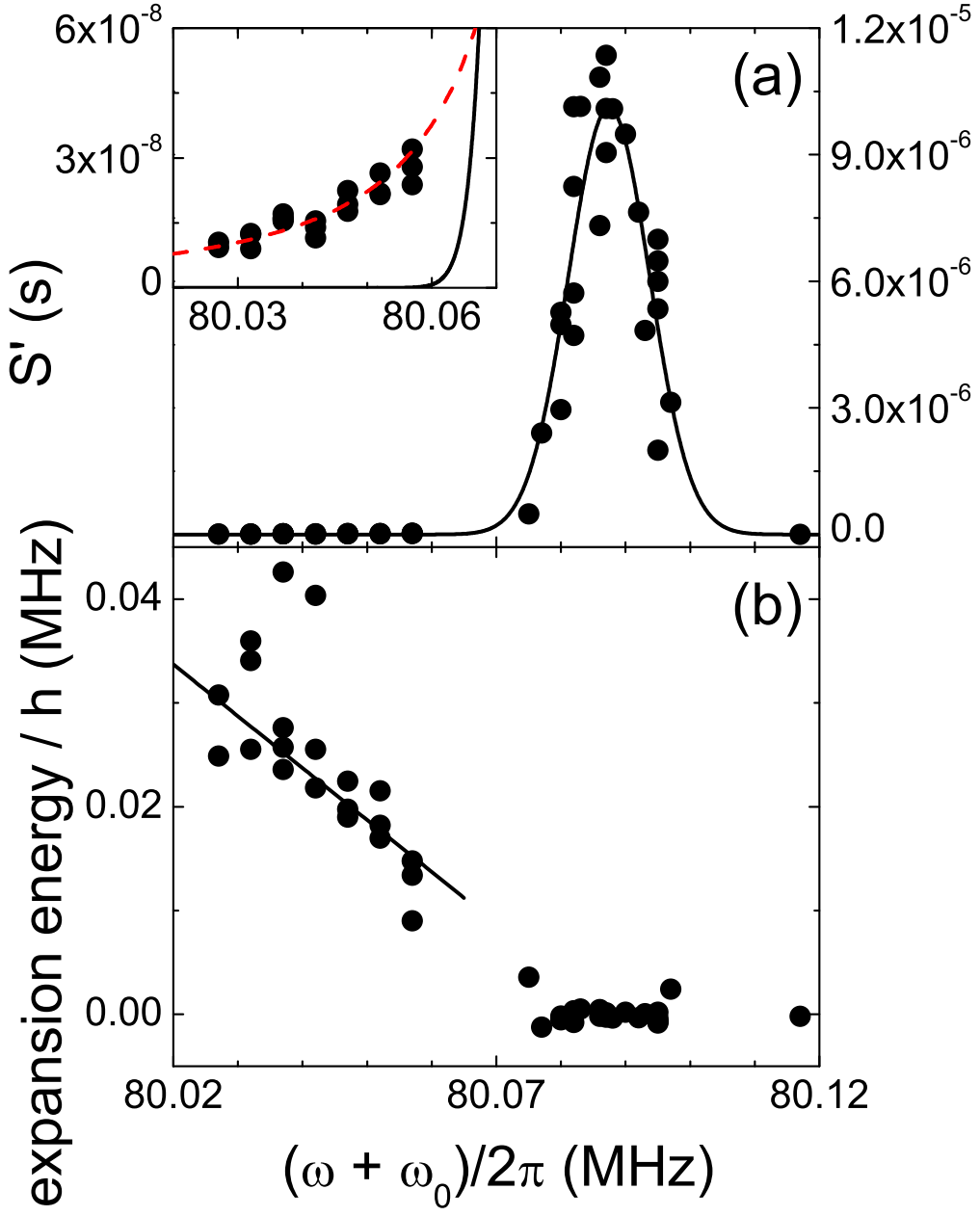

Figure 5.2: Example of rf contact spectroscopy. (a) Normalized number of outcoupled atoms, $S'(\omega) = S(\omega)/\int_{-\infty}^{\infty} S(\omega)d\omega$. We fit to a Gaussian lineshape (black line) and take the center to be the single atom resonance ω_0. In the inset, we show the $1/\omega^{3/2}$ tail at large negative detuning, where the signal is much larger than would be expected from the Gaussian fit (black line). The red dashed line is a fit of Eq. 5 to the $1/\omega^{3/2}$ tail. (b) Kinetic energy ($K.E.$) of outcoupled atom cloud, in units of MHz, measured in expansion. We calculate the energy from the width of the outcoupled atom cloud (σ), assuming $K.E. = \frac{3}{2}mv_{kick}^2/h$, where $v_{kick} = \sqrt{\sigma^2 - \sigma_0^2}/T$. Here σ_0 is the inherent width of the expanded cloud, measured on resonance, and T is the time between the rf pulse and the absorption image (4.5 ms). We use T instead of the expansion time because our rf couples the atoms into a less trapped state, and the subsequent ARP puts them in an untrapped state, expanding freely before we have turned off the magnetic confinement. In black we plot a prediction for the expansion energy divided by h, $-\frac{1}{2}(\omega - \omega_0)/2\pi$. We predict that the expansion energy should goes as $\frac{1}{2}\hbar\omega$, since the extra energy from the rf photon is split between two particles, owing to the pair-wise contact interaction. Our data shows good agreement with this prediction.

pansion. In the region of the $1/\omega^{3/2}$ tail, the expanded cloud size increases monotonically with increasing $|\omega|$. This is expected as larger $|\omega|$ outcouples atoms from further out into the $1/k^4$ tail in the momentum distribution. Notice that the data agrees well with the prediction (black line) described in the figure caption.

To extract the contact from our data, we plot the $1/\omega^{3/2}$ tail of $S(\omega)$ multiplied by $\omega^{3/2}$, as shown in Fig. 5.3. We fit this to $B/\beta(\omega)$, where $B = S(\omega)\beta(\omega)\omega^{3/2}$, at large $|\omega|$. For our fits we only consider detunings between $2\pi \times 30$ kHz and $2\pi \times 100$ kHz, which is well outside the Fourier-limited central lineshape that has an rms width of $1/25$ μs$= 2\pi \times 6$ kHz. The main effect of the $\beta(\omega)$ final-state correction is to suppress the tail. We illustrate this by plotting what we would expect, given the fit, had $\beta(\omega) = 1$ in the blue dashed line of Fig. 5.3. There also exists a minimal frequency dependence of $\beta(\omega)$ for our range of detunings.

We present preliminary results of our measurements of the contact in an interacting BEC in Fig. 5.4. On the vertical axis, we show the contact per particle $\mathcal{C} = C/N_{BEC}$, normalized to the average density of our cloud, with units of μm^2. We normalize the contact per particle to the average density to easily compare data taken at slightly different densities, as Eq. 5.3 shows us the linear dependence of C/N_{BEC} on n. On the horizontal axis, we show both the scattering length on the bottom, and, for reference, the LHY correction to the energy density, $\frac{128}{15\sqrt{\pi}}\sqrt{na^3}$, on the top. The Rabi frequency Ω is calculated by measuring the relative spin populations after rf sweeps inducing an adiabatic rapid passage (ARP), as a function of rf power. By measuring the transferred fraction, we can then deduce Ω [77]. The error bars are underestimates of the uncertainty, reflecting the error in the fit to B.

We image the final state atoms by performing a ARP with $> 95\%$ efficiency into the $|3, 0\rangle$ state. Atoms are imaged with σ^- light, which also optically pumps them to the $|3, -3\rangle$ state where the imaging light is now resonant with the $|3, -3\rangle$ to $|4', -4'\rangle$ cycling transition. Because the imaging light is off resonant with the initial optical-pumping transitions, and these transitions have smaller Clebsch-Gordan factors relative to the cycling transition, the number we measure in the absorption images of this state is systematically low. We describe this systematic with an imaging

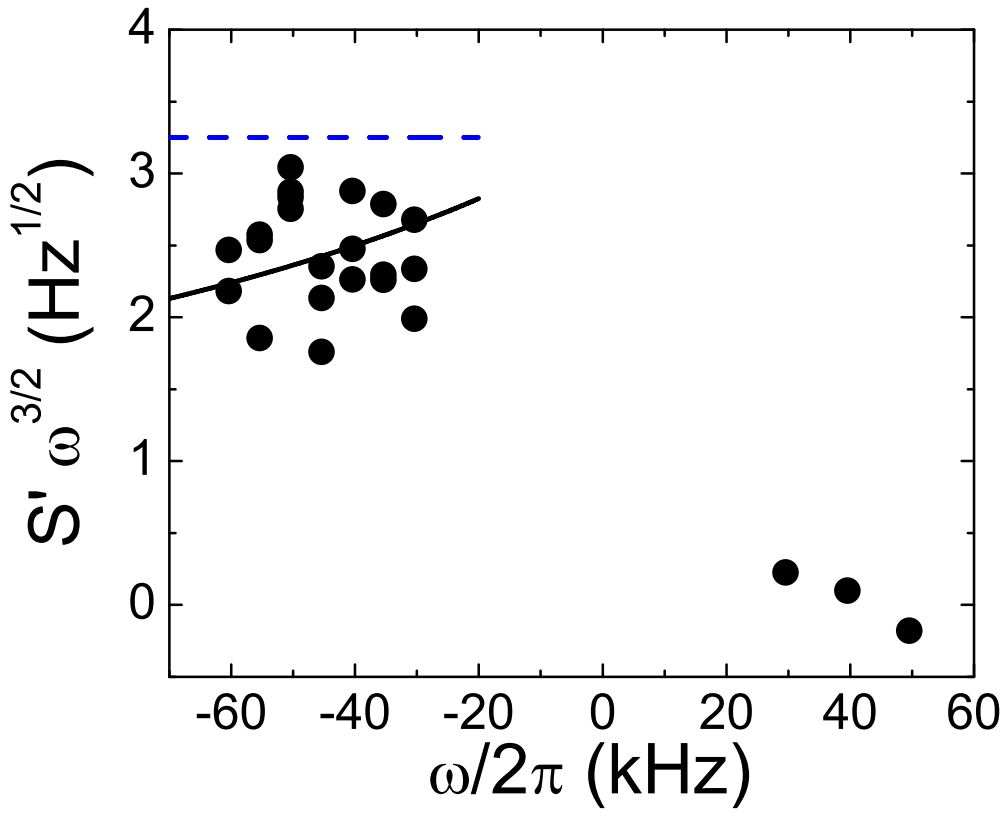

Figure 5.3: Extracting the contact at $a = 500\ a_0$, $n_{\text{avg}} = 4.9\times10^{12}\ \text{cm}^{-3}$, where n_{avg} is the density-weighted-density of the BEC. The condensate fraction for this data was 73%. The signal has again been normalized so that $S'(\omega) = S(\omega)/\int_{-\infty}^{\infty} S(\omega)d\omega$, as well as multiplied by the $\omega^{3/2}$ dependence. We fit this (black line) to $B/\beta(\omega) = S'(\omega)\omega^{3/2} = \frac{1}{4\pi^2}\alpha\sqrt{\frac{\hbar}{m}}\frac{C}{N}$, where $C = 8\pi\sqrt{\frac{m}{\hbar}}\frac{B}{\tau\Omega^2\alpha(a)}$. Thus $\frac{C}{N} = B\frac{4\pi^2}{\alpha}\sqrt{\frac{m}{\hbar}}$, and we are able to extract the contact. We also plot the fitted value of B (dashed blue line), which is what the signal would have been had $\beta(\omega) = 1$, illustrating this final-state effect.

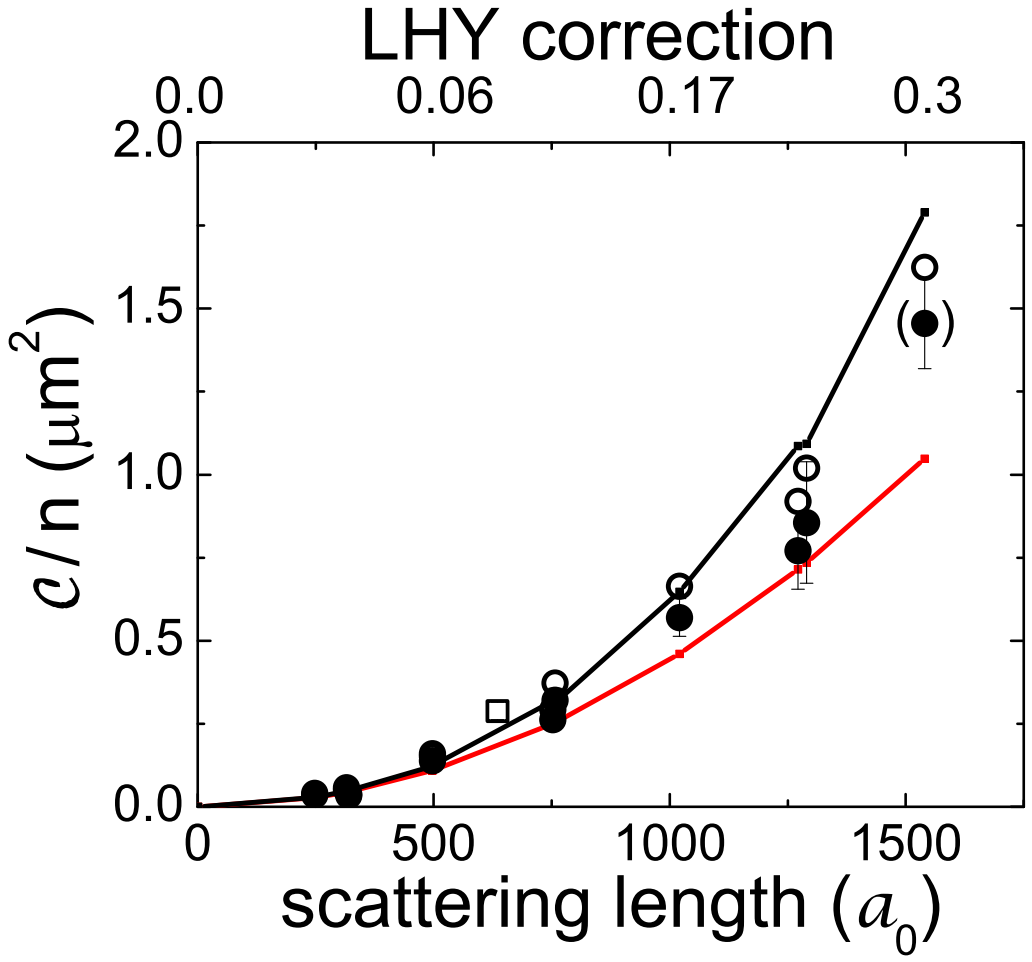

Figure 5.4: *Preliminary* BEC contact data as a function of interaction strength. Measured contact per particle (open circles) divided by n for different interaction strengths. The black circles show the data after making a correction for finite temperature as described in the text. The s-wave scattering length is given in units of a_0 on the lower scale and the fractional LHY correction is shown on the upper scale. The red line shows the mean-field prediction, using a local density approximation, while the black line is calculated like the red, but includes the LHY correction to the energy as well. It should be noted that it is quite possible that the apparent agreement between the data and the theory is fortuitous, and the error bars are not indicative of the other systematics inherent in these measurements.

efficiency η. The imaging efficiency is measured by comparing the number of atoms measured in the $|3,0\rangle$ versus the $|3,-3\rangle$ state in subsequent absorption images of thermal clouds of atoms. The states are prepared by using rf pulses and ARPs and we can check them by verifying that the measured atoms remaining in the $|2,-2\rangle$ or $|2,-1\rangle$ state is negligible. We later found out that this measured efficiency was highly sensitive to probe detuning, which was not constant throughout the data presented in Fig. 5.4. As a consequence the error bars shown in Fig. 5.4 are at best a lower limit to the actual uncertainty in the data, and we cannot accurately make an LHY measurement from these results.

The breathing-mode excitations discussed in Ch. 2 are modeled [56] and we find that at the time of the rf pulse the density has changed by less than 10%. In Fig. 3, this calculated density decrease has been included in the results. We also consider the effects of finite temperature in the contact measurement. At $a = 750\ a_0$, we have measured the dependence of C on the condensate fraction, and we use this to empirically extrapolate our data (white circles) to zero temperature (black circles).

It should be noted that for the contact the next order correction is expected to be as large as the LHY correction itself at 1200 a_0 for our densities [34, 35, 36].

5.3.1 Advantages

Contact spectroscopy, offers advantages compared to a direct probe of the energy of the gas. As mentioned earlier, three-body loss limits the time available for probing a BEC with large a, and this, in turn, can limit the resolution of energy measurements. However, in measuring the contact, the pertinent data is the amplitude of the signal far-detuned from resonance and noise on the central resonance of the lineshape is much less of a concern. This also allows us to use a short rf pulse if needed, since Fourier broadening of our pulse is tolerable. Finally, in Fig. 5.5, we show that final-state effects in the case of ^{85}Rb serve to enhance the signal, particularly at smaller values of na^3. Notice how the signal goes as $(a - a')^2$, whereas the contact itself (Eq. 5.3) goes as a^2. This will help facilitate a future measure of the LHY term, by giving an opportunity to validate

measurements at interaction strengths for which the LHY correction is negligible, and the physics is well understood.

5.3.2 Challenges

Contact spectroscopy is not without challenges. The biggest challenge we have found is in obtaining accurate measures of the BEC number. This is crucial for any contact measurement as the contact is an extensive quantity. We had previously tried to avoid such issues by normalizing our measurements to the total lineshape (i.e. determining $\tau\Omega^2 N$) , as given by Eq. 5.5. It turns out there is some difficulty with this approach, as seen in Fig. 5.6(b), where the Rabi frequency as measured with an ARP is compared with a Rabi frequency measured by integrating the lineshape. The suspected mechanism for suppressing the number of atoms outcoupled to the final state (which is directly proportional to $\tau\Omega^2 N$) is collapse induced by the large, negative background scattering length of -565 a_0. This collapse would lead to large three-body loss rates, and atoms that would never be imaged [66].

This effect should only occur for measurements on resonance, and not for data at large rf detuning. This is because the atoms outcoupled in the $1/\omega^{3/2}$ tail at large detuning have kinetic energies (see Fig. 5.2) much larger than the attractive energy provided by $a' = -565\ a_0$ (~ 300 Hz).

5.4 Conclusion

In conclusion, we have presented the first measurements of the contact in a BEC. Our result show the correct scaling with a, and the outcoupled atoms also reflect the high-k tail that we would expect in a contact measurement. We hope this measurement technique, contact spectroscopy, will allow for future investigation of dynamics following a fast change in the interaction strength. It will also be interesting to push these measurements into regimes where the interaction can no longer be considered perturbative.

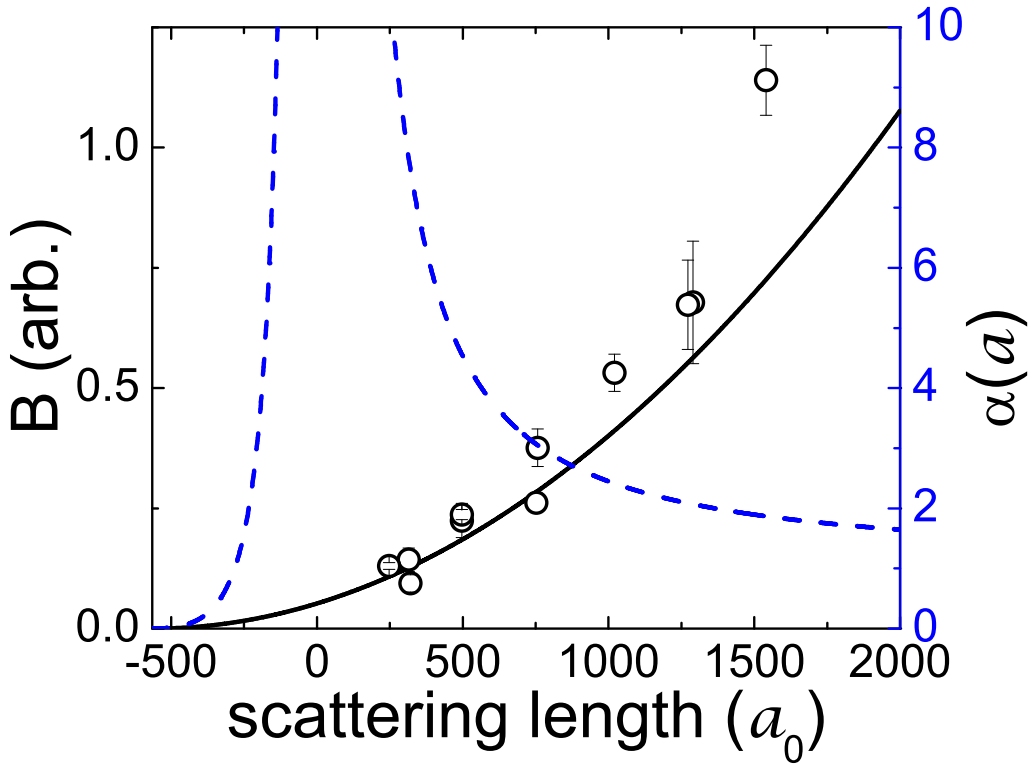

Figure 5.5: Strength of signal at different a, divided by the average density, n. The data has again been normalized to $\int_{-\infty}^{\infty} S(\omega)d\omega$. The solid line is the prediction for mean-field theory. The effect of the $\alpha(a) = (a'/a - 1)^2$ final state correction is shown in the blue dashed line, and its effect on the data is clearly seen here, shifting what would be a parabola centered about 0 to one centered about $a' = -565a_0$. This effect greatly enhances our signal at small a, making future calibrations of contact measurements at low na^3 possible. This will be important for eventual measurements of the LHY correction at high na^3.

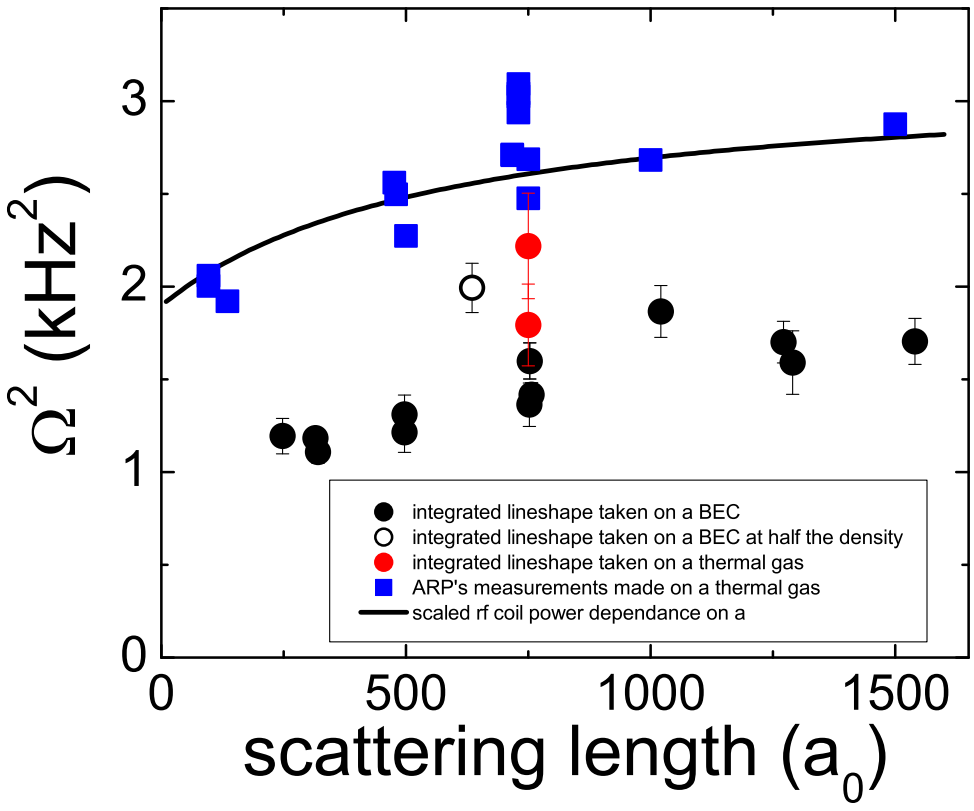

Figure 5.6: Pitfalls of using $\int S(\omega)d\omega$ to calculate $\tau\Omega^2 N$. Blue squares correspond to ARP measurements used to determine Ω^2. For the black circles, the Rabi frequency is determined by integrating a lineshape like that shown in Fig. 5.2(a). The rf power, and therefore the Rabi frequency, is dependant on the frequency of the rf, which in turn depends on the B-field. On the x-axis, we show the scattering length, which is tuned by varying the B-field. The fact that the black circles are systematically low supports the argument that the $|3,0\rangle$ atoms suffer loss and are not fully counted. Data taken in a similar fashion using a low density thermal gas (red circles), or BECs at half the density (open circle) further support this argument. The black line is arbitrarily scaled and reflects the response of the rf antenna as a function of B-field.

Chapter 6

Conclusion

We began this thesis with an allegorical story of a horse chasing some mythical carrot, so it only feels right to end it in the same way. While some of the smaller questions about the story might have been solved by the reader (in particular, the identities of the farmers holding the stick) there exist more fundamental questions: Have we tasted the carrot? How much farther is the carrot patch?

6.1 A small bite

While we have not been able to make a quantitative measure of the LHY correction in a BEC, I believe we are on the doorstep, staring down upon this carrot patch. The advantages provided by the 10 Hz spherical trap are being harnessed every day in lab, as 1 ms probes at large na^3 are now the norm, whereas before they were only a dream. Bragg spectroscopy provided our first taste of the carrot in the 2008 experiments we performed at large na^3. Fully motivated from the nibble, we have been able to carve out two distinct roads for approaching our many-body physics destination.

The first is the experimentally realized photon counting technique for Bragg spectroscopy. This path can be a little hilly, as we always measure a net response that complicates Bragg at small k, but steers clear entirely the problems incurred with large interactions that complicate a Bragg signal. In addition, it offers a number of tangential opportunities for the study of BEC physics. While these might not fall in line with our strictly carrotarian diet, they might provide a satisfying meal in their own right.

The second is contact spectroscopy, a new stretch of road that perhaps offers the straightest path towards an LHY measurement and our carrot patch. We have shown preliminary data verifying that contact measurements are feasible in our system, and look ideally suited to measure the LHY correction. As with any new road, however, there are a spots that need to be ironed out. Primary among them is an accurate way to measure the number in a strongly interacting BEC, or, better yet, a way to normalize the measurements of the rf tail. With the promise this has to offer, though, it will not be long before this becomes a major highway on the way to BEC enlightenment.

6.2 Staring down on the carrot patch

I believe the future looks bright for the strongly interacting BEC machine. With the preliminary results contact spectroscopy has brought in, an LHY measurement looks like it might be "one week away". My brothers-in-lab have already implemented high-field imaging, and a host of other technical improvements mere moments after I set foot out the door. With a few more systematics nailed down, they should be publishing some highly sought after results in the near future. With contact spectroscopy, there is a hope that we could also test the rates of our sweeps of a to determine the proper criteria for adiabaticity with respect to local many-body equilibrium. This is a current debate amongst ourselves and if we could shed light on this subject BEC dynamics could be experimental desserts.

The photon-counting that we worked so hard for ultimately took a back seat to the contact spectroscopy measurements that are still underway. This probe still has much to offer in terms of BEC physics, however, as there is an entire jungle of experimental phase-space still left to be explored in the many-body map (see Fig. 3.3). A few weeks before making the leap to contact spectroscopy, we discovered that we had been using a much smaller beam waist than we had planned for. It would have been interesting to see what results could have come from a redesigned weak beam at 15 μm. The ideas being tossed around at the time were of blue-detuned trap beams to damp out slosh, moving to a higher k so that the lineshapes were cleanly separated, or probing at $\theta = 90^\circ$ and $\theta = 180^\circ$, as our redesigned trap offered new areas to map out the dispersion of

strongly interacting BEC.

Other outstanding questions could be directly answered with our photon counting technique by using the larger ^{87}Rb clouds afforded in our experiment. It is predicted that the temperature dependence of $S(k)$ could be observed by measuring the Bragg response with a photon-counting technique [70]. In addition, with a system capable of studying the dynamics of a Bragg excitation, fundamental questions of the coherence of these momentum excitations can be addressed, which would have clear value to the atom-optics community. There are plenty of carrots to be had with the ^{85}Rb machine, and I believe through our work, the stick holding them from our nose is that much shorter.

Bibliography

[1] J. Wilks, *The properties of liquid and solid helium* (Clarendon P., Oxford, 1967).

[2] W. H. Keesom and M. Wolfke, *Proc. R. Acad. Amst.* **31**, 90 (1928).

[3] W. H. Keesom, *Helium* (Elsevier, Amsterdam, New York, 1942).

[4] W. H. Keesom and K. Clusius, *Proc. R. Acad. Amst.* **35**, 307 (1932).

[5] P. Kapitza, Viscosity of Liquid Helium below the λ-Point, *Nature* **141**, 74 (1938).

[6] J. F. Allen and A. D. Misener, Flow of Liquid Helium II, *Nature* **141**, 75 (1938).

[7] A. Griffin, New light on the intriguing history of superfluidity in liquid ^{4}He, *J. Phy.: Condens. Matter* **21**, 164220 (2009).

[8] V. P. Peshkov, *J. Phys. USSR* **8**, 131 (1944).

[9] V. P. Peshkov, *J. Phys. USSR* **10**, 389 (1946).

[10] H. E. Hall and W. F. Vinen, The rotation of liquid helium II. I. Experiments on the propagation of second sound in uniformly rotating helium II, *Proc. Roy. Soc. A* **238**, 204,215 (1956).

[11] L. Onsager, Statistical Hydrodynamics, *Nuovo Cimento* **6,** Suppl. 2, 249 (1949).

[12] H. Palevsky, K. Otnes, and K. E. Larsson, Excitation of Rotons in Helium II by Cold Neutrons, *Phys. Rev.* **112**, 11 (1958).

[13] D. G. Henshaw and A. D. B. Woods, Modes of Atomic Motions in Liquid Helium by Inelastic Scattering of Neutrons, *Phys. Rev.* **121**, 1266 (1961).

[14] L. Landau, *J. Phys. USSR* **5**, 71 (1941).

[15] R. P. Feynman and M. Cohen, Energy Spectrum of the Excitations in Liquid Helium, *Phys. Rev.* **102**, 1189 (1956).

[16] L. L. P. Pitaevskii, *Sov. Phys. JETP* **9**, 830 (1959).

[17] W. L. McMillan, Ground State of Liquid He^4, *Phys. Rev.* **138**, A442 (1965).

[18] D. Schiff and L. Verlet, Ground State of Liquid Helium-4 and Helium-3, *Phys. Rev.* **160**, 208 (1967).

[19] J. Boronat and J. Casulleras, Microscopic calculation of the phonon-roton branch in superfluid 4 He, *EPL (Europhysics Letters)* **38**, 291 (1997).

[20] L. Tisza, Transport Phenomena in Helium II, *Nature* **141**, 913 (1938).

[21] L. Tisza, Sur la théorie des liquides quantiques. Application a l'hélium liquide, *J. Phys. Radium* **1**, 164 (1940).

[22] L. Tisza, The Theory of Liquid Helium, *Phys. Rev.* **72**, 838 (1947).

[23] F. London, The λ-Phenomenon of Liquid Helium and the Bose-Einstein Degeneracy, *Nature* **141**, 643 (1938).

[24] N. Bogoliubov, On the theory of superfluidity, *J. Phys. USSR* **11**, 23 (1947).

[25] R. A. Cowley and A. D. B. Woods, Neutron Scattering from Liquid Helium at High Energies, *Phys. Rev. Lett.* **21**, 787 (1968).

[26] O. K. Harling, High-Energy Neutron Scattering Measurements on Liquid Helium and Bose Condensation in He II, *Phys. Rev. A* **3**, 1073 (1971).

[27] J. Steinhauer, R. Ozeri, N. Katz, and N. Davidson, Excitation Spectrum of a Bose-Einstein Condensate, *Phys. Rev. Lett.* **88**, 120407 (2002).

[28] M. J. Jamieson, Adiabatically corrected scattering lengths and effective ranges for collisions of helium atoms, *Chemical Physics Letters* **310**, 222 (1999).

[29] T. D. Lee and C. N. Yang, Many-Body Problem in Quantum Mechanics and Quantum Statistical Mechanics, *Phys. Rev.* **105**, 1119 (1957).

[30] T. D. Lee, K. Huang, and C. N. Yang, Eigenvalues and Eigenfunctions of a Bose System of Hard Spheres and Its Low-Temperature Properties, *Phys. Rev.* **106**, 1135 (1957).

[31] P. Noziéres and D. Pines, *The Theory of Quantum Liquids, Vol. II Superfluid Bose Liquids* (Addison-Wesley, Boulder, CO, 1990).

[32] A. L. Fetter and J. D. Walecka, *Quantum Theory of Many-Particle Systems* (Dover Publications, Mineola, New York, 2003).

[33] L. Pitaevskii and S. Stringari, *Bose-Einstein Condensation* (Clarendon Press, Oxford, 2003).

[34] T. T. Wu, Ground State of a Bose System of Hard Spheres, *Phys. Rev.* **115**, 1390 (1959).

[35] E. Braaten, H.-W. Hammer, and T. Mehen, Dilute Bose-Einstein Condensate with Large Scattering Length, *Phys. Rev. Lett.* **88**, 040401 (2002).

[36] S. Tan, Three-boson problem at low energy and implications for dilute Bose-Einstein condensates, *Phys. Rev. A* **78**, 013636 (2008).

[37] L. Sanchez-Palencia, D. Clément, P. Lugan, P. Bouyer, G. V. Shlyapnikov, and A. Aspect, Anderson Localization of Expanding Bose-Einstein Condensates in Random Potentials, *Phys. Rev. Lett.* **98**, 210401 (2007).

[38] F. S. Cataliotti, S. Burger, C. Fort, P. Maddaloni, F. Minardi, A. Trombettoni, A. Smerzi, and M. Inguscio, Josephson Junction Arrays with Bose-Einstein Condensates, *Science* **293**, 843 (2001).

[39] M. Greiner, O. Mandel, T. Esslinger, T. W. Hänsch, and I. Bloch, Quantum phase transition from a superfluid to a Mott insulator in a gas of ultracold atoms, *Nature* **415**, 39 (2002).

[40] C. A. Regal, M. Greiner, and D. S. Jin, Observation of Resonance Condensation of Fermionic Atom Pairs, *Phys. Rev. Lett.* **92**, 040403 (2004).

[41] J. E. Thomas, J. Kinast, and A. Turlapov, Virial Theorem and Universality in a Unitary Fermi Gas, *Phys. Rev. Lett.* **95**, 120402 (2005).

[42] W. Ketterle and M. W. Zwierlein, in *Proceedings of the International School of Physics "Enrico Fermi", Course CLXIV*, edited by M. Inguscio, W. Ketterle, and C. Salomon (IOS Press, Amsterdam, 2008).

[43] J. T. Stewart, J. P. Gaebler, and D. S. Jin, Using photoemission spectroscopy to probe a strongly interacting Fermi gas, *Nature* **454**, 744 (2008).

[44] G. Roati, C. D'Errico, L. Fallani, M. Fattori, C. Fort, M. Zaccanti, G. Modugno, M. Modugno, and M. Inguscio, Anderson localization of a non-interacting BoseEinstein condensate, *Nature* **453**, 895 (2008).

[45] M. Fattori *et al.*, in *Proceedings of the International Conference on Atomic Physics* (World Scientific, Singapore, 2008).

[46] N. R. Claussen, S. J. J. M. F. Kokkelmans, S. T. Thompson, E. A. Donley, E. Hodby, and C. E. Wieman, Very-high-precision bound-state spectroscopy near a ^{85}Rb Feshbach resonance, *Phys. Rev. A* **67**, 060701 (2003).

[47] C. Chin, R. Grimm, P. Julienne, and E. Tiesinga, Feshbach resonances in ultracold gases, *Rev. Mod. Phys.* **82**, 1225 (2010).

[48] S. L. Cornish, N. R. Claussen, J. L. Roberts, and E. A. C. andC. E. Wieman, Stable ^{85}Rb Bose-Einstein Condensates with Widely Tunable Interactions, *Phys. Rev. Lett.* **85**, 1795 (2000).

[49] S. B. Papp, Experiments with a two-species Bose-Einstein condensate utilizing widely tunable interparticle interactions, Ph.D. thesis, University of Colorado, 2007.

[50] P. A. Altin, N. P. Robins, D. Doring, J. E. Debs, R. Poldy, C. Figl, and J. D. Close, ^{85}Rb tunable-interaction Bose–Einstein condensate machine, *Review of Scientific Instruments* **81**, 063103 (2010).

[51] P. O. Fedichev, M. W. Reynolds, and G. V. Shlyapnikov, Three-Body Recombination of Ultracold Atoms to a Weakly Bound s Level, *Phys. Rev. Lett.* **77**, 2921 (1996).

[52] J. L. Roberts, Bose-Einstein Condensates with Tunable Atom-atom Interactions: The First Experiments with ^{85}Rb BECs, Ph.D. thesis, University of Colorado, 2001.

[53] D. S. Jin, J. R. Ensher, M. R. Matthews, C. E. Wieman, and E. A.Cornell, Collective Excitations of a Bose-Einstein Condensate in a Dilute Gas, *Phys. Rev. Lett.* **77**, 420 (1996).

[54] S. B. Papp, J. M. Pino, R. J. Wild, S. Ronen, C. E. Wieman, D. S. Jin, and E. A. Cornell, Bragg Spectroscopy of a Strongly Interacting ^{85}Rb Bose-Einstein Condensate, *Phys. Rev. Lett.* **101**, 135301 (2008).

[55] F. Dalfovo, S. Giorgini, L. P. Pitaevskii, and S. Stringari, Theory of Bose-Einstein condensation in trapped gases, *Rev. Mod. Phys.* **71**, 463 (1999).

[56] V. M. Pérez-García, H. Michinel, J. I. Cirac, M. Lewenstein, and P. Zoller, Dynamics of Bose-Einstein condensates: Variational solutions of the Gross-Pitaevskii equations, *Phys. Rev. A* **56**, 1424 (1997).

[57] J. Goldwin, Quantum Degeneracy and Interactions in the ^{87}Rb -^{40}K Bose-Fermi Mixture, Ph.D. thesis, University of Colorado, 2005.

[58] J. P. Burke, Jr., J. L. Bohn, B. D. Esry, and C. H. Greene, Prospects for Mixed-Isotope Bose-Einstein Condensates in Rubidium, *Phys. Rev. Lett.* **80**, 2097 (1998).

[59] J. L. Roberts, N. R. Claussen, S. L. Cornish, and C. E. Wieman, Magnetic Field Dependence of Ultracold Inelastic Collisions near a FeshbachResonance, *Phys. Rev. Lett.* **85**, 728 (2000).

[60] W. Petrich, M. H. Anderson, J. R. Ensher, and E. A.Cornell, Stable, Tightly Confining Magnetic Trap for Evaporative Cooling of NeutralAtoms, *Phys. Rev. Lett.* **74**, 3352 (1995).

[61] M. D. Barrett, J. A. Sauer, and M. S. Chapman, All-Optical Formation of an Atomic Bose-Einstein Condensate, *Phys. Rev. Lett.* **87**, 010404 (2001).

[62] S. R. Granade, M. E. Gehm, K. M. O'Hara, and J. E. Thomas, All-Optical Production of a Degenerate Fermi Gas, *Phys. Rev. Lett.* **88**, 120405 (2002).

[63] D. M. Stamper-Kurn, H.-J. Miesner, A. P. Chikkatur, S. Inouye, J. Stenger, and W. Ketterle, Reversible Formation of a Bose-Einstein Condensate, *Phys. Rev. Lett.* **81**, 2194 (1998).

[64] P. W. H. Pinkse, A. Mosk, M. Weidemüller, M. W. Reynolds, T. Hijmans, and J. T. M. Walraven, Adiabatically Changing the Phase-Space Density of a Trapped Bose Gas, *Phys. Rev. Lett.* **78**, 990 (1997).

[65] H. J. Lewandowski, Coherences and correlations in an ultracold Bose gas, Ph.D. thesis, University of Colorado, 2002.

[66] E. A. Donley, N. R. Claussen, S. L. Cornish, Roberts, J. L., E. A. Cornell, and C. E. Wieman, Dynamics of collapsing and exploding BoseEinstein condensates, *Nature* **412**, 295 (2001).

[67] S. K. Tung, Probing an interacting Bose gas in a quasi-two-dimensional trap, Ph.D. thesis, University of Colorado, 2010.

[68] J. M. Vogels, K. Xu, C. Raman, J. R. Abo-Shaeer, and W. Ketterle, Experimental Observation of the Bogoliubov Transformation for a Bose-Einstein Condensed Gas, *Phys. Rev. Lett.* **88**, 060402 (2002).

[69] A. Brunello, F. Dalfovo, L. Pitaevskii, and S. Stringari, How to Measure the Bogoliubov Quasiparticle Amplitudes in a Trapped Condensate, *Phys. Rev. Lett.* **85**, 4422 (2000).

[70] D. M. Stamper-Kurn, A. P. Chikkatur, A. Görlitz, S. Inouye, S. Gupta, D. E. Pritchard, and W. Ketterle, Excitation of Phonons in a Bose-Einstein Condensate by Light Scattering, *Phys. Rev. Lett.* **83**, 2876 (1999).

[71] S. T. Beliaev, Energy-spectrum of a non-ideal Bose gas, *Sov. Phys. JETP* **34**, 299 (1958).

[72] R. P. Feynman, Atomic Theory of the Two-Fluid Model of Liquid Helium, *Phys. Rev.* **94**, 262 (1954).

[73] R. P. Feynman, in *Progress in Low Temperature Physics*, edited by C. J. Gorter (Interscience, New York, 1955), Vol. 1, Chap. II, pp. 17–53.

[74] Y.-J. Wang, D. Z. Anderson, V. M. Bright, E. A. Cornell, Q. Diot, T. Kishimoto, M. Prentiss, R. A. Saravanan, S. R. Segal, and S. Wu, Atom Michelson Interferometer on a Chip Using a Bose-Einstein Condensate, *Phys. Rev. Lett.* **94**, 090405 (2005).

[75] W. Ketterle and S. Inouye, Collective enhancement and suppression in Bose-Einstein condensates, arXiv:cond-mat/0101424.

[76] A. Brunello, F. Dalfovo, L. Pitaevskii, S. Stringari, and F. Zambelli, Momentum transferred to a trapped Bose-Einstein condensate by stimulatedlight scattering, *Phys. Rev. A* **64**, 063614 (2001).

[77] H. Metcalf and P. van der Straten, *Laser Cooling and Trapping* (Springer, New York, 1999).

[78] D. Steck, Rubidium 85 D Line Data, http://steck.us/alkalidata/rubidium85numbers.pdf.

[79] D. Pines and P. Noziéres, *The Theory of Quantum Liquids, Vol. I Normal Fermi Liquids* (Westview Press, Boulder, CO, 1988).

[80] F. Zambelli, L. Pitaevskii, D. M. Stamper-Kurn, and S. Stringari, Dynamic structure factor and momentum distribution of a trapped Bose gas, *Phys. Rev. A* **61**, 063608 (2000).

[81] D. M. Ceperley, Path integrals in the theory of condensed helium, *Rev. Mod. Phys.* **67**, 279 (1995).

[82] J. Steinhauer, R. Ozeri, N. Katz, and N. Davidson, Peak in the static structure factor of a Bose-Einstein condensate, *Phys. Rev. A* **72**, 023608 (2005).

[83] J. Stenger, S. Inouye, A. P. Chikkatur, D. M. Stamper-Kurn, D. E. Pritchard, and W. Ketterle, Bragg Spectroscopy of a Bose-Einstein Condensate, *Phys. Rev. Lett.* **82**, 4569 (1999).

[84] J. Stenger, S. Inouye, A. P. Chikkatur, D. M. Stamper-Kurn, D. E. Pritchard, and W. Ketterle, Erratum: Bragg Spectroscopy of a Bose-Einstein Condensate [Phys. Rev. Lett. 82, 4569 (1999)], *Phys. Rev. Lett.* **84**, 2283 (2000).

[85] P. L. Gould, G. A. Ruff, and D. E. Pritchard, Diffraction of atoms by light: The near-resonant Kapitza-Dirac effect, *Phys. Rev. Lett.* **56**, 827 (1986).

[86] P. J. Martin, B. G. Oldaker, A. H. Miklich, and D. E. Pritchard, Bragg scattering of atoms from a standing light wave, *Phys. Rev. Lett.* **60**, 515 (1988).

[87] J. M. Pino, R. J. Wild, P. Makotyn, D. S. Jin, and E. A. Cornell, Photon counting for Bragg spectroscopy, *submitted to PRA* .

[88] B. E. A. Saleh and M. C. Teich, *Fundamentals of photonics* (Wiley, New York, 1991).

[89] A. Yariv, *Optical electronics in modern communications* (Oxford University Press, New York, 1997).

[90] I. Andonovic and D. Uttamchandani, *Principles of modern optical systems* (Artech House, Norwood, MA, 1989).

[91] M. A. de Araújo, R. Silva, E. de Lima, D. P. Pereira, and P. C. de Oliveira, Measurement of Gaussian laser beam radius using the knife-edge technique: improvement on data analysis, *Appl. Opt.* **48**, 393 (2009).

[92] R. Stutz, Towards Measuring the Electron Electric Dipole Moment Using Trapped Molecular Ions, Ph.D. thesis, University of Colorado, 2010.

[93] B. M. Peden, D. Meiser, M. L. Chiofalo, and M. J. Holland, Nondestructive cavity QED probe of Bloch oscillations in a gas of ultracold atoms, *Phys. Rev. A* **80**, 043803 (2009).

[94] N. Navon, S. Nascimbene, F. Chevy, and C. Salomon, The Equation of State of a Low-Temperature Fermi Gas with Tunable Interactions, *Science* **328**, 729 (2010).

[95] G. F. Gribakin and V. V. Flambaum, Calculation of the scattering length in atomic collisions using the semiclassical approximation, *Phys. Rev. A* **48**, 546 (1993).

[96] S. Tan, Energetics of a strongly correlated Fermi gas, *Ann. Phys.* **323**, 2952 (2008).

[97] S. Tan, Large momentum part of a strongly correlated Fermi gas, *Ann. Phys.* **323**, 2971 (2008).

[98] S. Tan, Generalized Virial Theorem and Pressure Relation for a strongly correlated Fermi gas, *Ann. Phys.* **323**, 2987 (2008).

[99] E. Braaten and L. Platter, Exact Relations for a Strongly-interacting Fermi Gas from the Operator Product Expansion, *Phys. Rev. Lett.* **100**, 205301 (2008).

[100] E. Braaten, D. Kang, and L. Platter, Universal relations for a strongly interacting Fermi gas near a Feshbach resonance, *Phys. Rev. A* **78**, 053606 (2008).

[101] R. Haussmann, M. Punk, and W. Zwerger, Spectral functions and rf response of ultracold fermionic atoms, *Phys. Rev. A* **80**, 063612 (2009).

[102] S. Zhang and A. J. Leggett, Universal properties of the ultracold Fermi gas, *Phys. Rev. A* **79**, 023601 (2009).

[103] F. Werner, L. Tarruel, and Y. Castin, Number of closed-channel molecules in the BEC-BCS crossover, *Eur. Phys. J. B* **68**, 401 (2009).

[104] E. D. Kuhnle, H. Hu, X.-J. Liu, P. Dyke, M. Mark, P. D. Drummond, P. Hannaford, and C. J. Vale, Universal Behavior of Pair Correlations in a Strongly Interacting Fermi Gas, *Phys. Rev. Lett.* **105**, 070402 (2010).

[105] J. T. Stewart, J. P. Gaebler, T. E. Drake, and D. S. Jin, Verification of Universal Relations in a Strongly Interacting Fermi Gas, *Phys. Rev. Lett.* **104**, 235301 (2010).

[106] R. Combescot, F. Alzetto, and X. Leyronas, Particle distribution tail and related energy formula, *Phys. Rev. A* **79**, 053640 (2009).

[107] A. M. J. Schakel, Tan Relations in Dilute Bose Gasses, arXiv:1007.3452.

[108] J. T. Stewart, Probing a strongly interacting Fermi gas, Ph.D. thesis, University of Colorado, 2009.

[109] W. Schneider, V. B. Shenoy, and M. Randeria, Theory of Radio Frequency Spectroscopy of Polarized Fermi Gases, arXiv:0903.3006.

[110] A. Perali, P. Pieri, and G. C. Strinati, Competition between final-state and pairing gap effects in the radio-frequency spectra of ultracold Fermi atoms, *Phys. Rev. Lett.* **100**, 010402 (2008).

[111] E. Braaten, D. Kang, and L. Platter, Short-Time Operator Product Expansion for rf Spectroscopy of a Strongly Interacting Fermi Gas, *Phys. Rev. Lett.* **104**, 223004 (2010).

[112] J. L. Bohn, (private communication).

Appendix A

Cart switch

To provide a uniform magnetic field in $\hat{y}$ (needed to shift the center of the magnetic potential of the 10 Hz spherical trap to compensate for sag and align to the optical trap) we modified the circuit driving a pair of coils that is mounted on our moving track [49]. The "cart coils" provide a magnetic quadrupole trap for the transfer of atoms from the MOT to the science cell, where the magnetic trap resides (see Ref. [49]). To go from the anti-Helmholtz configuration for the quadrupole trap potential to the Helmholtz configuration for a uniform field in $\hat{y}$ necessitates changing the direction of the current in one of the coils. While this might sound easy enough, these coils have significant inductances that we must fight against in order to keep things from...well, blowing up.

The switching scheme we use to flip the current in the top coil is referred to as the H-bridge, and is shown in Fig. A.1. To switch the direction of the current, we employ the same types of field-effect transistors (FETs) that are used for servoing the current in the cart coils.[1] Because the task of these FETs is only to switch the current direction, a mechanical relay would work fine for this application. However, for the large current ($\sim$250 A), we would need to string a number of solid state relays in parallel to make this work. The cost of these relays ($300/relay, with 8 relays needed) as well as our inexperience with them pushed us towards our trusted (and available) FETs. We opted to stay away from mechanical relays (read: expensive) to avoid changing the characteristic capacitance and impedance of the cart coils, and, more importantly, the dynamics of

[1] This is the APT10M07JVR FET that can be found in a number of the cold-atom groups here at JILA, and is the same one used in our magnetic trap servo.

the cart servo loop. We use three FETs in parallel, for each single FET shown in Fig. A.1, and we water-cool the FET bank in the typical way.

Complications to the switching scheme arise because of the inductance in the cart coils themselves. We calculate the self-inductance of each coil to be on the order of 70 μH. We also can directly measure $\frac{dI}{dt}$ using a Hall-probe current sensor after quickly turning off the current. Using $V = L\frac{dI}{dt}$ and the measured voltage when the current in the coils is turned off quickly gives us an inductance of 380 μH. This large discrepancy is most likely due to our neglecting of the resistance of the coils, which modifies the above voltage drop $V = L\frac{dI}{dt} + IR$. When installing the H-bridge configuration, we shut off the current running in series through the two coils and measured a 130 V spike (with respect to ground) at point (a) of the bottom coil (shown in Fig. A.1) and a 60 V spike (also with respect to ground) at point (b). These large spikes in voltage assured certain death for our switching FETs, as they are only rated to take at most a transient gate-source voltage of $\pm$40 V.

These transient voltages led us to make two modifications to the standard design. The first is the protection diodes seen in Fig. A.1. These diodes represent four 1N4004 diodes in parallel. The transient voltages, now given a shunt to the power supply voltage (which is typically 6 V), were reduced to 60 V at point (a) and 45 V at point (b).

While this helped with the problem of the FETs blowing up, our overall goal was a bit more ambitious than that. We still needed these FETs to stay on when asked! This was especially problematic, seeing as how the FETs respond to the aforementioned gate-source voltage, with our source voltage swinging up to as much as 60 V. Seeing as how the gate voltage was being referenced by our switching electronics, keeping the FET on (i.e. $V_{GS} > 3V$) was challenging. To that end, we devised a scheme that works equally well for high current switching as it does for household smoke alarms: the ever-popular 9V battery.

The batteries depicted in Fig. A.1 are of the 9V variety and function to maintain V_{GS} at 9 V by referencing the battery's anode to the FET's source. These FETs now function as switches in the "closed" position. To keep the other pair of FETs in their off state ("open" position) we

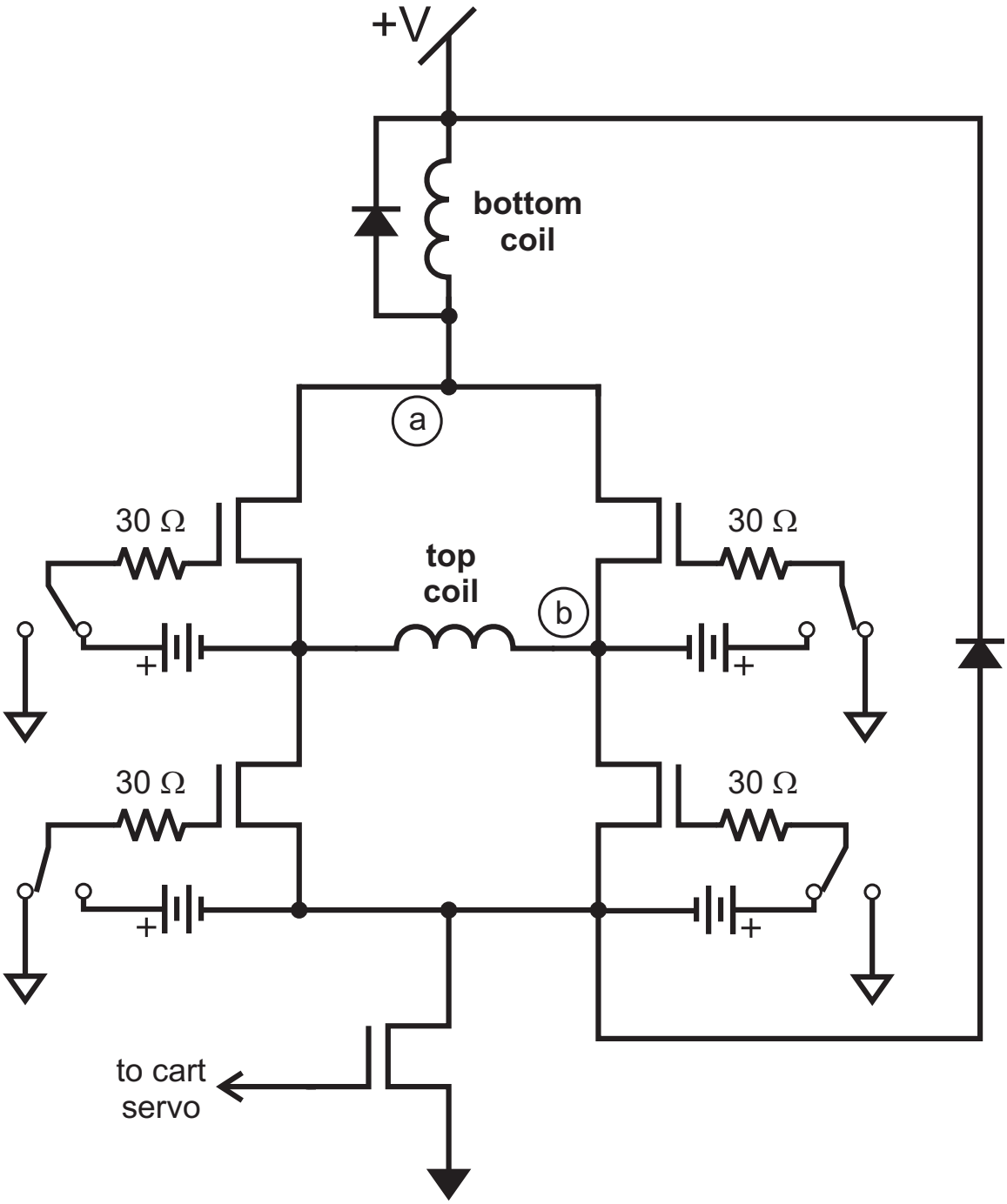

Figure A.1: Electrical schematic for H-bridge switching FETs. All of the switches shown here are tied together. As shown the current would flow through the top coil from left to right. Notice the separate grounds for the power supply and the switching electronics. Circled points are referred to in the text. The single FETs here represent three APT10M07JVR FETs in parallel. The switches shown are actually AZ831-2C-5DSE relays which are robust to high voltages.

reference the gate to the electronics ground, depicted by the hollow triangle. When we have the large voltage spikes induced by the quadrupole trap turn off these FETs stay in their "off" state, as V_{GS} becomes negative, in this case. We find that these batteries worked extremely well, despite the fact that the voltage spike is extremely fast, rising to its peak voltage in roughly 10 ms. We suspect that the battery is able to track the source voltage due to its negligible capacitance with the rest of the electronics.

Appendix B

Alternative approaches to BEC in a 10 Hz trap

B.1 The 2nd law of graduate student dynamics

There are a handful of "experimental axioms" tossed around in physics laboratories. Some of these are useful in diagnosing an elusive problem ("if you can't make things better, make things worse"). Some more useful in working with signals ("use lock-in detection, noise is always better at AC"). And some still for those interpreting data ("with enough fit parameters I can make the data agree too!"). Another axiom that is familiar with every graduate student in the lab is what I call the 2nd Law of Graduate Student Dynamics. Practically speaking, it means "If it ain't broke, don't fix it." This is learned through both experience ("...I touched this one knob that shouldn't do anything and now the experiment doesn't work...") and through instruction from the more senior students ("...don't ever, EVER touch any knob on here unless you absolutely have to..."). For better or worse this is a lab mantra, and, after doing a number of informal surveys (generally on the way to lunch) this is something ubiquitous to nearly every graduate student that has put in time on his or her respective machine. Much of this law borrows from the 2nd law of thermodynamics, which tells us that entropy and disorder will always go up in a system. In the laboratory this often means that each additional layer of control ("I made the experiment better!") comes at the cost of additional phase-space for things to spiral out of control ("...and now nothing works").

I mention this because in developing this spherical trap, we also had to develop a new evaporation scheme, throwing out a lot of what was working for us. And while our evaporation is defensible in light of its results, knowing the 2nd Law a different motivation is needed, at least

for the graduate students' sake. In this appendix, I outline a few other ideas and paths we chose to go down, with the goal of minimizing change, and why these other avenues ultimately did not succeed. What we found was that, for very different reasons, none of these strategies would work to our satisfaction. It was this realization that pushed us towards developing an entirely new way to think about evaporation and sympathetic cooling.

B.2 Crossed optical trap

Because simultaneous cooling of ^{85}Rb in the optical trap was successful, the simplest approach would be to add another laser beam for trapping in order to get the spherical geometry we desired. With this additional axial confinement, of course, comes larger mean trap frequencies, which are bad for both the physics we aim to study (see Fig. 2.3), as well as being major roadblock in the production of ^{85}Rb BEC [49].

In order to keep the mean trap frequency the same, we would need a reduced radial confinement, and hence more gravitational sag ($y_{sag} = g/\omega_y^2$). This is the eventual deal-breaker of optical trap geometries, because when the sag is on the order of the beam waist, the trap depth is compromised and strong anharmonic components are introduced in the potential. We predicted, however, that with substantial amounts of laser power ($\sim$ 1 W) at 1064 nm, and large enough beam waists (400 μm) a spherical trap would be possible with a potential created by two crossed beams. With this crossed beam design, the $\hat{y}$ direction would share the radial confinement between the two beams (i.e. both beams perpendicular to gravity).

In trying to implement this design, we found that with the needed laser intensities our optics severely distorted the imaging beam, as seen in Fig. B.1. We attributed this to heating of optical elements, causing a false signal in the OD images after the background image was taken 300 μs later and subtracted away. Shortly after this discovery we abandoned the crossed optical trap. Although heating of the optical elements could perhaps be avoided with less time between exposures, this type of trapping scheme would also require us to change out our original trap optics. Furthermore, this scheme would always be something of a compromise, having the spherical geometry, but still

with same relatively tight confinement as our previous optical trap.

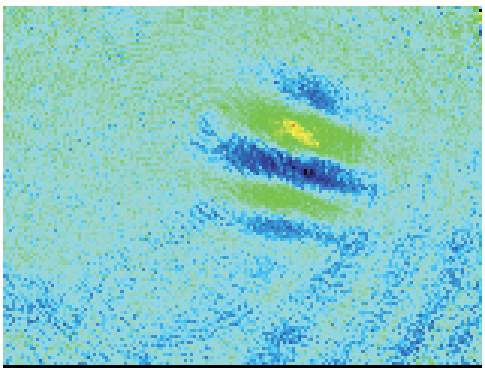

Figure B.1: Absorption image taken with no atoms present after $\sim$ 2 W of optical trap light for the crossed beam trap passed through optics shared with the imaging system. The contrast between the fringes seen here goes from an optical depth of -0.05 0.1. We speculate that these fringes are due to the heating and subsequent cooling of optical elements, distorts the beam profile. Changes in the spatial profile of the imaging beam between the shadow image and the reference image (without atoms), taken 300 ms later can cause the fringes.

B.3 BEC loading

The next approach, and perhaps the simplest one in terms of experimental changes, was to load atoms from the optical trap into the 10 Hz magnetic trap after we had created the BEC in our conventional way (simultaneous cooling of both ^{85}Rb and ^{87}Rb atoms in an optical dipole trap). This presented a few of its own difficulties, of course. First, as discussed previously, the equilibrium size of the BEC is very sensitive to the scattering length a. In order to keep the same scattering length throughout the loading process, we must ramp down the bias coil current in concert with ramping up of the magnetic trap currents. This would be necessary to avoid the breathing modes induced by a change in a, discussed previously.

The bigger issue, however, was in the gross mismatch of the shape and strength of the two traps. We would be loading from a $135 \times 135 \times 3$ Hz trap to one that was 10 Hz all around. Things like residual breathes and sloshes would be easily excited and eventually we would have to devise some way to damp these oscillations, which can be inherently difficult for a superfluid. These

mode-matching issues also showed up when the traps were slightly misaligned, as seen in Fig. B.2. Here, some of the BEC has spilled over a potential "bump" halfway through the load into the 10 Hz trap and the BEC then had a two-component shape. It was at this point that we abandoned this approach and realized that the only way a stable ^{85}Rb BEC was going to be happy in the 10 Hz trap was if it was born there.

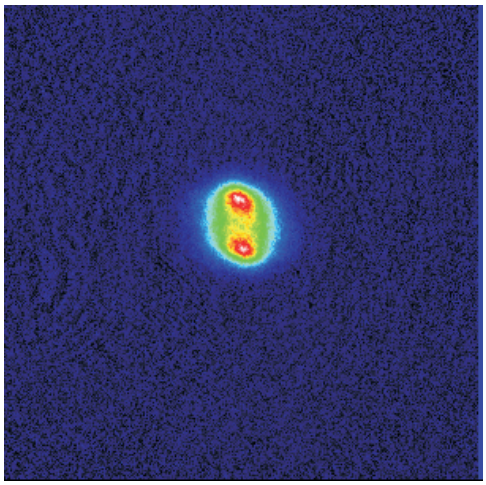

Figure B.2: Image of a ^{85}Rb BEC after ramp down from optical confinement to the weak, spherical trap. Images such as these, with two clearly distinguishable features, are a result of misalignment between the optical and weak magnetic traps.

B.4 Direct evaporation on ^{85}Rb

The last approach we tried before revamping the cooling scheme was to go back to the technique of the original ^{85}Rb experiments [48] and directly evaporate the ^{85}Rb gas, via forced rf evaporation, in the 10 Hz trap. Attempts at this were unsuccessful, however, and never proved very promising. We speculate that the extremely weak trap, with its sub-Hz collision rates, made evaporating on few minute duty cycles difficult. Considering that the original ^{85}Rb experiment was producing condensates of 10,000 atoms during its prime, we abandoned this approach without much regret, needing at least the 40,000 atoms we were getting in 2008 (and the signal-to-noise associated therein) for the experiments we proposed.